

# UC Santa Barbara

## UC Santa Barbara Electronic Theses and Dissertations

### Title

Investigating Electrokinetic and Electrochemical Phenomena in Confined Geometries through Multiphysical Modeling

### Permalink

<https://escholarship.org/uc/item/6xq8x1pb>

### Author

Eden, Alexander

### Publication Date

2019

Peer reviewed|Thesis/dissertation

UNIVERSITY OF CALIFORNIA

Santa Barbara

Investigating Electrokinetic and Electrochemical Phenomena in Confined Geometries through  
Multiphysical Modeling

A dissertation submitted in partial satisfaction of the  
requirements for the degree Doctor of Philosophy  
in Mechanical Engineering

by

Alexander Clinton Eden

Committee in charge:

Professor Carl Meinhart, Chair

Professor Sumita Pennathur

Professor Todd Squires

Professor Frederic Gibou

March 2019

The dissertation of Alexander Clinton Eden is approved.

---

Frederic Gibou

---

Todd Squires

---

Sumita Pennathur

---

Carl Meinhart, Committee Chair

January 2019

Investigating Electrokinetic and Electrochemical Phenomena in Confined Geometries through  
Multiphysical Modeling

Copyright © 2019

by

Alexander Clinton Eden

## ACKNOWLEDGEMENTS

I would like to acknowledge my advisors and doctoral committee for their assistance, thoughtful comments, and helpful critique throughout my graduate career. I would also like to acknowledge the co-authors from my publications for their knowledge and input in improving the quality of my research communication. Finally, I would like to acknowledge my family for their patience and support throughout my time at the University of California, Santa Barbara.

# VITA OF ALEXANDER CLINTON EDEN

January 2019

## EDUCATION

Bachelor of Science in Mechanical Engineering, University of California, Santa Barbara, June 2015 (Summa cum Laude)

Master of Science in Mechanical Engineering, University of California, Santa Barbara, June 2016

Doctor of Philosophy in Mechanical Engineering, University of California, Santa Barbara, January 2019 (expected)

## PROFESSIONAL EMPLOYMENT

2015-2019: Teaching Assistant/Graduate Student Researcher

## JOURNAL PUBLICATIONS

Eden *et al.*, "A hybrid experimental-numerical technique for determining 3D velocity fields from planar 2D PIV data," *Meas. Sci. Tech.*, 27 (2016), 094010.

Eden *et al.*, "Analyte preconcentration in nanofluidic channels with nonuniform zeta potential," *Phys. Rev. Fluids*, 2 (2017), 124203.

Eden *et al.*, "Modeling Faradaic reactions and electrokinetic phenomena at a nanochannel-confined bipolar electrode," *J. Phys. Chem. C*, (in press).

Scida *et al.*, "Discovery of transient electrochemical and electrokinetic effects at nanoconfined bipolar electrodes," (co-author) (under review).

## CONFERENCE PRESENTATIONS

11<sup>th</sup> International Symposium on Particle Image Velocimetry, Santa Barbara, CA, 2015

COMSOL Boston 2015, Boston, MA, 2015

3<sup>rd</sup> Annual Southern California Micro & Nanofluidics Symposium, Irvine, CA, 2016

COMSOL Boston 2016, Boston, MA, 2016

69<sup>th</sup> Annual Meeting of the APS Division of Fluid Dynamics, Portland, OR, 2016

COMSOL Boston 2017, Boston, MA, 2017

5<sup>th</sup> Annual Southern California Micro & Nanofluidics Symposium, Los Angeles, CA, 2018

COMSOL Boston 2018, Boston, MA, 2018

## AWARDS

Best Poster Award, COMSOL Conference Boston 2018

UCSB University Highest Honors at Graduation – Summa cum Laude

UCSB Dean's Honor List – 11 total quarters

## FIELDS OF STUDY

Major Emphases: 1) Micro and Nanotechnology, 2) Thermal and Fluid Sciences

Research with Meinhart Group: Particle image velocimetry experiments and numerical simulation of an AC electrothermal micromixer

Research with Pennathur Group: Simulation of field-effect controlled nanofluidics, bipolar electrochemistry, and electrokinetic micropumps

## ABSTRACT

### Investigating Electrokinetic and Electrochemical Phenomena in Confined Geometries through Multiphysical Modeling

by

Alexander Clinton Eden

In recent decades, microfluidics and nanofluidics have risen to the forefront of innovation and technological development for a plethora of analytical applications ranging from advanced point-of-care diagnostics and integrated drug delivery systems to multipurpose substance detection. These miniaturized platforms, made possible by emergent microfabrication technologies, often exploit unique features such as increased surface-liquid interactions and small sample volume requirements to efficiently carry out on-chip chemical and/or bioanalytical processes. Moreover, the inherent flexibility of these systems enables a number of processes such as mixing, focusing and separation, visualization and detection, and pumping to be integrated onto a single lab-on-chip platform. However, the physical phenomena that govern these processes tend to be complex and exhibit strong multiphysics coupling, particularly for nanoscale geometries in which finite electric double layers and associated charge-screening effects prevail. Here, numerical simulation offers an avenue for probing the highly coupled nature of electrokinetic and electrochemical effects in confinement, allowing us to elucidate the intricacies of such systems through modeling. By providing an improved fundamental understanding of relevant physical processes, these

numerical models enable researchers to optimize existing technologies and develop novel platforms for lab-on-chip applications.

In this work, we discuss the modeling of four separate microfluidic and nanofluidic systems suitable for a wide range of analytical processes. First, we discuss flow visualization in a micromixer device driven by electrothermal flow, with an emphasis on how particle image velocimetry measurements can be used to tune simulation results and better represent 3D flow structures in the physical system. Next, we present a nanofluidic analyte focusing and separation technique which leverages field-effect control via wall-embedded electrodes to locally modulate electric double layer properties and induce ion concentration polarization within the channel. Third, we discuss the dynamics of a nanochannel-confined bipolar electrode system and demonstrate how bipolar electrochemistry provides a flexible platform for mixing, preconcentration, and/or analyte detection. Finally, we introduce a variation of the bipolar electrode system which exploits the nonlinear hydrodynamics associated with induced-charge electroosmotic flow to electrokinetically actuate a peristaltic micropumping mechanism through fluid-structure interactions.

## TABLE OF CONTENTS

I. Electrothermal Micromixer: Theory, Measurement, and Modeling .....	1
A. Abstract.....	1
B. Introduction.....	1
C. Experimental Method .....	3
D. Numerical Model.....	6
E. Optimization.....	10
F. Results .....	12
G. Conclusion .....	20
H. Acknowledgement.....	20
References .....	22
II. Nanofluidics: The Electrical Double Layer and Field-Effect Control .....	25
A. Abstract.....	25
B. Introduction.....	26
C. Theoretical and Numerical Framework.....	29
1. Electrical Double Layers and Electroosmotic Flow .....	29
2. Nanofluidic Device .....	31
3. Governing Equations and 2D Numerical Model .....	32
4. Simplified 1D Area-Averaged Model.....	37
D. Results .....	41
1. Verification Simulations.....	41
2. Possible Enhancement Mechanisms.....	45
3. Analyte Focusing Using Nonuniform, Overlapped EDLs: 2D Simulation Results.....	50

4. Maximum Enhancement and Limiting Behavior .....	53
5. Simultaneous Focusing and Separation .....	55
4. Assumptions and Limitations .....	57
E. Conclusion.....	60
F. Additional Simulation Details .....	61
G. Acknowledgement.....	62
References .....	63
III. Bipolar Electrochemistry in Confined Geometries .....	68
A. Abstract.....	68
B. Introduction.....	69
C. Theory and Simulation.....	72
1. Numerical Model Overview .....	72
2. Theoretical Framework and Governing Equations.....	74
D. Experimental Methods.....	80
E. Results.....	81
1. BPE Charging Dynamics .....	81
2. Modeling Tracer Molecule Fluorescence.....	88
3. BPE-Induced Ion Concentration Polarization.....	90
4. BPE Discharging Dynamics .....	92
5. Effect of Oxide Growth on BPE .....	100
6. Deducing Information About Chemical Kinetics Through Simulation .....	104
F. Conclusion.....	107
G. Additional Simulation Details .....	108

H. Acknowledgement.....	114
References .....	115
III. Induced-Charge Electroosmotic Flow at Bipolar Electrodes: A Potential	
Mechanism for Mixing and Peristaltic Micropump Actuation .....	123
A. Abstract.....	123
B. Introduction.....	124
C. BPE Induced-Charge Electroosmotic Flow .....	125
D. BPE-Induced Peristaltic Pumping .....	127
E. Electrokinetic Mixing Using Bipolar Electrodes .....	133
F. Conclusion.....	135
G. Acknowledgement.....	135
References .....	136

# **I. Electrothermal Micromixer: Theory, Measurement, and Modeling**

## ***A. Abstract***

Knowledge of three-dimensional, three component velocity fields is central to the understanding and development of effective microfluidic devices for lab-on-chip mixing applications. In this chapter we present a hybrid experimental-numerical method for the generation of 3D flow information from 2D particle image velocimetry (PIV) experimental data and finite element simulations of an alternating current electrothermal (ACET) micromixer. A numerical least-squares optimization algorithm is applied to a theory-based 3D multiphysics simulation in conjunction with 2D PIV data to generate an improved estimation of the steady state velocity field. This 3D velocity field can be used to assess mixing phenomena more accurately than would be possible through simulation alone. Our technique can also be used to estimate uncertain quantities in experimental situations by fitting the gathered field data to a simulated physical model. The optimization algorithm reduced the root-mean-squared difference between the experimental and simulated velocity fields in the target region by more than a factor of 4, resulting in an average error less than 12% of the average velocity magnitude. This chapter was adapted from Eden *et al.*, *Meas. Sci. Tech.* 2016 (DOI: 10.1088/0957-0233/27/9/094010), and was reproduced with permission from the publisher. All rights reserved, © IOP Publishing.

## ***B. Introduction***

Electrokinetic flows produced by alternating current (AC) electric fields have been studied extensively and have proven to be an effective means of driving fluids and particles in applications such as mixing, stirring, focusing, and pumping.<sup>1-8</sup> These AC electrokinetic phenomena can be broadly classified into the following categories: electrothermal flow,

electroosmosis, and dielectrophoresis (DEP).<sup>2</sup> Fluid motion from electrothermal forces is due to the interaction of an electric field with thermally induced conductivity and permittivity gradients within the fluid. AC electroosmosis occurs when the tangential component of an electric field interacts with a field-induced electric double layer around a solid surface, resulting in a net body force on the fluid. Dielectrophoretic forces act on particles and result from differences in polarizability between a particle and fluid medium in the presence of a non-uniform electric field.<sup>6-8</sup> Here we study externally induced thermal gradients from Joule heating, resulting in fluid circulation due to electrothermal and buoyancy forces. Dielectrophoretic forces on tracer particles are also calculated and included to account for any DEP effects, which are most significant for particles near the electrodes. The frequencies on the order of 1 MHz in our experiments are much larger than typical electrode polarization frequencies. AC electroosmotic effects are thus negligible because there is insufficient time for charge accumulation in the diffuse double layer around the electrodes.<sup>9</sup> In our micromixer, configurable electrothermal fluid motion is generated by applying distinct AC signals to each of 5 different electrodes. These voltage patterns can include different signal phases and be periodically switched to induce chaotic mixing, but here we study the steady state case.<sup>4,8</sup>

Current methods for generating 3D velocity fields from PIV experiments require multiple-camera setups and custom processing software. These 3D PIV methods can be challenging to implement and can result in measurements with significantly lower out-of-plane accuracy than in-plane accuracy.<sup>10,11</sup> An alternate 3D POD PIV algorithm developed by Kauffman *et al.*<sup>12</sup> for generating out-of-plane velocity components from successive 2D measurements would require 16 interrogation regions to span the entire mixing chamber, each requiring measurements at 20 different height levels. Such large, data-intensive experiments can

introduce problems such as drift from various sources, as well as error from stitching the data together. Instead, we use numerical simulation and a curve-fitting optimization approach to extend the previous work of authors who have made use of the continuity equation to reconstruct out-of-plane velocity components from 2D measurements.<sup>12,13</sup>

Numerical simulation models of ACET flow provide a simpler way to estimate 3D flow fields and have been developed using various commercial finite element packages.<sup>14-17</sup> The works of Lee *et al* and Loire *et al* discuss efforts to simulate 2D electrothermal flows using *COMSOL Multiphysics*.<sup>16,17</sup> For our device, we use a combination of built-in *COMSOL Multiphysics* simulation modules and manually programmed partial differential equations to numerically represent the governing physical equations in 3D. This allows us to recreate the PIV experimental conditions through simulation, following Loire *et al*. However, these simulations can often have significant discrepancies with measurements for a variety of reasons, including inhomogeneous material properties, inexact experimental geometries, and assumptions made to simplify physical models. To refine this technique and develop a more accurate physical representation of the experimental conditions, we introduce an optimization algorithm that inputs a velocity field obtained through 2D PIV experiments and minimizes the velocity error between the experimental data and the 3D simulation results at the measurement plane. This method allows us to generate more accurate out-of-plane information in the simulation by scaling physical properties and measurement uncertainty parameters to fit experimental in-plane results.

### ***C. Experimental Method***

The ACET micromixer shown in Figures 1.1 and 1.2 is driven by 10  $\mu\text{m}$  thick electroless nickel immersion gold (ENIG) electrodes on an FR4 printed circuit board substrate. A 450

$\mu\text{m}$  deep x 3 mm x 3 mm PDMS well with a 1 mm thick glass cover defines the mixing chamber above the substrate. During experiments, the device was mounted on a 1 cm thick copper plate for thermal stasis. The PIV experiments were conducted with a solution of 0.1X phosphate-buffered saline (PBS) ( $\sigma_m = 1.9 \text{ mS/cm}$ ) seeded with 1  $\mu\text{m}$  diameter fluorescent latex beads used as tracer particles. A DC power supply and a function generator were used to supply a sinusoidal AC signal with an amplified peak-to-peak voltage of  $V_{pp} = 26 \text{ V}$  and a frequency of  $f = 1 \text{ MHz}$  to drive the flow. At this voltage and size scale of tracer particles, Brownian motion is considered negligible compared to motion from other forces involved.<sup>18</sup>

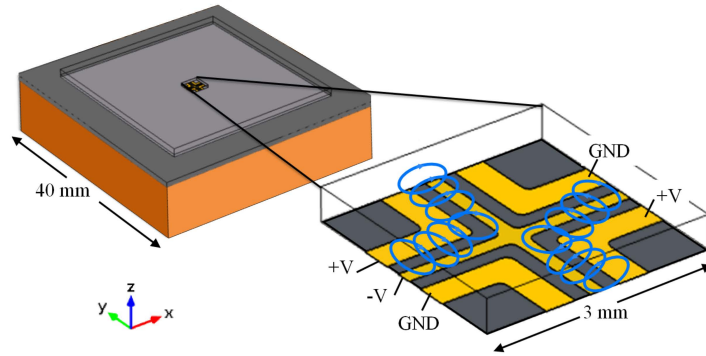


**Figure 1.1:** An overview of the ACET micromixer device, depicting the voltage pattern applied to the electrodes during experiments. The general flow pattern is indicated by vertical vortices between positive and negative electrodes.

The PIV measurements were made using the  $\mu\text{PIV}$  procedure pioneered by Meinhart, Wereley, and Santiago.<sup>19</sup> The flow field was imaged through an epi-fluorescent microscope (Nikon Eclipse FN1) with a 10X objective lens (Nikon Plan Fluor:  $\text{NA} = 0.30$ ). The focal plane was illuminated with frequency doubled Nd:YAG pulsed lasers (New Wave Research MiniLase II-30) controlled by a synchronizer (TSI LaserPulse Synchronizer). Measurements were made at heights of  $h_{zm} = 96 \mu\text{m}$  and  $148 \mu\text{m}$  above the chamber bottom, with an estimated measurement depth of  $\delta_{zm} = \pm 10.75 \mu\text{m}$  from the focal plane.<sup>20</sup> For each

experiment, 100 image pairs ( $\Delta t = 10$  ms) were recorded by a digital CCD camera (TSI PIVCAM 14-10 cross/auto correlation digital CCD Camera). The resulting images were of 1376 x 1024 pixel resolution with a square pixel size of 0.64  $\mu\text{m}/\text{pixel}$ . These images were processed using software with a custom PIV cross-correlation algorithm that ensemble averages the images and fits a 9-point Gaussian function to the data to determine the particle-image displacement peaks, yielding a 2-dimensional 33 x 24 velocity field for the images taken in each interrogation window.<sup>21</sup> Further data processing was performed on the velocity fields using proprietary vector cleanup software to remove erroneous measurement components. We estimate that approximately 3.5% of the raw data points consisted of spurious vectors that were removed by the cleanup software. The resulting velocity fields for each interrogation region provide a window of data 800  $\mu\text{m}$  x 575  $\mu\text{m}$  in size. Fluid velocities ranging from 1 to 516  $\mu\text{m}/\text{s}$  were experimentally measured in the various interrogation regions.

While the PIV results reproducibly captured the in-plane velocity components, the micromixer flow contains significant out-of-plane fluid motion which could not be measured directly using 2D PIV techniques. For example, in the central interrogation region there are clear regions in the center, top left corner, and bottom right corner with very low in-plane velocities. In these regions, there is significant out-of-plane fluid motion where a combination of buoyancy and electrothermal forces drives the flow in vortical patterns up away from the positive electrodes and down towards the negative electrodes. Figure 1.2 depicts a diagram of the device and the experimental setup.

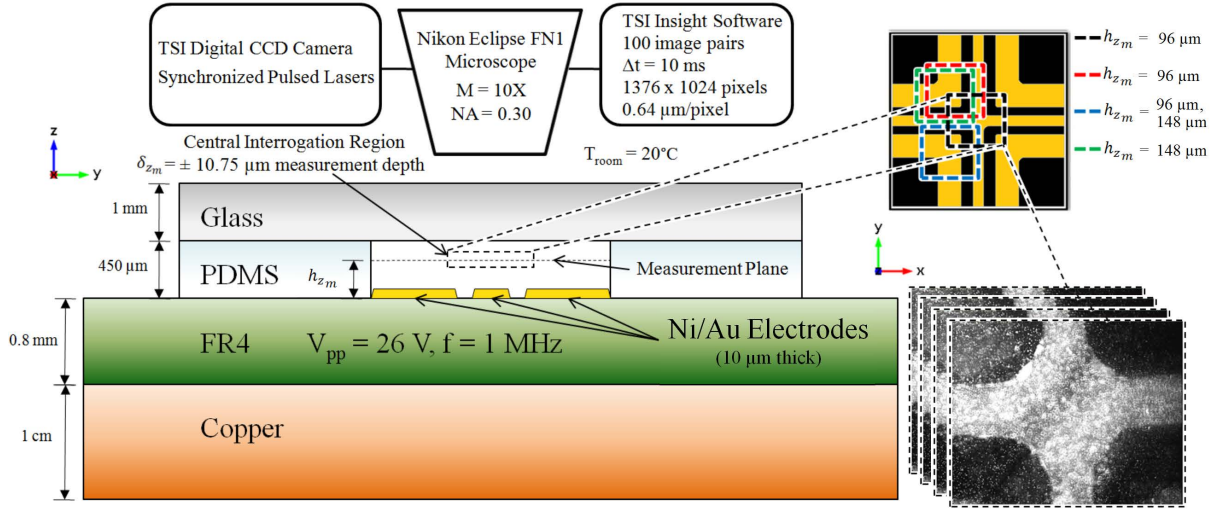


**Figure 1.2:** The experimental setup for the 2D PIV measurements, portraying a cross-sectional side view of the device (left) and a top view of the mixing chamber showing the interrogation region locations (top right). The different interrogation region locations and heights are represented by red, blue, black, and green dashed rectangles. Images of the central interrogation region captured during a PIV experiment are shown (bottom right). Note that the diagram is not to scale.

#### D. Numerical Model

The numerical simulations were performed using *COMSOL Multiphysics v5.1* finite element simulation software to solve the 3D temperature and velocity fields as well as the quasi-static electric fields. The simulated physical equations were based on the theoretical model for ac electrokinetic flows developed by Ramos *et al.*<sup>22</sup> and improved by Loire *et al.*<sup>17</sup> The full enhanced model<sup>17</sup> presents a simplified and coupled set of temperature-dependent equations for use in situations where the maximum estimated temperature rise, derived from scaling laws and given by  $\Delta T \sim \sigma_m V_{pp}^2 / (8k_m)$ , is greater than 5°C. For our experimental conditions, this order of magnitude estimate is approximately 20°C, suggesting that temperature coupling is necessary.

The governing equations were derived from Gauss's Law and charge conservation, the Joule heating equation, and the Stokes equations. The Joule heating equation and the Stokes

equations were solved using the built-in *COMSOL* physics modules of “heat transfer in fluids” and “laminar single-phase flow”, respectively. The temperature boundary conditions for the external surfaces of the modeled device were set to convective heat transfer fluxes with an ambient room temperature of  $T_{\text{room}} = 20^{\circ}\text{C}$ , while the boundary conditions for the solid interior surfaces of the mixing chamber were assigned a no-slip condition where  $\mathbf{u} = 0$ . The temperature-dependent form of the electrical convection-diffusion equation was manually entered and solved using the “coefficient form PDE” module, with RMS voltage boundary conditions on the electrodes and zero flux boundary conditions on the interior walls of the mixing chamber (i.e.  $\partial V / \partial n = 0$ ). Figure 1.3 below shows the boundary conditions and mesh for the numerical model. There were approximately 680,000 elements used in the various domains, discretized by second order elements for the velocity and electric fields, and first order elements for the temperature distribution. More than 550,000 of these elements were used in the mixing chamber alone, where a custom swept mesh was used to resolve fine gradients near the electrodes.

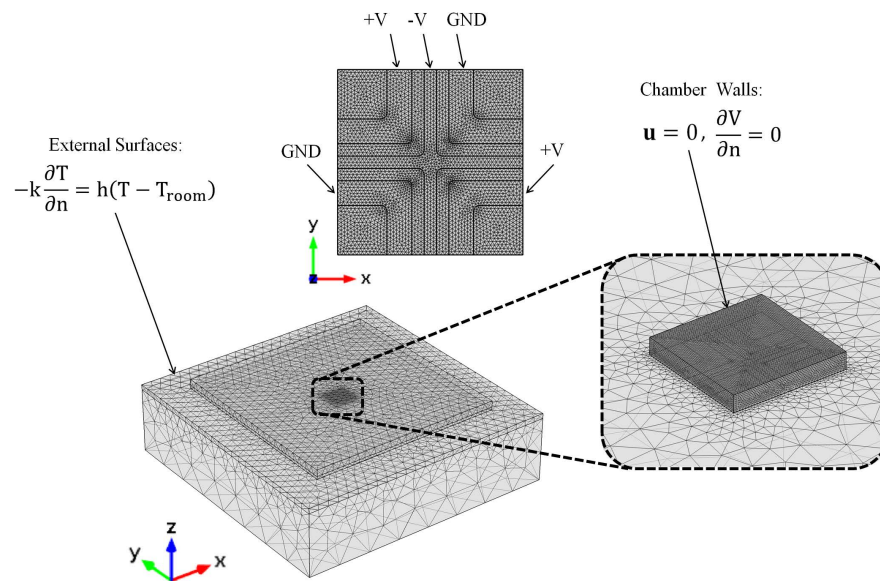


**Figure 1.3:** The mesh and boundary conditions used in the numerical simulation.

The governing equations from Loire *et al.*<sup>17</sup> are presented below in (1.1),

$$\begin{cases} \nabla^2 \tilde{V} = c_\sigma \nabla T \cdot \nabla \tilde{V}, & \tilde{\mathbf{E}} = -\nabla \tilde{V} \\ \rho(T) C_p(T) \mathbf{u} \cdot \nabla T = \nabla \cdot (k_m \nabla T) + \frac{\sigma_m(T)}{2} |\tilde{\mathbf{E}}|^2, \\ \nabla \cdot \left[ \eta_m(T) (\nabla \mathbf{u} + (\nabla \mathbf{u})^T) \right] + \mathbf{F} = \nabla P, & \nabla \cdot \mathbf{u} = 0 \end{cases} \quad (1.1)$$

where  $\tilde{\mathbf{E}}$  is the complex electric field vector,  $\tilde{V}$  is the complex electric potential,  $T$  is temperature,  $\mathbf{u}$  is velocity vector,  $P$  is the fluid pressure,  $\rho(T)$ ,  $C_p(T)$ ,  $\sigma_m(T)$ ,  $\eta_m(T)$ , and  $k_m(T)$  are respectively the temperature-dependent density, specific heat, electrical conductivity, dynamic viscosity, and thermal conductivity of the medium, and  $c_\sigma$  is a rate constant used in the calculation of the temperature-dependent electrical conductivity. For experiments involving most ACET devices, including those described here, only the real part of the electric field and potential are nonzero due to a phase difference of 0 or  $\pi/2$  between electrodes.<sup>17</sup> Empirically-based temperature-dependent functions in *COMSOL Multiphysics* were used for the fluid density, specific heat, viscosity, and thermal conductivity to evaluate these properties in the simulation. Due to a lack of available information about the specific material properties of PBS solutions, these thermal properties were modeled as those of water. The electrical conductivity and permittivity of the aqueous fluid medium were approximated as linear, temperature-dependent equations described by  $\sigma_m(T) = \sigma_m(T_0) [1 + c_\sigma (T - T_0)]$  and  $\varepsilon_m(T) = \varepsilon_m(T_0) [1 + c_\varepsilon (T - T_0)]$ , respectively, where  $c_\sigma = \frac{1}{\sigma_m(T_0)} \left( \frac{\partial \sigma_m}{\partial T} \right) \Big|_{T=T_0} \approx 0.02^\circ \text{C}^{-1}$ ,  $c_\varepsilon = \frac{1}{\varepsilon_m(T_0)} \left( \frac{\partial \varepsilon_m}{\partial T} \right) \Big|_{T=T_0} \approx -0.004^\circ \text{C}^{-1}$ , and  $T_0$  is a reference temperature.<sup>23</sup> The parameter  $c_\sigma$  is used in (1.1) instead of  $c_\varepsilon$  because the charge

relaxation time for our experiments, given by  $\tau = \frac{\varepsilon_m(T_0)}{\sigma_m(T_0)}$ , is much less than the period of the applied AC signal.<sup>17</sup>

The net external body forces include the time-averaged electrothermal force, the buoyancy force, and the dielectrophoretic force. The force  $\mathbf{F}$  used to solve the Stokes equations consists only of the electrothermal force and the buoyancy force, the equations for which are shown in (1.2). Since the dielectrophoretic force acts on polarizable particles, this term was not used directly in the solution of the Stokes equations. Instead, the dielectrophoretic velocity was calculated independently with (1.3) and used to correct the numerically solved velocity field to account for the presence of DEP forces on tracer particles.<sup>24</sup> This equation was obtained by equating the dielectrophoretic force to the Stokes drag force on a spherical particle in a low Reynolds number flow, and solving for the velocity of the fluid relative to the particle as a function of the DEP force. This force is directly proportional to the permittivity of the fluid medium and the cube of the particle radius  $r_p$ . It is also proportional to the gradient of the squared RMS electric field and the Clausius-Mossotti Factor, which is the complex term in (1.3). This term accounts for the frequency dependence of the fluid medium and tracer particle permittivity due to field-induced dipoles. The complex permittivity equations for the particles and fluid medium are given by  $\varepsilon_p^* = \varepsilon_p - j\sigma_p / \omega$  and

$$\varepsilon_m^* = \varepsilon_m - j\sigma_m / \omega. \text{ }^{24}$$

$$\left\{ \begin{array}{l} \mathbf{F} = \mathbf{F}_{\text{ET}} + \mathbf{F}_{\text{B}} \\ \mathbf{F}_{\text{ET}} = \frac{\varepsilon_m(T)}{2} \left[ (c_\varepsilon - c_\sigma)(\nabla T \cdot \tilde{\mathbf{E}})\tilde{\mathbf{E}} - \frac{1}{2}c_\varepsilon \nabla T |\tilde{\mathbf{E}}|^2 \right], \\ \mathbf{F}_{\text{B}} = \rho(T)\mathbf{g} \end{array} \right. \quad (1.2)$$

$$\left\{ \begin{array}{l} \mathbf{F}_{\text{DEP}} = 2\pi\epsilon_m(T)r_p^3 \left[ \text{Re} \left( \frac{\epsilon_p^* - \epsilon_f^*}{\epsilon_p^* + 2\epsilon_f^*} \right) \nabla |\tilde{\mathbf{E}}|^2 \right] \\ \mathbf{U}_{\text{DEP}} = \frac{\mathbf{F}_{\text{DEP}}}{6\pi r_p \mu(T)} \end{array} \right. \quad (1.3)$$

To account for the effect of the finite experimental measurement depth of the microscope on the experimental velocity fields, we introduce a Gaussian window function to sample the simulated velocity field based on vertical distance from the measurement plane. Since the tracer particles in the experiments go out of focus when they move sufficiently far from the focal plane, the Gaussian window function provides an analogous effect on the 3D velocity field by allowing for tunable depth-averaging with the use of a linear projection operation in the simulation. The simulation therefore mimics the image capturing aspect of the PIV experiments by only looking at velocities near the measurement plane and linearly projecting the results on a 2D horizontal plane. Both the width and location of this Gaussian function were used as control parameters for the optimization algorithm to account for any uncertainty in the measurement depth and focal plane location.

### *E. Optimization*

The initial simulation results show qualitative agreement with the experimental measurements. However, the quantitative accuracy of these results is limited due to uncertainties in material properties and the voltage drop from the impedance of the fluid-electrode interface. In order to achieve better agreement between simulation and experiment, we minimize the mean squared error through a gradient-free Nelder-Mead optimization algorithm. We quantify the error using the normalized mean squared error, which represents the square of the ratio of the area-averaged velocity error to the area-averaged velocity

magnitude. This equation, which was used as the objective function in the optimization algorithm, is shown below in equation (1.4),

$$Objective = \frac{\sum \left[ (u_{PIV} - u_{model})^2 + (v_{PIV} - v_{model})^2 \right]}{\sum \left[ (u_{PIV})^2 + (v_{PIV})^2 \right]}. \quad (1.4)$$

The gradient-free Nelder-Mead optimization algorithm was chosen to allow for the potential use of control parameters that require the model to re-mesh between successive iterations. In addition to the location and width of the Gaussian pulse function, the optimization control parameters included linear scaling factors for material properties that are not known with a high degree of certainty, such as the electrical conductivity of the PBS solution and the anisotropic thermal conductivity components of the FR4 printed circuit board. By constraining the control parameters to vary by an appropriately small amount, we are able to ensure that the results are physically reasonable. A voltage scaling factor was also introduced to account for differences between the nominally applied voltage and the voltage actually applied due to impedance mismatch or signal attenuation. Objective functions from five different interrogation regions, three at a height of 96  $\mu\text{m}$  and two at a height of 148  $\mu\text{m}$ , were calculated. The objective function for the central interrogation region was used during optimization, while the other objective functions were used to validate the approach without introducing curve-fitting. A diagram showing the general procedure for the optimization routine is shown below in Figure 1.4.

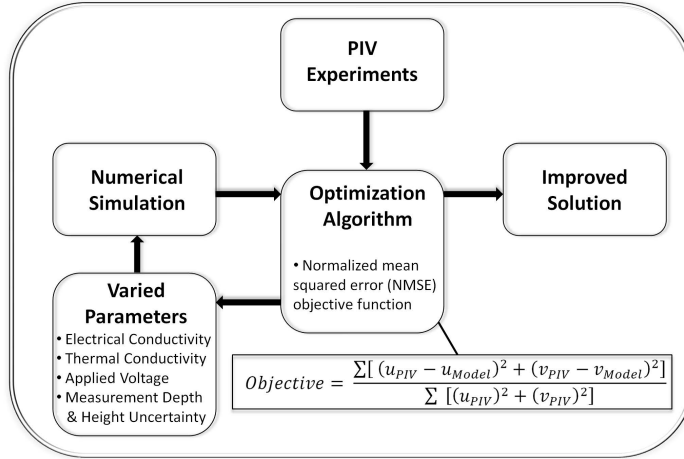


**Figure 1.4:** The steps taken in the optimization process. An initial simulation with the best guess of parameters is compared with experimental results, providing a quantitative measure of the error that can be used as an objective function and subsequently minimized by varying several control parameters. The ultimate result is a simulation that more accurately represents the experimental data.

### ***F. Results***

The resulting temperature profile at the bottom of the mixing chamber for the optimized results indicates that the maximum calculated temperature rise was about 9°C, which is higher than the  $\Delta T \approx 5^\circ\text{C}$  suggested by Loire *et al* to necessitate the use of the fully coupled ACET model. The highly temperature-dependent physical properties of electrical conductivity and dynamic viscosity change by approximately 20% with a temperature rise of around 10°C, so it is important to take these effects into account in the numerical model.<sup>17</sup>

Measurement plane results for the 2D velocity fields from the PIV central interrogation region, the original simulation, and the optimized simulation are shown in Figure 1.5. The original results qualitatively match the experimentally-measured flow pattern. However, the velocity magnitude differs about by an order of magnitude in some regions of the flow. The optimized velocity field shows a significant improvement, as both the velocity magnitude and direction are in excellent agreement with the experimental PIV measurements. The major flow features in the optimized results, such as the saddle point in the center of the device and

the flow reversal regions that represent vertical fluid motion in the top left and bottom right corners, are nearly indistinguishable from those in the PIV results. The low in-plane velocity in these regions suggests that the flow between positive and negative electrodes is substantially vertical, indicating the presence of strong buoyancy and electrothermal forces due to high temperature gradients and intense electric fields. Figure 1.6 shows top views of the optimized results with streamlines, which illustrate the directional flow patterns at the measurement plane more clearly. Also shown is an overlay of 2D in-plane streamlines from the simulation and experimental results to demonstrate the agreement in flow direction between the experimental data and overlapping sections of the three interrogation regions at  $h_{z,m} = 96 \mu\text{m}$ .

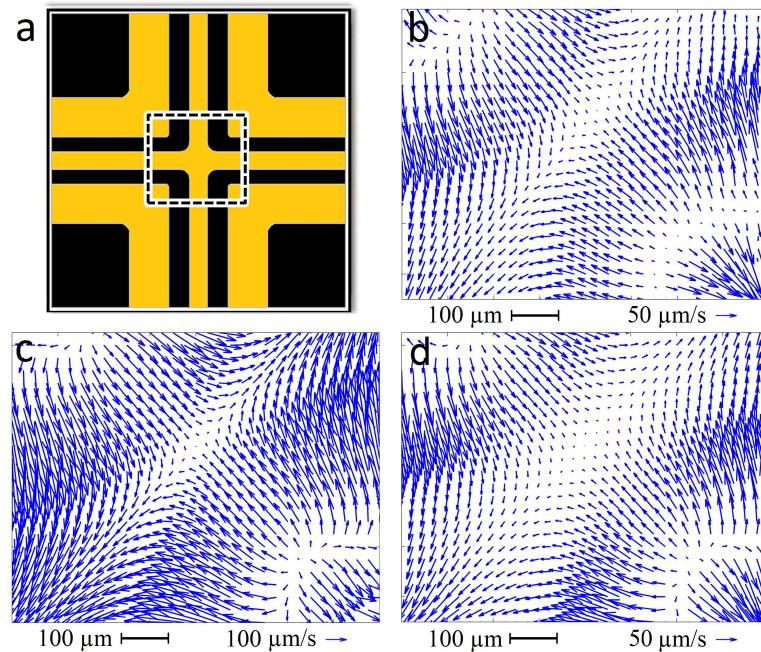


**Figure 1.5:** (a) The electrode pattern with an overlay of the central interrogation region location, (b) a top view of the fully processed PIV data from the central interrogation region, (c) *COMSOL* simulation results of the 2D velocity field at the measurement plane for the original estimation of parameters, and (d) optimized *COMSOL* 2D velocity field at the measurement plane. Each of the velocity fields depicts regions of reversed flow in the top left and bottom right corners and a saddle point in the center. However, the optimized solution clearly has a much closer velocity magnitude to that in (b).

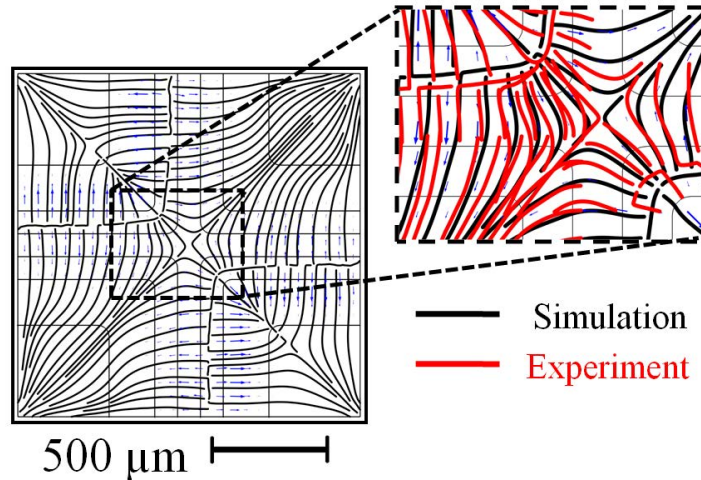


**Figure 1.6:** Velocity field and streamlines for the optimized results. The streamlines depict the flow reversal regions and the saddle point from Figure 1.5, and indicate the general 2D flow pattern for the device at the measurement plane. The results show close agreement between the experiment and simulation for parts of three different interrogation regions.

With more accurate in-plane velocity results, we can generate more reliable out-of-plane information from the 3D simulation. Figure 1.7 below depicts a vertical plane through the center of the micromixer that cuts across the negative and positive electrodes. These velocity streamlines portray the characteristic behavior of the flow above and between the electrodes. The regions where the vortices meet between the positive and negative electrodes correspond to the top left and bottom right corner regions shown in Figure 1.5 where the direction of the in-plane flow changes due to vertical circulation, while the vortices directly above the negative electrode represent the saddle point visible in the center of the 2D velocity measurements.

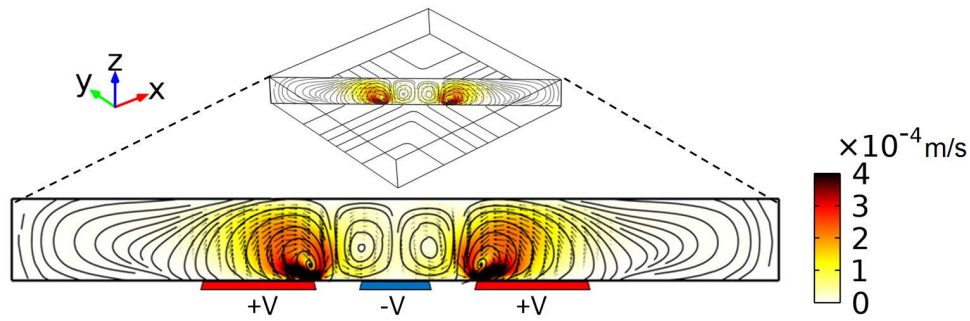


**Figure 1.7:** Out-of-plane optimized velocity magnitude and streamlines for a vertical plane spanning diagonally across the center of the device. The location of the plane within the micromixer is shown, and the locations of the electrodes on the projected plane are indicated by red for the positive electrode and blue for the negative electrode. The out-of-plane fluid circulation patterns contain features depicted in Figures 1.5 and 1.6, such as the corner flow reversal regions and the saddle point in the center.

In addition to 2D in-plane and out-of-plane results, we can obtain smooth 3D velocity field information such as the streamlines shown in Figure 1.8. This information, along with the 2D velocity field results, provides enough information to estimate the general 3D flow patterns of the device under experimental conditions. The 3D streamlines show more detail about the theoretical trajectories of the experimental tracer particles throughout the device, verifying that most of the fluid motion does indeed result from the recirculation between charged electrodes caused by the relatively high level of joule heating there. By periodically switching the voltages applied to the electrodes, more effective mixing and dispersion could potentially be induced within the device. With knowledge of these flow field results, a particle tracing simulation can be generated to visually recreate the motion of the tracer particles in the PIV experiments. The numerical 3D velocity, temperature, and electric field data can also be exported for further computational analysis of these mixing devices. Figure 1.8 shows that the optimized maximum velocity magnitude is within the range of those measured experimentally.

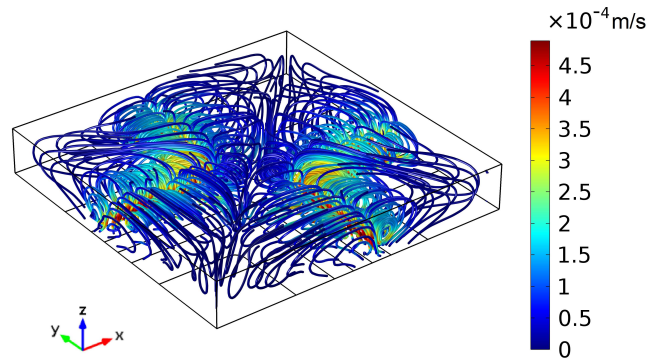


**Figure 1.8:** Velocity streamlines for the optimized flow conditions in the mixing chamber, in m/s. These streamlines effectively represent the theoretical 3D trajectories of the tracer particles in the PIV experiments. The general flow pattern did not change significantly through optimization, but the average flow speed was reduced by almost an order of magnitude.

The original and optimized control parameters are presented in Table 1.1, and a plot of the pre- and post-optimization results for each of the five interrogation regions is shown in Figure 1.9. These results show that the normalized root-mean-square error (NRMSE) was reduced by factors of up to 11.4 through optimization, with the target region NRMSE reduced by a factor of 4.2. A comparison of the original and optimized parameters shows how the relevant physical properties were scaled to match experimental flow conditions, as well as how the image measurement parameters were slightly altered to achieve a better fit between experimental and numerical results. The optimized width of  $\pm 9.9 \mu\text{m}$  for the Gaussian measurement depth function was close to the theoretical measurement depth  $\pm 10.75 \mu\text{m}$  for the objective lens and fluorescence method used.<sup>20</sup> The optimized measurement plane location offset of less than  $20 \mu\text{m}$  was also reasonably close to the expected value, suggesting an initial measurement plane height uncertainty less than 5% of the chamber height.

Scaling of the material properties, some of which are sensitive to exact composition and can thus vary considerably, shows that optimization reduced the electrical conductivity of the PBS solution by approximately 15% to better match experimental data. The optimized

electrical conductivity of  $\sigma_m(T_0) = 1.64$  mS/cm at 20°C was close to the expected value of 1.9 mS/cm, which was initially estimated through conductivity measurements of previously prepared PBS solutions. This scaled result is consistent with the value of 1.79 mS/cm at 23.5°C previously reported in literature when the linear approximation for the temperature dependent electrical conductivity is taken into account.<sup>25</sup> The initial anisotropic thermal conductivity components of the FR4 printed circuit board proved to be slightly lower than the values which ultimately provided a better fit to experimental flow conditions. These values were also in the range of reported values,<sup>26</sup> while the slight drop in effective applied voltage was to be expected because the impedance effects of the electrode and fluid were not investigated or modeled.

**Table 1.1:** Original and optimized control parameters.

<b>Parameter</b>	<b>Original</b>	<b>Optimized</b>
Fluid Electrical Conductivity	1.9 mS/cm	1.64 mS/cm
Applied RMS Voltage	9.19 V	8.91 V
Gaussian Function Width	$\pm 5$ $\mu\text{m}$	$\pm 9.9$ $\mu\text{m}$
Measurement Plane Location Offset	0	-19.5 $\mu\text{m}$
FR4 Thermal Conductivity, x-direction	0.8 W m <sup>-1</sup> K <sup>-1</sup>	0.86 W m <sup>-1</sup> K <sup>-1</sup>
FR4 Thermal Conductivity, y-direction	0.8 W m <sup>-1</sup> K <sup>-1</sup>	0.86 W m <sup>-1</sup> K <sup>-1</sup>
FR4 Thermal Conductivity, z-direction	0.3 W m <sup>-1</sup> K <sup>-1</sup>	0.32 W m <sup>-1</sup> K <sup>-1</sup>

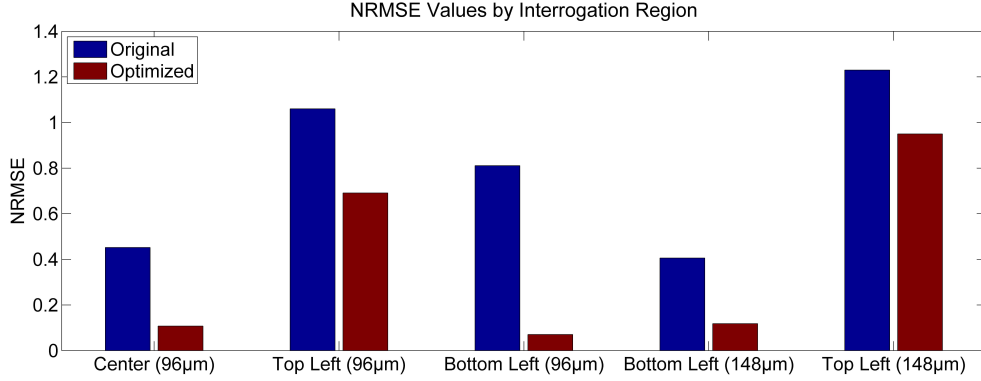


**Figure 1.9:** Optimization results, showing the normalized RMS velocity error between the simulation results and PIV measurements for the each interrogation region. These results indicate that the relative error between the RMS velocity error and RMS velocity for the optimized results is only 0.115 for the central interrogation region; that is, the optimized RMS error is less than 12% of the RMS velocity, compared to an RMS error more than 45% of the RMS velocity for the non-optimized solution. Results from other interrogation regions all showed reductions in error, indicating that the remaining regions of the velocity field at both measurement planes are also an improved fit with the experimental results despite not explicitly being included in the objective function for optimization.

We can gauge the efficacy of the micromixer under various conditions by simulating the transport of an uncharged species via a convection-diffusion species conservation equation,

$$\frac{\partial c}{\partial t} + \mathbf{u} \cdot \nabla c = D \nabla^2 c, \quad (1.5)$$

where  $c$  and  $D$  are the species concentration and diffusion coefficient, respectively. This equation is bounded by fixed concentration inlet conditions at the bottom surface of the device and no flux conditions at the remaining walls of the mixing chamber.

Volume-averaged concentration profiles within the mixing chamber are shown in Figure 1.10 for a peak-to-peak voltage range between 0 and 60 V for a sample with diffusivity  $D = 5 \times 10^{-10} \text{ m}^2 \text{ s}^{-1}$ . The limiting case of zero voltage applied represents pure diffusion, and exhibits the typical shape of a temporal diffusion time profile. By changing the peak-to-peak voltage, we can control the level of Joule heating and the resulting temperature gradients that are

produced to either enhance or diminish the influence of buoyancy and electrothermal effects on the flow.

At our fluid conductivity and applied voltage range, electrothermal effects scale with  $V_{pp}^k$ , where  $k$  is between 4 and 5, while buoyancy scales with  $V_{pp}^2$  and is more dependent on the length scale.<sup>17</sup> One could ostensibly use this information to tailor the device and experimental conditions to the needs of the particular application. For biological samples that may be sensitive to temperature changes, a lower voltage can be applied to induce predominantly buoyancy-driven flow. Conversely, for processes which may require thermal cycling at higher temperatures, a higher conductivity buffer could be used at relatively high voltages to produce more Joule heating and create stronger fluid circulation patterns.

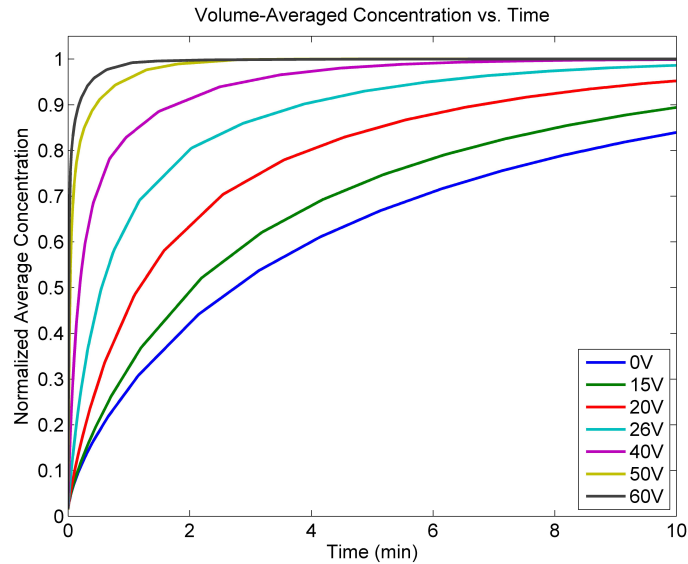


**Figure 1.10:** Average normalized sample concentration in the micromixer over time as a function of the applied peak-to-peak sinusoidal voltage. Higher voltage signals can provide greater than an order of magnitude reduction in mixing time due to the increased convective dispersion, but at the cost of a higher operating temperature.

### ***G. Conclusion***

In this chapter, we introduced a hybrid experimental-numerical optimization technique for estimating 3D velocity vector fields from planar 2D PIV data. This method provides an alternative to 3D PIV and data-intensive 2D techniques, allowing us to easily generate simulated 3D velocity fields that are consistent with 2D experimental measurements. The implementation of this least-squares optimization algorithm to 2D PIV measurements of an electrothermal micromixer resulted in greater than a factor of 4 reduction in the normalized RMS velocity error between the simulation and experimental results in the target region. In addition, the hybrid approach can help determine experimental parameters or material properties that are not well known *a priori*. The optimization algorithm reduced the simulated flow speed significantly throughout the micromixer, providing a more accurate estimation of the complete 3D fluid motion by scaling several control parameters to match the experimentally determined best estimate of the 2D measured velocities. These scaled parameters were physically reasonable, as the resulting PBS electrical conductivity and the FR4 thermal conductivity components were consistent with those previously reported in literature. This hybrid method shows promise in developing simulations that can more accurately reflect experimental conditions and predict mixing capabilities, and has potential applications in the modeling of other flow measurement-related research where the dominant physical effects are well characterized and understood.

### ***H. Acknowledgement***

This research was supported in part by the Institute for Collaborative Biotechnologies through grant W911NF-09-0001 from the U.S. Army Research Office, ONR MURI grant N00014-11-1-0087, and ARO-MURI grant W911NF-14-1-0359. The content of the

information does not necessarily reflect the position or the policy of the Government, and no official endorsement should be inferred. The authors would also like to thank the California NanoSystems Institute Microfluidics Lab on the campus of the University of California, Santa Barbara for allowing us to use the laboratory facilities in the fabrication of the experimental devices.

## References

1. González A, Ramos A, Morgan H, Green N G and Castellanos A 2006 Electrothermal flows generated by alternating and rotating electric fields in Microsystems *J. Fluid Mech.* **654** 415-33.
2. Sigurdson M, Wang D and Meinhart C D 2005 Electrothermal stirring for heterogeneous immunoassays *Lab on Chip* **5** 1366-73.
3. Sasaki N, Kitamori T and Kim H 2012 Fluid mixing using AC electrothermal flow on meandering electrodes in a microchannel *Electrophoresis* **33** 2668-73.
4. Ng W Y, Goh S, Lam Y C, Yang C and Rodríguez I 2009 DC-biased AC-electroosmotic and AC-electrothermal flow mixing in microchannels *Lab on Chip* **9** 802-809.
5. Feng J J, Krishnamoorthy S and Sundaram S 2007 Numerical analysis of mixing by electrothermal induced flow in microfluidic systems *Biomicrofluidics* **1** 024102.
6. Sigurdson M, Chang D E, Tuval I, Mezić I and Meinhart C D 2007 Ac electrokinetics: stirring and focusing of nanoparticles *BioMEMS and Biomedical Nanotechnology* ed M Ferrari *et al* (New York: Springer) pp 243-55.
7. Sin M L Y, Gau V, Liao J C and Wong P K 2010 Electrothermal Fluid Manipulation of High-Conductivity Samples for Laboratory Automation Applications *JALA* **15**(6) 426-32.
8. Ramos A, Morgan H, Green N G, and Castellanos A 1999 AC Electric-Field-Induced Fluid Flow in Microelectrodes *Journal of Colloid and Interface Science* **217**(2) 420-22.
9. Green N G, Ramos A, González A, Castellanos A, and Morgan H 2001 Electrothermally induced fluid flow in microelectrodes *Journal of Electrostatics* **53** 71-87.
10. Soloff S M, Adrian R J and Liu Z-C 1997 Distortion compensation for generalized stereoscopic particle image velocimetry *Meas. Sci. Technol.* **8** 1441-54.

11. Prasad A K 2000 Stereoscopic particle image velocimetry *Exp. Fluids* **29** 103-16.
12. Kauffman P, Loire S, Mezić I, and Meinhart C D “Proper Orthogonal Decomposition based 3D microPIV: application to electrothermal flow study.” 10<sup>th</sup> International Symposium on Particle Image Velocimetry, Delft, The Netherlands, July 1-3, 2013.
13. Bown M R, MacInnes J M and Allen R W K 2007 Three-component micro-PIV using the continuity equation and a comparison of the performance with that of stereoscopic measurements *Exp. Fluids* **42** 197-205.
14. Chen D F and Du H 2006 Simulation studies on electrothermal flow induced in a dielectrophoretic microelectrode system *J. Micromech. Microeng.* **16** 2411-19.
15. Hong F J, Cao J and Cheng P 2010 A parametric study of AC electrothermal flow in microchannels with asymmetrical interdigitated electrodes *International Communications in Heat and Mass Transfer* **38**(3) 275-79.
16. Lee H, Yun S, Ko S H and Kang K H 2009 An electrohydrodynamic flow in ac electrowetting *Biomicrofluidics* **3** 044113.
17. Loire S, Kauffman P, Mezić I, and Meinhart C D 2012 Ac electrokinetics: A theoretical and experimental study of ac electrothermal flows *J. Phys. D: Appl. Phys* **45** 185301.
18. Castellanos A, Ramos A, González A, Green N G, and Morgan H 2003 Electrohydrodynamics and Dielectrophoresis in Microsystems: scaling laws *J. Phys. D: Appl. Phys* **36** 2584-97.
19. Meinhart C D, Wereley S T and Santiago J G 1999 PIV Measurements of a Microchannel Flow *Exp. Fluids.* **27** 414-19.
20. Meinhart C D, Wereley S T and Gray H M B 2000 Volume illumination for two-dimensional particle image velocimetry *Meas. Sci. Technol.* **11** 809-14.

21. Meinhart C D, Wereley S T and Santiago J G 2000 A PIV algorithm for estimating time-averaged velocity fields *J. Fluid Eng.* **122** 285-89.
22. Ramos A, Morgan H, Green N G and Castellanos A 1998 Ac electrokinetics: A review of forces in microelectrodes *J. Phys. D: Appl. Phys* **31** 2338-53.
23. Lide D R 2000 *Handbook of Chemistry and Physics* edition 81 (New York: CRC Press).
24. Liang M “Microfluidic manipulation by AC Electrothermal effect.” PhD diss, University of Tennessee, 2010.
25. Johnson A M, Sadoway D R, Cima M J and Langer R 2005 Design and Testing of an Impedance-Based Sensor for Monitoring Drug Delivery *J. Electrochemical Society* **152** H6-H11.
26. Azar, K; Graebner J. E. 1996 Experimental Determination of Thermal Conductivity of Printed Wiring Boards. *Proceedings of the Twelfth IEEE SEMI-THERM Symposium: 169–182.*

## **II. Nanofluidics: The Electrical Double Layer and Field-Effect Control**

### ***A. Abstract***

It is well known that charged analytes in the presence of nonuniform electric fields concentrate at locations where the relevant driving forces balance, and a wide range of ionic stacking and focusing methods are commonly employed to leverage these physical mechanisms in order to improve signal levels in biosensing applications. In particular, nanofluidic channels with spatially varying conductivity distributions have been shown to provide increased preconcentration of charged analytes due to the existence of a finite electric double layer (EDL), in which electrostatic attraction and repulsion from charged surfaces produce nonuniform transverse ion distributions. In this work, we use numerical simulations to show that one can achieve greater levels of sample accumulation by using field-effect control via wall-embedded electrodes to tailor the surface potential heterogeneity in a nanochannel with overlapped EDLs. In addition to previously demonstrated stacking and focusing mechanisms, we find that the coupling between two-dimensional ion distributions and the axial electric field under overlapped EDL conditions can generate an ion concentration polarization (CP) interface in the middle of the channel. Under an applied electric field, this interface can be used to concentrate sample ions between two stationary regions of different surface potential and charge density. Varying conditions can also lead to downstream field gradients, enabling simultaneous focusing and separation of charged analytes. Our numerical model uses the Poisson-Nernst-Planck system of equations coupled with the Stokes equation to demonstrate the phenomenon, and we discuss in detail the driving forces behind the predicted sample enhancement. The numerical velocity and salt concentration profiles exhibit good agreement with analytical results from a simplified 1D area-averaged model for several limiting cases, and we show predicted amplification ratios of

up to  $10^5$ . This chapter was reproduced in part from Eden *et al.*, *Phys. Rev. Fluids*, **2**, 124203, © 2017 American Physical Society (DOI: 10.1103/PhysRevFluids.2.124203).

### ***B. Introduction***

A constantly evolving understanding of natural biological processes coupled with advances in micro- and nanoscale fabrication technologies has recently spurred the development of myriad novel devices for bioassays, protein and DNA separation/amplification, and other lab-on-chip processes.<sup>1-7</sup> The small scale of these devices introduces many obstacles that must be overcome through engineering prowess, however, and a primary concern in the field remains the necessity for sample analyte preconcentration in bioanalytical micro- and nanofluidic devices.<sup>2,8</sup> Innovative focusing techniques utilizing electrokinetic phenomena such as field-amplified sample stacking (FASS),<sup>8-11</sup> ion concentration polarization,<sup>12-17</sup> isotachopheresis,<sup>18</sup> isoelectric focusing,<sup>19</sup> concentration gradient focusing,<sup>20</sup> and many others have been introduced to address and resolve this prevalent issue. In many such cases, anionic analyte focusing is achieved by exploiting the competition between electroosmotic flow (EOF) and electrophoresis in order to drive the anionic species to a location where the upstream electrophoretic velocity balances the downstream bulk electroosmotic fluid flow.<sup>10,14,16</sup> These enriched ions can then be interrogated, separated, or otherwise manipulated for further downstream processing once the level of sample molecules reaches the threshold limit for the desired application, allowing for increased sensitivity of bioanalytical devices.<sup>12,15</sup>

In traditional field-amplified sample stacking methods, electric field gradients are used to drive analyte ions to an interface between a background solution and an injected plug of lower conductivity fluid.<sup>8</sup> This effect occurs regardless of the EDL thickness, and can thus be

achieved in microscale channels and/or with higher electrolyte concentrations in nanochannels. Sustarich *et al.*<sup>10</sup> discovered that in nanochannels, greater FASS enhancement ratios can be obtained due to flow focusing and electrostatic repulsion of sample ions towards the channel center by finite-sized but non-overlapping EDLs. These FASS techniques produce short-lived enhancement, however, as they require a propagating plug which is prone to diffusion and dispersion due to pressure gradients induced by nonuniform EOF.<sup>9</sup> In the regime of overlapped EDLs, other approaches such as CP leverage the charge-selective nature of EDL structures by generating stationary or propagating “shock” zones of ion accumulation or depletion near permselective microchannel/nanochannel junctions, as first visualized by Pu *et al.*<sup>12</sup> and later described in detail by Mani *et al.*<sup>14</sup> and Zangle *et al.*<sup>15</sup> They found that these CP phenomena are primarily governed by the background electrolyte (BGE) concentration, the analyte mobility, the channel height, the induced surface charge that establishes the electric double layer structure, and the applied electric field strength. All of these factors determine the nature and extent of the observed concentration polarization, and therefore the subsequent analyte preconcentration capabilities of CP-based methods.

Researchers have also previously investigated the effects of nonuniform EOF due to spatially varying surface properties realized through field-effect control and/or various surface treatments. Schasfoort *et al.*<sup>21</sup> first presented a device they designated a “flowFET” which allowed for local zeta potential and electroosmotic flow control through field-effect modulation via a gate electrode near the channel wall. Herr *et al.*<sup>22</sup> later developed a simple 1D model to represent nonuniform EOF in a capillary with a step change in zeta potential due to surface adsorption of an EOF-suppressing polymer. Fu *et al.*<sup>23</sup> investigated a similar configuration of heterogeneous zeta potential in more detail by accounting for local ion distributions and electroosmotic advection using a Nernst-Planck model. More complex

models have since been generalized to represent micro/nanofluidic systems with arbitrary nonuniform surface charge and/or variable heights.<sup>14,16,24</sup> Applications ranging from integrated fluid field-effect transistors to nanofluidic diodes have also emerged following fundamental discoveries reported by researchers such as Karnik *et al.*<sup>25</sup> and Daiguji *et al.*,<sup>26</sup> respectively; as a result of this research and other similar works,<sup>1,27-33</sup> nanofluidic channels with nonuniform surface potential have been shown to exhibit tremendous promise when it comes to controlling the behavior of bulk fluid and individual ions on-demand. Moreover, Jin and Aluru<sup>32</sup> showed that in addition to exhibiting FET properties, nanochannels with wall-embedded electrodes used to tailor the surface charge and potential can be leveraged for variable analyte stacking by tuning the applied gate voltage. To our knowledge, however, no studies to date have investigated in-depth the preconcentration capabilities of nanochannels with nonuniform surface properties achieved through field-effect control.

The remainder of this chapter is organized as follows. In Section C, we introduce the electric double layer and present the underlying governing equations for ion transport in the nanofluidic system, then we describe in detail our 2D numerical model along with the simulated boundary conditions. The preconcentration simulation results are presented in Section D, in which we discuss the causes and limitations of the predicted sample enhancement. We reveal that the mechanisms which lead to sample accumulation are effectively the same as the driving forces behind FASS and CP, as field-effect surface charge modulation can induce axial gradients in the ionic conductivity distribution and generate concentration polarization interfaces between distinct regions of the channel due to large area-averaged EDL gradients. These combined effects are shown to only occur in nanochannels with sufficiently large electric double layers relative to the channel height, and in channels with nonuniform zeta potential. Our results predict achievable sample

enhancement ratios which exceed those from traditional FASS by more than two orders of magnitude.<sup>10,11</sup> Finally, we conclude by summarizing the main points of our findings in Section E.

### ***C. Theoretical and Numerical Framework***

#### **1. Electrical Double Layers and Electroosmotic Flow**

The term “electrical double layer” refers to the spatially distinct regions of an electrolyte solution that comes into contact with a charged surface. This interfacial surface charge can arise naturally, as in the cases of charged species adsorption and physicochemical reactions involving protonation and deprotonation of surface groups, or it can be physically controlled, as with functionalized surfaces. The surface charge can also manifest as a result of surface polarization, either directly by the application of a potential (as with polarizable electrodes or dielectrics), or by interfacial charge transfer during electrochemical reactions.

Regardless of the origin, the charge present at the surface generates an electric field which attracts counter-ions in solution to accumulate near the wall in order to electrostatically screen the surface charge. This region of accumulated ions can be regarded as two separate regions, according to the Guoy-Chapman-Stern model.<sup>2</sup> The first, termed the Stern layer, is a thin layer (~1 atomic layer) of hydrated ions that are effectively adsorbed onto the surface by intense electrostatic attraction. The Stern layer can therefore be thought of as immobilized charge separated by a distance equal to the hydrated radius of a counter-ion (see Figure 2.1). Under the assumption of no specific adsorption the space between the immobilized charge consists only of solvent molecules, and the electrostatic potential consequently varies linearly from the surface potential to the potential at the interface between the Stern layer and the second EDL layer; this second layer is called the diffuse

layer. The Stern layer/diffuse layer interfacial potential is referred to as the zeta potential, and is an important parameter that governs EDL composition and coupled effects such as EOF. The diffuse layer is dominated by counter-ions which are still attracted to the charged surface, but experience a sufficient counter-directional diffusive flux from ions nearer the surface to prevent additional accumulation. Thus, an equilibrium EDL is characterized by the balance of electrostatic forces and diffusion at every point in the diffuse layer; the potential distribution therefore decays exponentially away from the Stern/diffuse layer interface. Outside the diffuse layer is a bulk region in which the electrostatic potential arising from the wall charge is zero, indicating the absence of any local attractive or repulsive forces on ions due to full electrostatic screening of the wall charge by the EDL.

When this electrical double layer structure is subjected to a tangential electric field, Coulombic forces cause the net ionic charge present in the EDLs to migrate along the tangential field and carry fluid along with it by viscous drag. Since the Coulombic forces act only on *net* charge (regions where there is an imbalance between cationic and anionic charge – i.e. the EDL), this force is equal to zero in the bulk solution and the fluid in this region therefore only moves by viscous shear from the EDL motion. This leads to the development of an electroosmotic flow velocity profile which is equal to zero at the Stern layer/diffuse layer interface (also referred to as the shear plane) and which becomes uniform in the bulk region (Figure 2.1). The velocity profile is determined, in part, by the wall zeta potential, as this correlates with the ionic charge imbalance in the EDL and thus the electrostatic body force which causes fluid motion. Note that a nonuniform zeta potential distribution will lead to regions of fluid which naturally want to move faster and slower in certain regions due to the nonuniform forces acting on the fluid, but mass conservation requires that the flow rate is uniform everywhere for an incompressible fluid. Thus, internal pressure gradients must be

induced in order to speed up and slow the flow locally, where necessary, in order to ensure continuity. The full velocity profile for electroosmotic flow should therefore be regarded as a combination of pressure-driven flow and EOF; for simplicity, we will refer to this combination as “the EOF profile” for the remainder of this chapter.

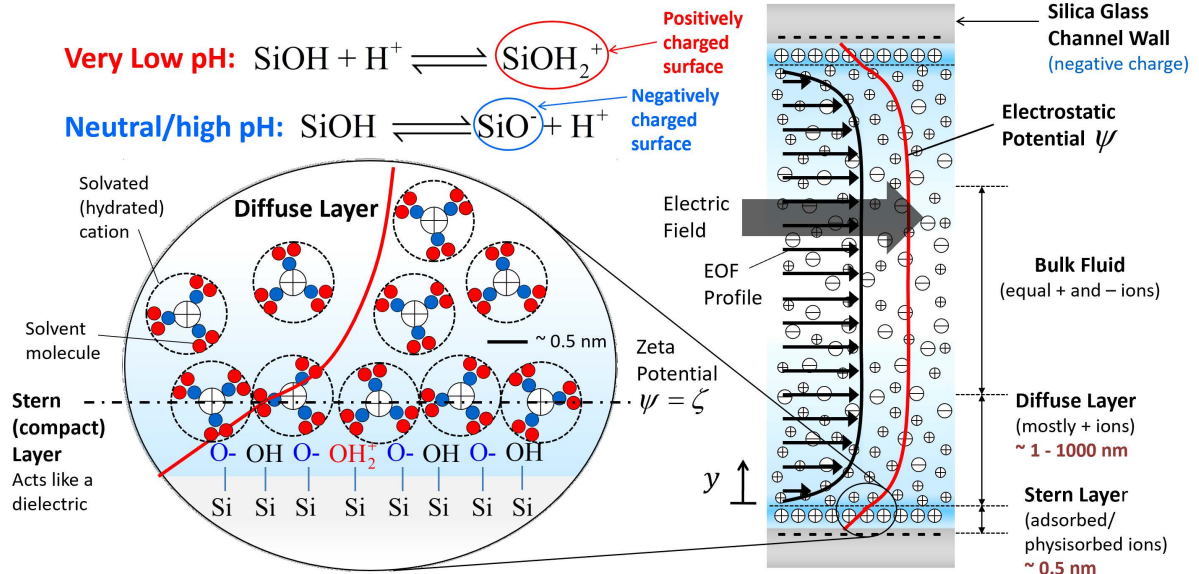


**Figure 2.1:** Schematic of an electrical double layer in a glass channel.

## 2. Nanofluidic Device

The system we are modeling consists of a nanofluidic channel with embedded, addressable electrodes along half of the channel length (see Figure 2.2). These gate electrodes, which are isolated from the fluid within the channel by a thin dielectric layer, allow for field-effect modulation of the local surface charge density and electric potential at the fluid/solid interface in this region of the channel. The nanochannel connects two reservoirs which are significantly larger than the channel and are filled with a solution of background electrolyte ions. In nanofluidic systems such as this, high geometric aspect ratios

generally result in channels with very small height-to-width ratios ( $H/W \ll 1$ ), and therefore a depth-averaged 2D analysis is a reasonable approximation of the transport conditions.

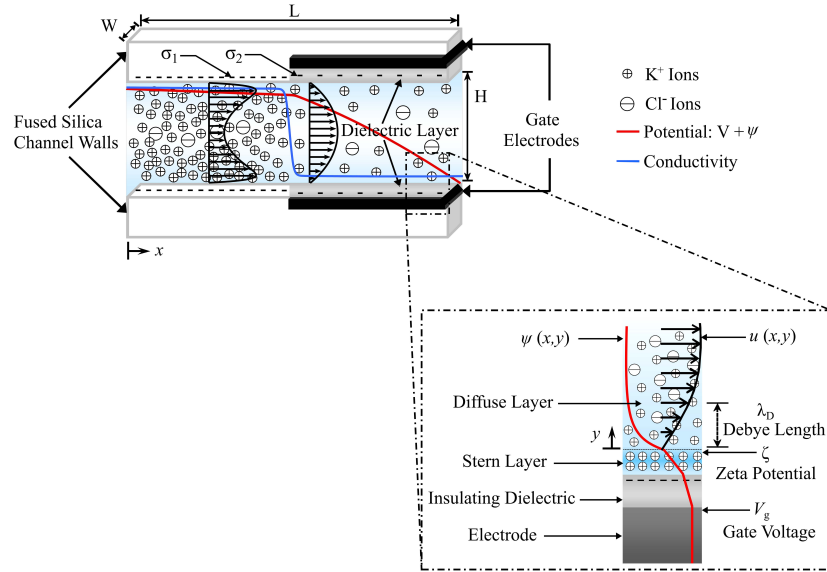


**Figure 2.2:** Diagram of the described nanofluidic device with embedded electrodes in the top and bottom channel walls, showing example ion distributions in a channel with modified surface charge and potential (top center), as well as the EDL potential and velocity profiles near an embedded electrode (bottom right).

### 3. Governing Equations and 2D Numerical Model

The foundation for ion transport within the channel is the Poisson-Nernst-Planck system of equations, which accounts for the local ion distributions arising from electrostatic interactions with the charge-regulated channel walls. These equations are coupled with the Navier-Stokes equations to account for the advective transport of ions through the channel due to electroosmotic flow from an applied electric field.<sup>23,24</sup> Since the nanofluidic channel is long and thin, it is convenient to separate the local electrostatic potential of the fluid into a potential  $V$  associated with the applied electric field, which varies in the axial direction inside the channel, and an intrinsic EDL potential  $\psi$  which can vary in both the axial and transverse directions for nonuniform EOF cases. Separating the EDL and applied potentials in this

manner facilitates comparison between our numerical simulations and the 1D area-averaged verification model presented in the supplemental material,<sup>34</sup> and is similar to the approach found in previous works which assume that the EDLs are in equilibrium in the transverse direction<sup>14,24,32</sup> but can vary in the axial direction due to effects such as CP.

We use Poisson's equation to relate the electrostatic potential distribution throughout the fluid to the spatial free charge density of ions in solution,

$$-\nabla \cdot [\varepsilon_0 \varepsilon_f \nabla (V + \psi)] = \rho_E, \quad (2.1)$$

where  $\varepsilon_0$  is the permittivity of free space,  $\varepsilon_f$  is the dielectric constant of the electrolyte solution (assumed to be a constant  $\varepsilon_f = 80.1$ ),  $\rho_E$  is the local volumetric charge density,  $V$  is the potential associated with an applied electric field, and  $\psi$  is the local EDL potential. The charge density  $\rho_E$  effectively represents the net free charge present due to a local imbalance of cations and anions in solution, and can be expressed as  $\rho_E = F \sum_{i=1}^m z_i c_i$ , where  $F$  is Faraday's constant,  $z_i$  is the ion valence of species  $i$ ,  $c_i$  is the molar concentration, and  $m$  is the number of species in solution. Following previous works, we assume that the concentration of sample ions is much lower than the BGE ion concentrations, such that the sample has a negligible influence on the charge density.<sup>10,15</sup> The local potential  $V + \psi$  is specified to be equal to an applied potential at the top boundary of the inlet reservoir and grounded at the top boundary of the outlet reservoir, while the EDL potential  $\psi$  is locally equal to the zeta potential  $\zeta$  at the channel and reservoir walls. As reported by Stein *et al.*,<sup>35</sup> the resulting surface charge can be related to the potential gradient at the wall using the relation  $\sigma_s = \mathbf{n} \cdot \nabla (\varepsilon_0 \varepsilon_f \psi)$ , where  $\mathbf{n}$  is the outward surface normal unit vector.

The concentrations of background electrolyte ions and ionic sample species within the channel and reservoirs are determined using mass conservation. Extending Fick's macroscale diffusion law to account for electroosmotic advection as well as transverse and axial electromigration of ionic species in a dilute BGE solution, we define the mass conservation equation for species  $i$  as

$$\frac{\partial c_i}{\partial t} = -\nabla \cdot [\mathbf{u}c_i - D_i \nabla c_i - \mu_i z_i F c_i \nabla (V + \psi)], \quad (2.2)$$

where  $D_i$  is the ion diffusivity,  $\mu_i$  is the electrophoretic mobility, and  $\mathbf{u}$  is the fluid velocity. The convective flux  $\mathbf{u}c_i$  accounts for ion transport due to electroosmotic advection, while the diffusive flux  $-D_i \nabla c_i$  represents ion diffusion in the presence of a local concentration gradient. The combined electromigration flux  $-\mu_i z_i F c_i \nabla (V + \psi)$  accounts for axial and transverse migration from variations in the EDL potential  $\psi$ , as well as the additional axial electromigration once an applied potential  $V$  is introduced across the channel. Therefore, the total flux of species  $i$  is given by  $\mathbf{N}_i = \mathbf{u}c_i - D_i \nabla c_i - \mu_i z_i F c_i \nabla (V + \psi)$ . As a consequence of equation (2.2), the net current density  $\mathbf{J} = F \sum_{i=1}^m z_i \mathbf{N}_i$  associated with BGE ion transport is divergence free at steady state.

We consider a dilute binary background electrolyte solution where  $c_+$  is the cation concentration,  $c_-$  is the anion concentration, and  $c_s$  is the sample species concentration. The ion mobilities are calculated using the Nernst-Einstein mobility equation  $\mu_i = D_i / (RT)$ , where  $R$  is the universal gas constant and  $T$  is the solution temperature, assumed to be fixed at  $20^\circ \text{C}$ . The boundary conditions associated with equation (2.2) include bulk concentration

Dirichlet conditions  $c_i = c_{i,\infty}$  and  $c_s = c_0$  for the BGE and sample species, respectively, at the reservoir inlet and outlet. A zero normal species flux condition  $\mathbf{n} \cdot \mathbf{N}_i = 0$  is enforced at the solid walls of the nanochannel and reservoirs, which are assumed to be impermeable.

Finally, the inherently low Reynolds number associated with nanofluidic flows allows us to use the incompressible form of the Stokes' equation and the continuity equation to describe the steady state conservation of momentum within the nanochannel for a fluid experiencing a Coulombic body force due to a nonzero free charge distribution,

$$0 = \eta \nabla^2 \mathbf{u} - \nabla P - \rho_E \nabla (V + \psi); \quad \nabla \cdot \mathbf{u} = 0 \quad (2.3)$$

where  $P$  is the pressure within the fluid and  $\eta$  is the dynamic viscosity of the fluid. The fluid gauge pressure relative to atmosphere is specified to be zero at the inlet and outlet of the reservoirs, while a no slip condition  $\mathbf{u} = 0$  is enforced at the nanochannel and reservoir walls.

We use COMSOL v5.1 to numerically simulate the highly coupled, nonlinear system of equations (2.1)-(2.3). Since we assume a very dilute sample concentration, we first solve for the final steady state transport conditions in the BGE and then use these results to separately solve for the temporal and steady state concentrations of the sample species. Our model also assumes a fixed surface potential at the walls and constant ion mobilities, both of which are often used in analytical and numerical models but are not always found to be true in practice.<sup>35,39</sup> We included fluid reservoirs located at the channel inlet and outlet in order to allow for a more realistic treatment of the boundary conditions at the free surface of the fluid (see Figure 2.3), as well as to account for any concentration polarization effects at the channel inlet and outlet. The zeta potential along the channel was modeled as a smoothed, continuous step function which transitions over  $\delta = 5\text{nm}$ . The unmodified wall zeta potentials are chosen to be representative of previously reported values for various pH and electrolyte

concentrations,<sup>36</sup> while the gate voltages required to produce the desired modified zeta potentials are estimated for future experimental verification using the theory of Hughes *et al.*<sup>37</sup> for non-overlapped EDLs and the theory of Yeh *et al.*<sup>38</sup> for overlapped EDLs.

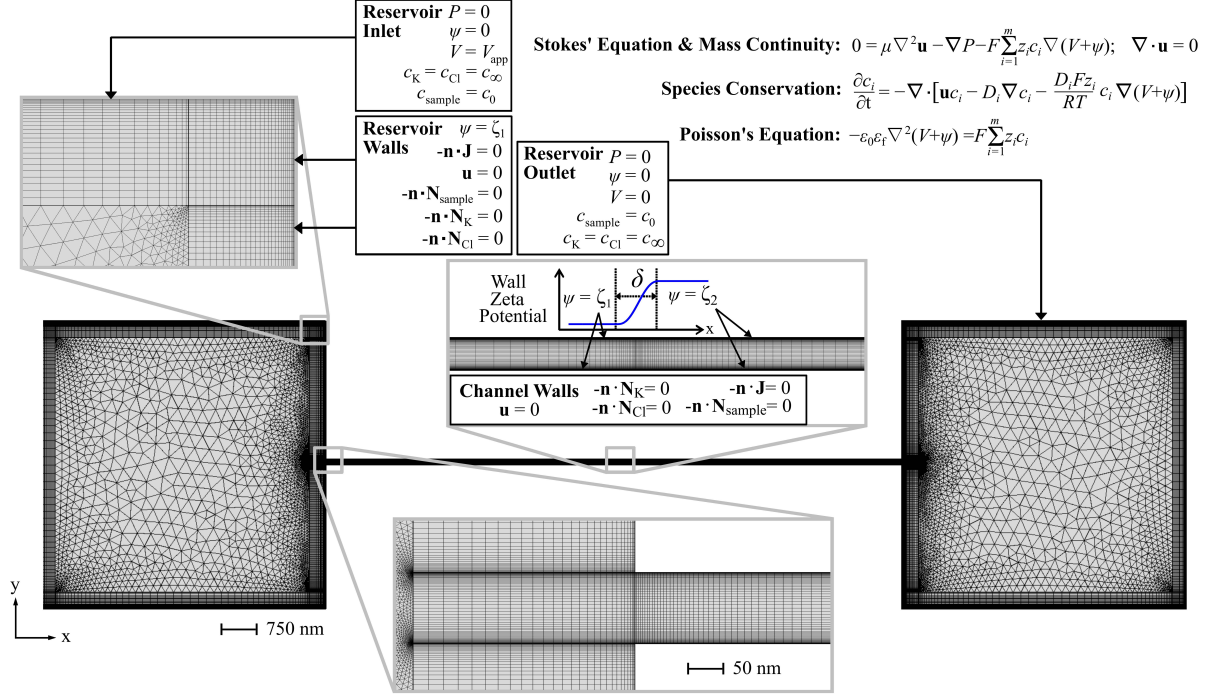


**Figure 2.3:** COMSOL mesh and boundary conditions for the 2D numerical model.

In order to verify that our 2D numerical simulations yield reasonable results for the BGE conditions, we compare the results to a simplified 1D area-averaged model which captures most, but not all, of the important physics (see supplemental material<sup>34</sup>). The most significant shortcoming of this 1D model is that it neglects diffusion and concentration polarization effects arising from the application of an external field across a permselective nanochannel with overlapped EDLs. However, Mani *et al.*<sup>14</sup> showed that these CP effects are negligible when the accumulation and depletion regions near a nanochannel inlet and outlet do not extend beyond a diffuse region near the interface (referred to as nonpropagating CP) and the Peclet number  $Pe = UL/D$  is sufficiently large. We therefore restrict the use of our 1D

verification model to (1) non-overlapped EDL cases and (2) high  $Pe$  overlapped EDL cases without appreciable CP propagation. Including these effects would make a simple 1D model intractable, so we instead use the 1D area-averaged model to verify our numerical simulations for these simpler limiting cases and then investigate more complex conditions using the 2D numerical results.

#### 4. Simplified 1D Area-Averaged Model

To ignore axial diffusion and CP effects, we assume that the system consists of two long, uniform channels in series, where the flow fields and ion distributions far away from the CP interface(s) are uniform in the axial direction. The underlying transport conditions in each of the two channels are different, however, and conservation laws couple the two channel sections together. Based on prior analysis, we are justified in assuming that ions are at equilibrium in the transverse direction, and the distribution is determined only by the local transverse potential  $\psi$ .<sup>4,16</sup> Using Boltzmann statistics, the ion distribution of a charged species  $i$  near a charged surface is thus approximated as

$$c_i = c_{i,\infty} \exp\left(-\frac{Fz_i\psi_c}{RT}\right) \exp\left[-\frac{Fz_i(\psi - \psi_c)}{RT}\right], \quad (2.4)$$

where  $\psi_c$  is the EDL potential at the channel centerline. For low concentration electrolytes ( $c_\infty < 10$  mM) in nanofluidic channels, the electric double layers can become overlapped, leading to a nonzero  $\psi_c$  and centerline ion concentrations which subsequently deviate from the bulk solution concentration.<sup>37,38</sup> Assuming a 1D transverse potential distribution, Poisson's equation becomes

$$\frac{d^2\psi}{dy^2} = \frac{-F}{\varepsilon_0\varepsilon_f} \sum_{i=1}^m z_i c_{i,\infty} \left\{ \exp\left(-\frac{Fz_i\psi_c}{RT}\right) \exp\left[-\frac{Fz_i(\psi - \psi_c)}{RT}\right] \right\}. \quad (2.5)$$

Baldessari and Santiago<sup>39</sup> showed that this equation can be made non-dimensional, integrated with a symmetry condition  $\frac{d\psi}{dy} = 0$  applied at some midplane location, and then integrated again with a zeta potential condition at the wall to obtain the full transverse potential distribution. It should be noted here that for channels with modified zeta potentials in any region(s) of the channel, the “bulk” concentration  $c_\infty$  in this region will not necessarily be equal to the supplying inlet reservoir concentration and must instead be solved as an additional unknown using channel-to-well equilibrium via a species conservation equation (see the next section), as in previous works by Mani *et al.*<sup>14</sup> and Sustarich *et al.*<sup>10</sup>

When the channel is long and thin, we can assume a fully developed laminar flow in each of the channel sections. Axial variations in the EDL potential  $\psi$  are also negligible far from the inlet, outlet, and zeta potential transition when CP effects are negligible, such that the axial electric field component is purely due to the applied potential across the channel.<sup>15</sup> Solving for the fully-developed 1D streamwise velocity profile  $u(y)$  far from these CP locations for a flat, rectangular channel of height  $H$  by substituting the charge density from Poisson’s equation into Stokes’ equation yields

$$u(y) = \frac{1}{2\eta} \frac{dP}{dx} (y^2 - Hy) - \frac{\varepsilon_0\varepsilon_f E_x \zeta}{\eta} \left( 1 - \frac{\psi(y)}{\zeta} \right). \quad (2.6)$$

Using flow continuity, we equate the height-averaged mean flow in regions of different zeta potential in order to relate the internal pressure gradients to the area-averaged EDL potential and electric fields in the respective regions.<sup>22</sup> By assuming atmospheric pressure at the channel inlet and outlet, we obtain the following equation for the pressure gradients in a

configuration with zeta potential  $\zeta_1$  in the first half and zeta potential  $\zeta_2$  in the second half of the channel

$$\left(\frac{dP}{dx}\right)_{1,2} = \mp \frac{6\varepsilon_0\varepsilon_f}{H^2} \left[ E_1\zeta_1 \left(1 - \frac{\bar{\psi}_1}{\zeta_1}\right) - E_2\zeta_2 \left(1 - \frac{\bar{\psi}_2}{\zeta_2}\right) \right], \quad (2.7)$$

where  $\bar{\psi}_1$  and  $\bar{\psi}_2$  are the height-averaged EDL potentials in regions 1 and 2, respectively. It is important to note that the electric fields in regions 1 and 2 are also different due to the dissimilar EDLs and corresponding ion distributions in the respective regions. These distributions can have significantly different numbers of charge carrying ions, thus the electrical conductivity and electric fields may vary considerably from one region to the next. We model the drop in the externally applied potential across the two regions as that due to series resistances, such that  $\Delta V_1 + \Delta V_2 = V_{\text{app}}$ . Assuming a linear potential drop in each region, we can divide by the product  $L_1L_2$  and use the definition  $E = \Delta V / L$  to relate the axial electric field in the two different regions to the applied potential  $V_{\text{app}}$ ,

$$\frac{1}{L_2}E_1 + \frac{1}{L_1}E_2 = \frac{V_{\text{app}}}{L_1L_2} \quad (2.8)$$

Since the electric fields in both regions are unknown, further analysis is required to close the system of equations. Under high Peclet number conditions, the effect of diffusion is confined near the channel inlet, outlet, and the location(s) of any changes in zeta potential. For cases with negligible CP, we emulate the approach of Sustarich *et al.*<sup>10</sup> by ignoring the diffusion term in the species conservation equation and solving for 1D area-averaged flow conditions far from these locations. The steady state conservation equation for the background electrolyte ions can be integrated over the height of the channel to obtain

$$\int_0^H [u(y)c_i(y) + b_i c_i(y)E_x] dy = \overline{uc}_i + b_i \overline{c}_i E_x = \text{const.}, \quad (2.9)$$

where  $b_i = \mu_i z_i F$ . This equation requires that the average net flux of species  $i$  due to convection and electromigration remains constant far from the zeta potential transition in each region at steady state. Equations (2.5)-(2.9) form a closed set of equations describing the theoretical framework required to approximate the 1D transverse electrostatic potential, ionic species transport, velocity profile, and axial electric field in the nanochannel from a simplified area-averaged model for cases of negligible CP. These equations are first solved simultaneously for the unknown electric fields and the unknown “bulk” concentration  $c_\infty$  of ions in the downstream, modified region. The resulting potential and BGE ion profiles are then found from the method described in the previous section, and the velocity profiles are calculated from equation (2.6). Note that equations (2.5)-(2.7) are only valid for regions with transverse potential distributions that are symmetric about the centerline (i.e. where the top and bottom walls have the same surface charge and zeta potential).

To provide an additional measure of comparison between the numerical model and analytical theory, we estimate the 1D centerline BGE concentration for non-overlapped EDLs through a balance of local species drift and diffusion in the two electroneutral regions

$$u_{ion,1}c_1 - D_i \frac{dc_1}{dx} = u_{ion,2}c_2 - D_i \frac{dc_2}{dx} = \text{const.}, \quad (2.10)$$

where  $u_{ion,1}$  and  $u_{ion,2}$  are the ion transport velocities due to the combined effects of advection and electromigration in regions 1 and 2, respectively, and  $c_1$  and  $c_2$  are the local centerline BGE concentrations in regions 1 and 2, respectively. Integrating these equations and applying the constraints that {1} the concentrations far away from the interface decay to bulk values  $c_{\infty,1}$  and  $c_{\infty,2}$ , and {2} the concentration at the interface is the same in both regions, we obtain the following equations describing the jump in concentration from one region to the next

$$c_1(x) = c_{\infty,1} + (c_{\infty,2} - c_{\infty,1}) \exp(\text{Pe}_x) \quad \text{for } -L_1 \leq x \leq 0, \quad (2.11)$$

$$c_2(x) = c_{\infty,2} - (c_{\infty,2} - c_{\infty,1}) \exp(\text{Pe}_x - \text{Pe}_{L_1}) \quad \text{for } 0 < x \leq L_2, \quad (2.12)$$

where  $\text{Pe}_x = u_{ion} x / D$  and  $\text{Pe}_{L_1} = u_{ion} L_1 / D$ . The ion drift velocity is a combination of the bulk flow and electrophoretic transport,  $u_{ion,i} = u_{EOF} + b_i E_x$ .

## D. Results

### 1. Verification Simulations

We first verify our numerical model by comparing 2D simulation results to the 1D model for the case of finite, non-overlapping EDLs (see Figure 2.4). The nonuniform ion distributions and the resulting electric fields for this particular non-overlapping EDL case do not cause appreciable sample accumulation in the channel because the difference in zeta potentials is insufficient to induce the large changes in bulk concentration (and therefore the electrical conductivity) required for significant FASS-like enhancement.<sup>10</sup> We therefore neglect the sample analyte conservation equations for these particular simulations, and simply confirm that the resulting background electrolyte ion, potential, and velocity profiles in our numerical simulations reasonably match those predicted by the 1D model.

The verification simulation geometry is a 0.5 mm long, 100 nm tall straight nanochannel filled with a solution of 15 mM KCl, corresponding to a Debye length of about  $\lambda_D \approx 2.5$  nm. A voltage of 5 V is externally applied to drive the resulting EOF with a nominal electric field strength of 10 kV/m. The unmodified and modified zeta potentials of the channel walls are fixed at -30 mV and -6 mV, respectively. Using the theory of Hughes *et al*, we find that a solution of 15 mM KCl at pH = 6.2 would yield an unmodified wall zeta potential of about -30 mV for silica, and a corresponding gate voltage of 10 V would generate a zeta potential of

approximately -6 mV in the right half of the channel<sup>138</sup> for an insulating silica layer thickness of 30 nm.

Figure 2.4 shows good agreement between our numerical simulation and the 1D area-averaged model for the EDL potential, BGE salt concentration, and velocity profiles. The transverse potential in Figure 2.4(a) decays to zero for the non-overlapping EDL case, maintaining electroneutrality along the channel centerline for these conditions. The nonuniform zeta potential distribution leads to internally generated pressure gradients in both regions because the average electroosmotic flow component of the velocity from equation (2.6) is different in the two regions of differing zeta potential. Since the average electroosmotic velocity is higher in region 1, the velocity profile in this region must contain an adverse pressure driven flow component to maintain mass conservation. Under the assumption of atmospheric pressure at the channel inlet and outlet, the pressure gradient in region 2 is equal and opposite of that in region 1 by flow continuity for our chosen geometry. These internal pressure gradients lead to a velocity profile which is maximum along the center in region 2 and has a local minimum at the center in region 1, as shown in Figure 2.4(c).

In order to satisfy background ionic species conservation, the height-averaged fluxes from equation (2.9) must be equal in the two regions. This constraint leads to the nonuniform ion profiles in Figure 2.4(b) and Figure 2.4(d), in which the bulk centerline concentration must change locally to balance the overall average fluxes as the flow conditions change from region 1 to region 2. To understand why this occurs, we consider the cationic fluxes in each region. The average convective flux from equation (2.9) depends on the integrated product of the velocity and ion concentration, hence the shape of each profile relative to the other plays a large role in determining the magnitude of the average flux. We know that the adverse pressure gradient in region 1 leads to decreased flow along the channel centerline and

increased flow near the walls, where the counter-ions are abundant within the EDL. Thus, the average convective flux is relatively large because the maximum velocity and maximum concentration occur near the same location. Conversely, the favorable pressure gradient in region 2 increases the flow along the centerline and hinders flow near the walls, so the average convective flux of cations would naturally be lower for the same concentration profile because the flow speed is largest where the concentration is minimum. As a result, the average concentration in region 2 must increase to maintain a total flux balance between the two regions. Figure 2.4 shows that the region 2 bulk BGE concentration increases by about a factor of 1.4 to account for this imbalance.

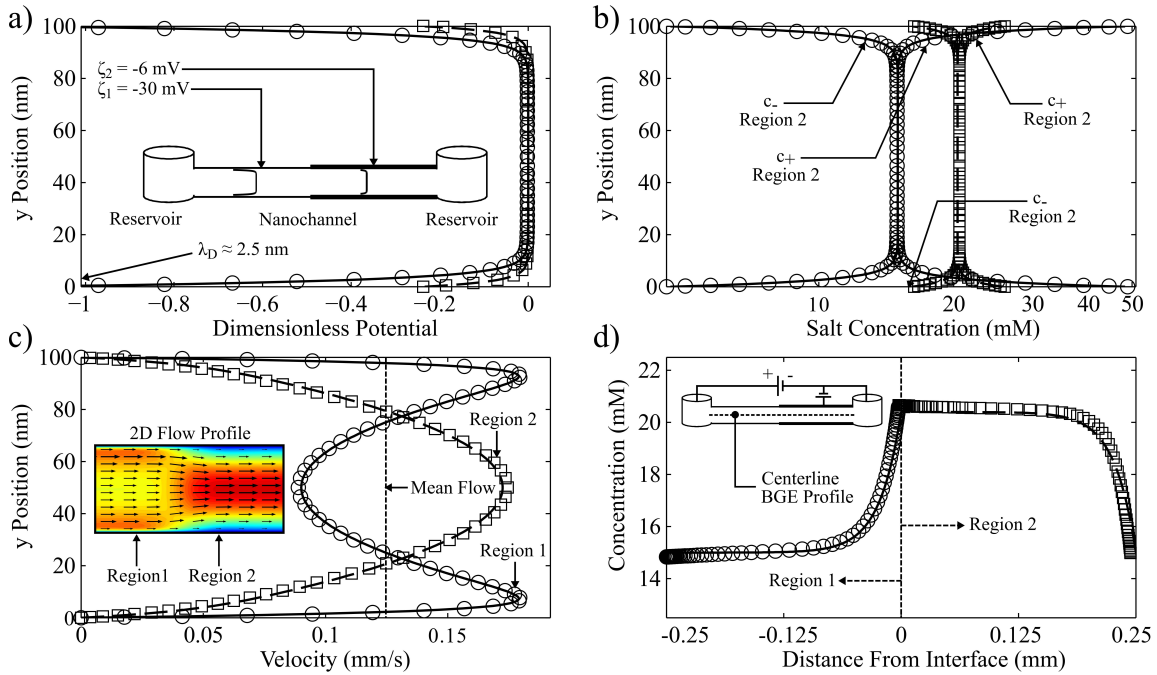


**Figure 2.4:** Comparison of 1D area-averaged (solid and dashed lines) vs. simulation results (open circles and squares) for thin EDLs. The profiles show excellent agreement in both region 1 (solid lines, open circles) and region 2 (dashed lines, open squares).

Figure 2.5 shows a comparison of various simulated profiles with the 1D area-averaged model as we varied the zeta potential  $\zeta_2$  in the right half of a channel filled with 0.01 mM

KCl. This low density of screening BGE ions leads to noticeably overlapped EDLs, as the Debye length of approximately 97 nm is on the same order as the height of the 100 nm tall channel. The zeta potential in region 1 is fixed at -100 mV, roughly corresponding to a solution of pH = 6.15, and the nominal electric field strength is 10 kV/m. The estimated gate voltages required to produce the  $\zeta_2$  values in Figure 2.5 range from approximately 0 to 8.8 V. Significant propagation of CP beyond the channel inlet/outlet was not observed in these simulations; this fact coupled with a Peclet number of  $\sim 100$  suggests that it is safe to compare these numerical results to the 1D area-averaged model<sup>14</sup> without expecting significant errors.

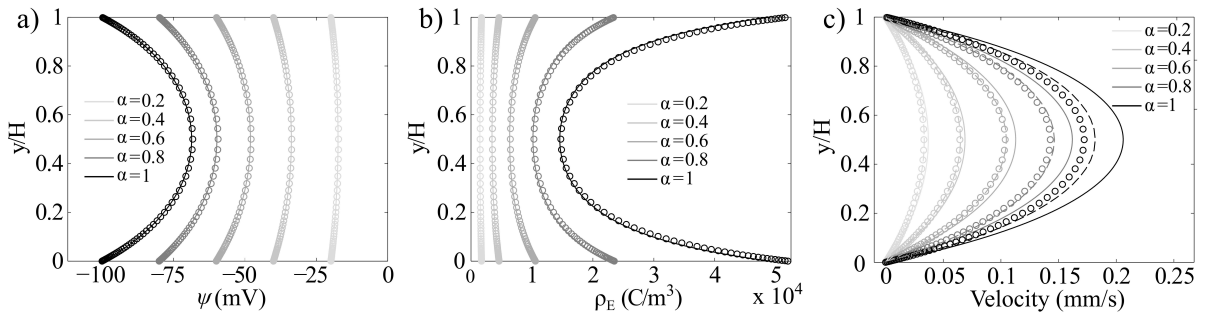


**Figure 2.5:** Simulation vs analytical results for thick EDLs in a 100 nm tall channel filled with 0.01 mM KCl solution. Here, the zeta potential ratio  $\alpha = \zeta_2 / \zeta_1$  is varied as  $\zeta_1$  is fixed at -100 mV. Analytical (solid lines) vs. simulation (open circles) results are shown for (a) the potential, (b) the charge density, and (c) the velocity profiles as  $\zeta_2$  is modified. Velocity profiles are also included in (c) for a 1D model which does not assume zero pressure differential across the channel, but instead uses the simulated pressure drop as a correction factor to the theoretical profile (dashed lines).

The results in Figure 2.5 show good agreement with the 1D area-averaged model for the potential and charge density profiles far from the zeta potential transitions, even though the velocity profiles appear to deviate for the more uniform cases in which the value of  $\alpha = \zeta_2 / \zeta_1$  approaches unity. This discrepancy is primarily due to the fact that the 1D model assumes atmospheric pressure at the channel inlet and outlet to obtain equation (2.7), an assumption which leads to zero pressure difference across the channel. In contrast, the

numerical simulation fully encompasses the effect of the fluid reservoirs; accounting for this more realistic fluid motion in the reservoirs leads to a small adverse pressure differential across the channel which slows the fluid slightly. It should be noted here that since the height-averaged potentials  $\bar{\psi}_{1,2}$  approach the zeta potentials  $\zeta_{1,2}$  as the EDL thickness increases, equation (2.7) shows that the internal pressure gradients are significantly reduced when the EDLs are overlapped. For overlapped EDL cases with values of  $\alpha$  closer to unity, internal pressure gradients due to the imposed heterogeneities are further reduced and the velocity profile is subsequently more sensitive to errors in the pressure gradient calculations introduced by the assumption of a nonzero pressure differential across the channel. Included in Figure 2.5(c) are velocity profile results in which the numerically solved pressure drop across the channel is used to correct the 1D area-averaged model. This correction improves agreement between the 1D model and numerically simulated profiles, confirming that the adverse pressure differential between the reservoirs introduces a small but non-negligible error in the velocity field for some cases.

## 2. Possible Enhancement Mechanisms

For the current nanochannel configuration in which an embedded electrode controls the zeta potential in the right half of the channel, there are three possible mechanisms which can contribute to sample accumulation inside the channel itself: stacking, focusing, and focusing at a mid-channel CP interface. Both cationic and anionic preconcentration can also be achieved at or near the channel inlet/outlet via stacking and/or focusing by leveraging CP effects at stationary or propagating “shocks” of ion accumulation and depletion at different interfaces within the reservoirs; Zangle *et al.*<sup>15</sup> comprehensively reviewed the various

experimentally observed and theoretically predicted stacking and focusing mechanisms at these locations, so we direct our focus to investigating stacking and focusing within the domain of a nanochannel with nonuniform zeta potential.

Mani *et al.*<sup>14</sup> described a useful characteristic analysis which utilizes a dimensionless mobility defined as the ratio of the migration speed of species  $i$  to the bulk electroosmotic velocity,  $v_i^* = \frac{U_i^{\text{eph}}}{U^{\text{bulk}}}$ , in order to predict the direction of analyte information propagation in

different regions of the system (and therefore whether stacking or focusing occurs) through simple scaling arguments. We adopt this approach by scaling the analytical EOF profile for

region 2 of a nonuniform channel to obtain  $v_{2,i}^* = -\frac{v_i |z_i| F \eta E_2}{\epsilon_0 \epsilon_f (3E_1 \zeta_1 - 4E_2 \zeta_2)}$ . Note that our definition

differs from the conventional definition  $v_i^* = \frac{v_i z_i F \eta}{\epsilon_0 \epsilon_f \zeta}$  of Mani *et al.*,<sup>14</sup> but reduces to the same

result for the limiting case of  $E_1 = E_2$  and  $\zeta_1 = \zeta_2$ . This distinction arises because our nonuniform channel leads to different induced pressure gradients and electric fields in the two regions, such that the dimensionless mobility varies within the channel. The bulk flow velocity must have the same scale in both regions by continuity, so similarly for region 1 we have

$$v_{1,i}^* = -\frac{v_i |z_i| F \eta E_1}{\epsilon_0 \epsilon_f (3E_1 \zeta_1 - 4E_2 \zeta_2)}.$$

For an anionic species, a dimensionless mobility  $v_{2,i}^* > 1$  describes an analyte for which the upstream electrophoretic velocity in region 2 exceeds the downstream bulk flow speed, leading to net upstream analyte transport in that region. Conversely, a dimensionless mobility of  $v_{2,i}^* < 1$  predicts that the same analyte will travel downstream in region 2 because the bulk flow speed exceeds the electrophoretic velocity. In such a case, the anionic sample will not be able to enter the channel from the outlet reservoir and thus no preconcentration is possible

inside the channel.<sup>15,16</sup> The electric field in each region can be roughly estimated to calculate the dimensionless mobility by approximating the EDLs as thin<sup>10,14</sup> to obtain  $E_2 / E_1 \sim \sigma_1 / \sigma_2$ , and then by using the Grahame equation to obtain  $E_2 / E_1 \sim \sinh\left(\frac{Fz\zeta_1}{RT}\right) / \sinh\left(\frac{Fz\zeta_2}{RT}\right)$ .<sup>41</sup>

The first possible enhancement mechanism within the nanochannel, stacking, occurs when the background flow conditions predict average anionic sample velocities in each region which are not equal but are still in the same direction, i.e. when  $v_{2,i}^* > v_{1,i}^* > 1$ . This transport velocity difference effectively leads to a “traffic jam” of ions because sample ions are predicted to move upstream faster in region 2 than in region 1. This is the effect observed in Figure 2.6(a) in which the ion concentration in one of the two regions must increase in order to balance the flux of ions moving through each region at steady state. This is also the same underlying mechanism found in classical field-amplified sample stacking, as described by Burgi and Chien.<sup>8</sup> In the current configuration, however, FASS-like stacking can be achieved in a stationary manner without the need for a propagating injected plug solution. Note that this type of mid-channel stacking would be achieved using higher concentration BGE solutions in which the EDLs do not overlap, and is therefore not a direct consequence of CP. For overlapped EDLs, concentration polarization effects would manifest and the third mechanism would dominate the predicted enhancement.

The second mechanism, focusing under non-overlapped EDL conditions, occurs when the transport velocity of an anionic species is upstream in region 2 but downstream in region 1, i.e. when  $v_{2,i}^* > 1 > v_{1,i}^* > 0$ . In such situations, the sample is predicted to be driven from both sides to a single location of maximum accumulation near the zeta potential transition, as shown in Figure 2.6(b). This type of focusing occurs in our channel when the electrophoretic velocity exceeds the bulk flow speed in region 2 but not in region 1, a condition which can be

satisfied by specific combinations of zeta potentials, electric fields, and velocity profiles in each region. Whether stacking or focusing occurs in the channel depends on the dimensionless mobility, and is therefore highly dependent on sample mobility and valence. In general, samples of lower mobility will tend to become focused because the decreased mobility lowers  $v_{1,i}^*$  sufficiently that the opposing convection can exceed electromigration and change the direction of the analyte transport in region 1. This mechanism was discussed at length by Sustarich *et al.*,<sup>10</sup> who showed that finite but non-overlapping EDLs can enhance the level of observed focusing.

The third possible mechanism is also considered focusing but occurs only for thick EDL cases. This effect arises from the axial potential gradient between regions of different area-averaged EDL potential, and has previously proven to be useful in concentrating charged samples at microchannel/nanochannel interfaces.<sup>13-16</sup> This effect differs from the focusing described above in that the dimensionless mobility in region 1 does not necessarily have to drop below unity. Rather, in this case there exists a small diffusion-limited transition region at the CP interface in which the dimensionless mobility actually changes sign across the interface because the coupling between the area averaged EDL potential gradient and the applied electric field can effectively reverse the net electric field direction in this location (see Sec. IIIB for further explanation). A dimensionless mobility greater than unity in both region 1 and region 2 would subsequently lead to a strongly polarized interface with depletion on the left side and accumulation on the right side (see Figure 2.6). Since the first two mechanisms have been thoroughly investigated by Bharadwaj *et al.*<sup>9</sup> and Sustarich *et al.*,<sup>10</sup> respectively, we chose to limit the scope of the current study to investigating a regime of overlapped EDLs with nonuniform zeta potentials in which the third mechanism is the principal cause of analyte accumulation.

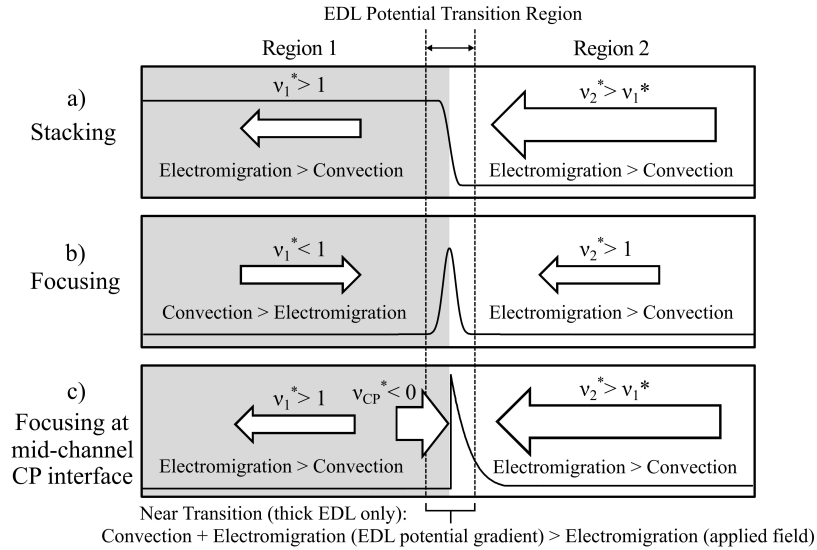


**Figure 2.6:** Diagram of the three possible enhancement mechanisms: stacking, focusing, and focusing at a mid-channel CP interface. Arrows show the direction and relative magnitude of the net sample ion transport velocity in each region before steady state is reached.

The enhancement from sample stacking can easily be estimated by the ratio of predicted sample fluxes in each region,<sup>8,15</sup> while the non-overlapped EDL focusing mechanism requires some incorporation of diffusion in order to properly model. Focusing capabilities for such conditions are still largely determined by the ion fluxes in the fully developed areas far from the zeta potential transition, however, and analytical theory can still be used to estimate the level of sample enhancement from this type of focusing by including axial diffusion.<sup>10</sup> In contrast, the third mechanism is dominated by a very localized CP effect near the transition and thus cannot be quantitatively predicted using a simple 1D model; a more complete numerical treatment is required when the nonuniform EDLs are overlapped in order to fully capture all of the driving forces which contribute to this type of CP-based focusing within the channel.

### 3. Analyte Focusing Using Nonuniform, Overlapped EDLs: 2D Simulation Results

We demonstrate how an anionic sample analyte with valence  $z = -2$  and diffusivity  $D_s = 0.5 \times 10^{-9} \text{ m}^2\text{s}^{-1}$  accumulates near an interface where a smooth step change in zeta potential occurs (see Figure 2.7). Specifically, Figure 2.7(a) depicts the temporal evolution of a 2D sample concentration profile within a  $20 \text{ }\mu\text{m}$  long,  $100 \text{ nm}$  tall channel. We fixed the sample concentration at  $1 \text{ pM}$  at the top of the BGE inlet and outlet reservoirs for these simulations, such that the sample ions migrate left through the channel under the influence of the applied field. The unmodified zeta potential was fixed at  $-100 \text{ mV}$ , while the modified zeta potential was  $-40 \text{ mV}$  and the nominal electric field strength was  $10 \text{ kV/m}$ .

The intrinsic EDL potential  $\psi$  along the centerline remains nonzero throughout the channel due to the overlapped EDLs, leading to an axial gradient in the area-averaged EDL potential near the zeta potential transition. Since the axial electric field  $E_x = -\left(\frac{\partial V}{\partial x} + \frac{\partial \psi}{\partial x}\right)$  is a coupled combination of the applied electric field and the axial EDL potential gradient, its direction can change sign locally at certain locations depending on the sign and magnitude of  $\frac{\partial \psi}{\partial x}$  relative to  $\frac{\partial V}{\partial x}$ . Figure 2.7(a) shows how this gradient in the net electric field enhances sample accumulation in the middle of the channel by effectively creating an electrophoretic trapping region at this CP interface. The presence of a similar electrostatic potential gradient at the channel outlet suggests that an anionic analyte will not be able to enter the channel unless diffusion and electromigration from the applied field can drive ions past this interface. The magnitude of the zeta potential  $\zeta_2$  near the outlet is therefore critical in determining whether sample ions are able to enter the channel, as suggested by the form of the dimensionless mobility  $\nu_{2,i}^*$ . By controlling  $\zeta_2$  with embedded electrodes in the top and

bottom walls, this area-averaged potential gradient can be lowered sufficiently that the combined effect of diffusion and electromigration from an external electric field overcomes the CP at the channel outlet, allowing for sample transport into the channel.

A simple analysis suggests that net the electric field should locally change direction at a CP interface when the local EDL potential gradient exceeds the local electric field from the applied potential, or  $\frac{\partial\psi}{\partial x} > \left| \frac{\partial V}{\partial x} \right|$ . By estimating this EDL potential gradient as the change in zeta potential over some transition length scale assumed to be on the order of the Debye screening length, it is predicted that an approximate difference in zeta potentials exceeding just 1 mV leads to  $\frac{|\zeta_2 - \zeta_1|}{\lambda_D} > \frac{V_{\text{app}}}{L}$ , and thus  $E_x < 0$ , for a 10 kV/m applied field in a 0.01 mM KCl solution ( $\lambda_D \approx 100$  nm). Our simulation results in Figure 2.7(b) show that this local electric field reversal indeed occurs when  $\zeta_1$  and  $\zeta_2$  differ by more than about 0.6 mV.

Although this effect occurs for very small variations in  $\alpha = \frac{\zeta_2}{\zeta_1}$ , we do not see appreciable focusing of ions within the channel when  $\zeta_2$  is sufficiently negative, such as in the  $\alpha = 0.8$  case in Figure 2.7(d), because CP at the outlet almost entirely excludes all sample ions from entering the channel.

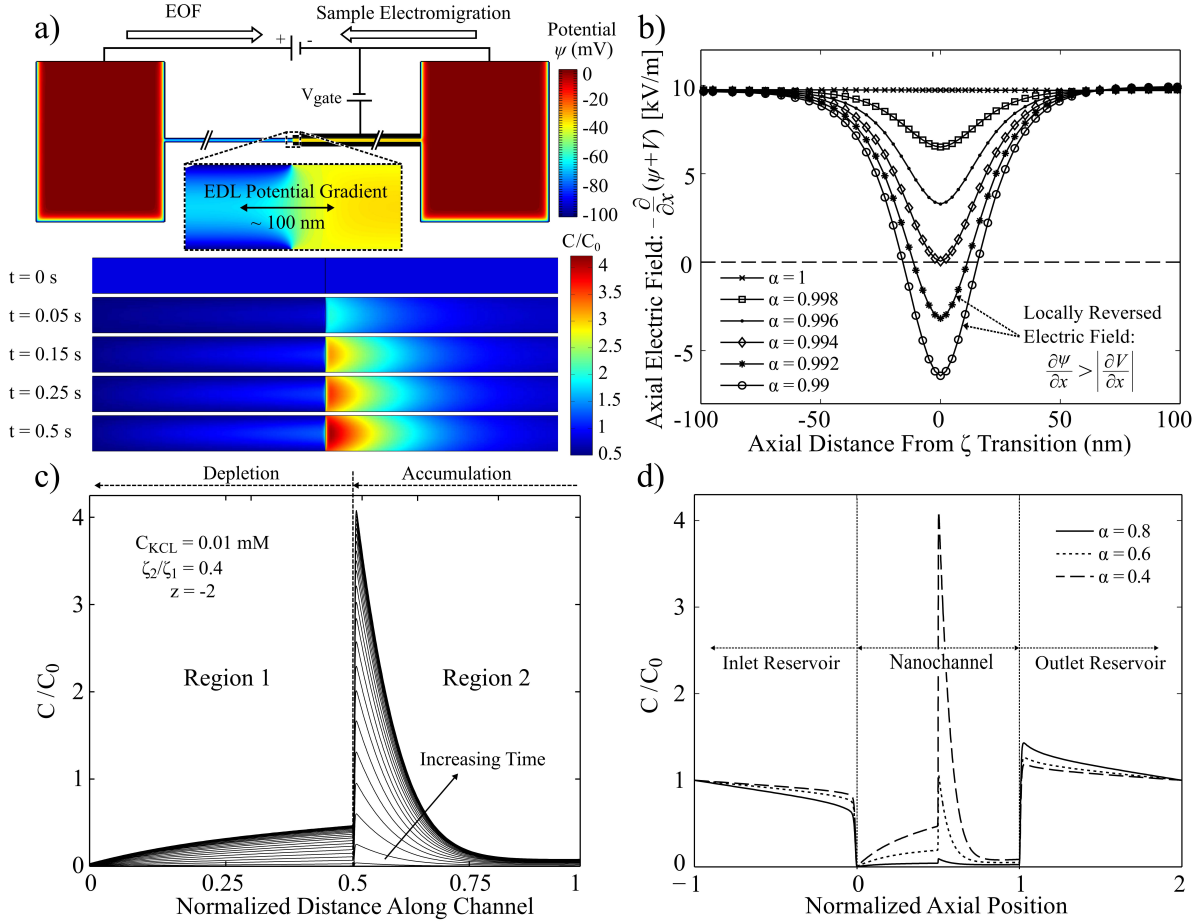


**Figure 2.7:** (a) EDL potential near the mid-channel CP interface along with the transient evolution of a 2D sample concentration profile in the channel, (b) the net electric field along the centerline near the mid-channel CP interface, (c) the temporal sample profile along the channel center, and (d) the steady state sample concentration along the centerline for varying  $\alpha$ . The axial EDL potential gradient is visible in (a), and its effect on the sample motion is evident from the reversal of the net electric field in (b) as well as the CP-induced analyte focusing in (c) and (d). The zeta potential ratio and BGE concentration for these simulations of a 20  $\mu\text{m}$  long, 100 nm tall channel were fixed at  $\alpha = 0.4$  and  $C_{KCl} = 0.01$  mM, respectively, unless otherwise specified.

To understand the temporal distribution of sample ions throughout the channel in Figures 2.7(a) and 2.7(c), we further examine the role of the net electric field and corresponding sample fluxes. The electric field in region 2 is higher than that in region 1 due to the lower density of BGE ions (fewer ions are needed to screen the smaller zeta potential), and thus any sample ions that are able to enter the channel are driven towards region 1 with a large electrophoretic velocity. Sample ions near the region 2/region 1 transition are slowed when

approaching the EDL potential gradient at the CP interface, which is large enough to reverse the direction of the net electric field in this case. In this diffusion-limited transition zone, the electrophoretic flux and convective flux are both positive (to the right) and only the diffusive flux is negative (to the left). The diffusive flux is initially relatively small, so the overall imbalance of fluxes causes the sample to rapidly become focused near the location where the net electric field changes direction. After the sample sufficiently accumulates, the concentration gradient which controls the diffusive flux becomes large enough to drive sample ions past this stationary CP “shock” and into region 1. Once the sample enters region 1, electromigration and a strong diffusive flux drive the ions further upstream into the BGE inlet reservoir, easily overcoming the opposing convective flux and leading to further localized sample depletion as ions are rapidly accelerated out of the channel. Eventually the diffusive, electromigrative, and convective fluxes start to balance and the system approaches equilibrium. The spatiotemporal centerline sample concentration converges to a constant profile as the system reaches steady state, as shown in Figure 2.7(c).

#### 4. Maximum Enhancement and Limiting Behavior

The maximum achievable sample concentration enhancement for overlapped EDL conditions is governed by CP phenomena, and is therefore primarily a function of EDL thickness, zeta potential ratio, sample charge and mobility, and the applied electric field. Figure 2.8 shows thick EDL sample focusing within a 50 nm tall channel, demonstrating the maximum concentration enhancement achievable as these control parameters are varied. Significant accumulation occurs near the zeta potential transition for our simulated conditions only when the nonuniformities in potential and ion distributions throughout the channel are noticeable; that is, when the zeta potential magnitudes in region 1 and 2 differ sufficiently and

the electric double layers overlap to create a mid-channel CP interface. A moderate level of stacking or focusing can potentially be observed in the regime of non-overlapped EDLs for certain sample mobilities and BGE conditions, but our results in Figure 2.8(a) indicate that the simulated sample with a mobility of  $3.9 \times 10^{-8} \text{ m}^2\text{V}^{-1}\text{s}^{-1}$  (roughly representative of fluorescein) is not predicted to appreciably accumulate anywhere in the channel when the EDLs are not overlapped.

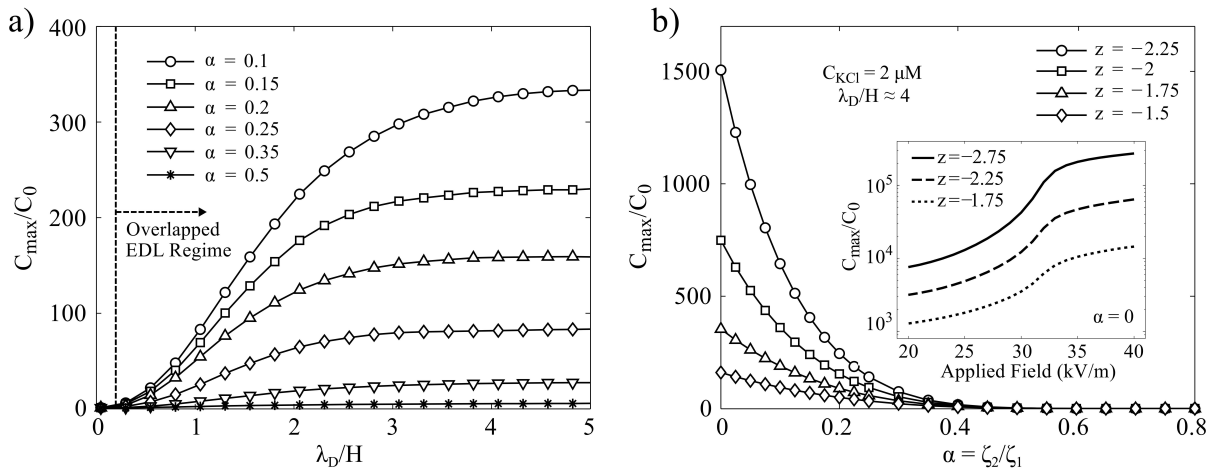


**Figure 2.8:** Sample enhancement is shown in (a) for varying zeta potential ratios and EDL thicknesses for a fixed 50 nm channel height and 10 kV/m applied field, and in (b) for varying zeta potential, sample charge, and applied field. The zeta potential in region 1 was fixed at -100 mV for these simulations, while the sample valence for (a) was fixed at  $z = -2$ . The corresponding KCl concentrations in (a) range from 50 mM to 1.5  $\mu\text{M}$ . The inset plot in (b) shows maximum concentration enhancement for  $\alpha = 0$  as the applied electric field is increased to 40 kV/m.

More interesting effects manifest as we explore sample enhancement in the limit of thick electric double layers. Figure 2.8(a) demonstrates that the level of sample enhancement increases as the EDLs become much thicker relative to the channel height and the magnitude of  $\zeta_2$  decreases, i.e. as the mid-channel CP interface becomes more prominent and the CP interface at the outlet starts to disappear. Figure 2.8(b) shows that the extent of CP at the outlet is limited enough to allow a large number of sample ions to enter the channel and

accumulate near the zeta potential transition only when  $\alpha < 0.5$  for these conditions. Specifically, the results show that the sample is locally enhanced by greater than an order of magnitude in the middle of the channel when  $\alpha$  drops below approximately 0.45 for  $\lambda_D / H \approx 4$  if  $\zeta_1$  is fixed at -100 mV.

As the concentration is decreased below 1 mM, the enhancement in Figure 2.8(a) first increases dramatically and then starts to saturate as the system reaches a state in which there are such few ions to screen the charged walls that the potential and ion distributions are essentially the same at the centerline as they are at the wall. This limiting behavior leads to an area-averaged EDL potential gradient that approaches a constant value as the concentration is decreased beyond a critical threshold for a given channel height and fixed zeta potentials. As this potential gradient governs the CP which leads to sample focusing, the enhancement ultimately reaches a plateau for very low BGE concentrations if all other simulation parameters are held fixed. Figure 2.8(b) shows that because highly charged sample ions experience stronger interactions with field gradients near the transition, ions of sufficiently high valence can effectively be concentrated by up to five orders of magnitude by increasing the applied electric field strength. The curves for  $z = -1.75$  are representative of fluorescein ions, and the predicted 6,200-fold enhancement of this sample at 32 kV/m roughly constitutes a factor of 45 increase compared to injection-based FASS results with the same sample and applied field.<sup>10</sup>

## 5. Simultaneous Focusing and Separation

Under the right conditions, such as those shown in Figure 2.9(a), CP effects can propagate away from the midchannel interface and establish extended electric field gradients in the channel downstream of the interface.<sup>14,15</sup> Note that this is slightly different than

conventional CP systems which utilize microchannel-nanochannel junctions as the CP interface; inside the nanochannel, the electric field can reach higher values because of the low nanochannel conductance relative to that of the adjoining microchannels in which the stacking or focusing locations are conventionally found. As with similar CP and counter-flow gradient focusing (CFGF) techniques,<sup>7,14-17,20</sup> the electric field gradient depicted in Figure 2.9(b) can be leveraged for focusing anions at the location where the dimensionless mobility changes sign; that is, where the electrophoretic velocity exceeds EOF downstream (to the right) of the location but EOF prevails upstream (to the left) of that location.<sup>14-16</sup> Our results suggest that concentration enhancements on the order of  $10^4$  are readily achievable with minimal tuning and optimization of the simulation conditions.

For analytes of different mobility, the maximum and minimum electrophoretic velocity will vary and thus the location where EOF and electrophoresis balance will change; for higher mobility analytes the focusing location will shift to the left, while for lower mobility analytes the focusing location will shift to the right (Figure 2.9(c)). This leads to the development of focusing locations which also serve to simultaneously separate the analytes into spatially distinct regions of high concentration/intensity. The curves shown in Figure 2.9(a) overlap considerably because of the short channel with a relatively low Peclet number ( $\sim 100$ ) that was simulated here; however, a longer channel would broaden the field gradient and lead to larger separation between peaks, which would be more practical for the purposes of individual analyte detection.

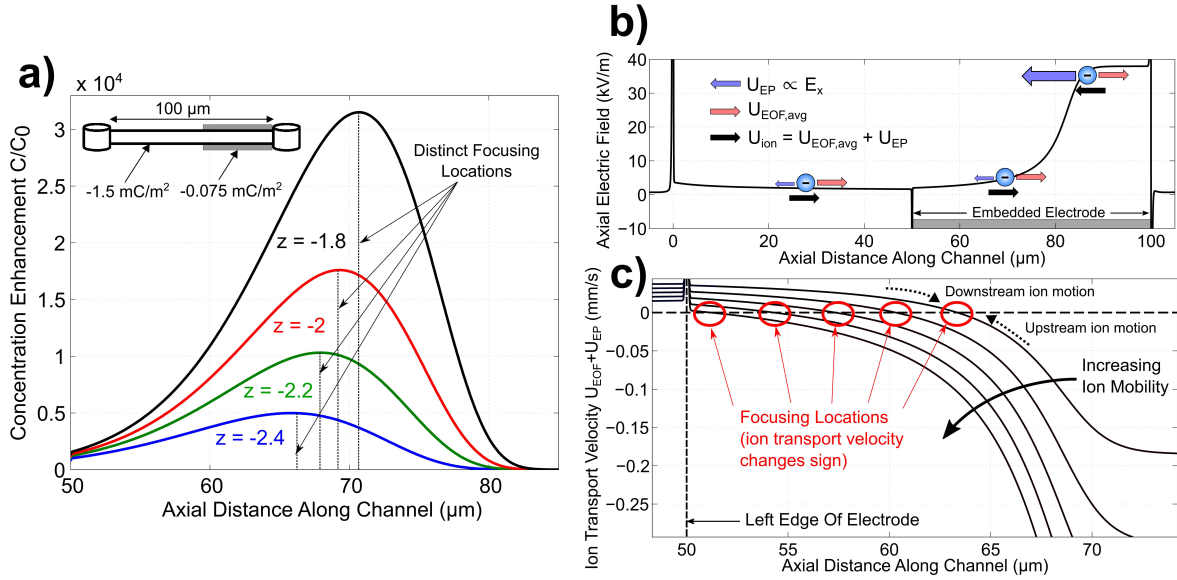


**Figure 2.9:** Simultaneous focusing and separation in region 2 of the nanochannel. CP effects establish an extended electric field gradient throughout this region, leading to significant variations in the local electrophoretic velocity along the channel. For analytes of different mobility the electrophoretic velocity balances the EOF velocity at different axial locations, raising the prospect of simultaneous focusing and separation for this configuration.

## 6. Assumptions and Limitations

As with any simulation, it is important to understand the assumptions and limitations of our numerical model. First, we note again that  $\zeta_1$  is fixed at  $-100 \text{ mV}$  for the idealized simulations which employ zeta potential boundary conditions, so practical variations in  $\zeta_2$  would only be achievable by modulating the gate voltage for a fixed solution pH. While the choice of the zeta potential transition length  $\delta = 5 \text{ nm}$  in our numerical model is somewhat arbitrary, our results show that the choice of  $\delta$  does not appreciably affect the results for a range of  $2 \text{ nm} < \delta < 200 \text{ nm}$  with a background concentration of  $C_{\text{KCl}} = 0.01 \text{ mM}$ . This can be explained through the observation that the centerline potential profile in the diffusion-limited transition region, and thus the axial EDL potential gradient, is relatively insensitive to  $\delta$  unless it is varied by several orders of magnitude and is well outside the predicted range of

values (see the supplemental material<sup>34</sup>); preliminary simulations of the 2D governing equations (2.1)-(2.3) with a discontinuous surface charge boundary condition indicate that the surface potential transition length ranges from approximately 2 nm to 150 nm depending on  $\alpha$ , while a previously published numerical simulation of embedded electrodes suggests that the transition is on the order of a few nanometers.<sup>3</sup> Therefore, we fixed the transition length at  $\delta = 5$  nm for the purposes of this study.

A background electrolyte concentration of less than 1  $\mu\text{M}$  is impractical to simulate in the limit of small  $\alpha$ , as the sample ions will begin to accumulate sufficiently that the maximum concentration would be within an order of magnitude of the BGE concentration. In such a case, the analyte would noticeably contribute to the charge density and corresponding EDL potential distributions near the mid-channel CP interface (recall that this contribution is neglected in the current model). However, practically achieving ionic concentrations below 1  $\mu\text{M}$  is difficult since ions in pure water are generally in the nM concentration range. Furthermore, these low concentration conditions would introduce complications in the experimental characterization and validation of the devices; the conductivity of electrolyte solutions approach that of water for sufficiently low BGE concentrations, and the small resulting current produced by ion transport in the channel at such low concentrations can exceed the limit of practical current sensing capabilities due to the inherently low electrical conductance of nanofluidic channels.<sup>35-39</sup>

The induced pressure gradients within nanochannels experiencing nonuniform EOF can also pose practical difficulties. In particular, electrokinetic systems with large nonuniform electric fields can lead to structural deformation, channel collapse, cavitation, and delamination of bonded wafers.<sup>42,43</sup> For the current configuration in which  $\zeta_1 < \zeta_2 < 0$ , the

higher magnitude of  $\zeta_1$  generally leads to a higher EOF component of the fluid flow in region 1, and by continuity an adverse pressure gradient must be generated in this region to balance the average sum of the pressure driven flow and electroosmotic flow components in both regions. Therefore, cavitation is unlikely to occur because the positive pressure gradient in region 1 leads to a positive gauge pressure in the middle of the channel. Moreover, the lowest pressure predicted by our simulations was on the order of  $-1 \times 10^{-2}$  bar, well below the critical pressure of -16 bar at which cavitation is theoretically predicted to occur.<sup>42</sup> Structural deformation or wafer debonding could potentially be an issue for more extreme conditions than those we investigate, but the maximum fluid pressure achieved in our simulations is slightly below 3 kPa, several orders of magnitude below the typical bond strength of standard microfabrication techniques.<sup>43</sup>

Finally, it should be noted that the current model neglects the presence of  $H^+$  and  $OH^-$  ions due to non-neutral solution pH and dissociation of surface silanol groups at the channel walls. Depending on the solution properties, these effects may also need to be taken into account when calculating the volumetric charge density. Consideration of  $H^+$  and  $OH^-$  ions in previous studies<sup>37,38</sup> suggests that there is a limited pH range over which the concentration of these ions significantly differs from the BGE ion concentrations and can subsequently be neglected. For solutions with sufficiently high or low pH, the relatively high concentration of  $OH^-$  or  $H^+$  ions, respectively, leads to additional charge screening effects which introduce error in the resulting potential and BGE profiles if neglected. By comparing the relative bulk ion concentrations in the reservoirs from electroneutrality conditions, we can expect an estimated error of more than 10% in the spatial charge density if we neglect  $H^+$  and  $OH^-$  ions in a KCl solution with a concentration below 1  $\mu$ M, regardless of solution pH. Increasing the concentration by an order of magnitude to  $C_{KCl} = 0.01$  mM, however, leads to a charge

density error that is only expected to exceed 10% if the pH is outside the approximate range of  $6 < \text{pH} < 8$  (see the supplemental material<sup>34</sup>).

### ***E. Conclusion***

In this work, we demonstrated the use of COMSOL Multiphysics to model the 2D electroosmotic flow of a dilute background electrolyte and the subsequent electrophoretic stacking or focusing of sample ions in a nanofluidic channel with selectively modified surface charge and potential. We first verified our 2D model by comparison with a simplified, approximate 1D area-averaged model for several limiting cases, and then we investigated the possible preconcentration mechanisms within the channel as the wall zeta potential was selectively varied. Our results indicate that the area-averaged electrostatic potential gradient between two regions of nonuniform, overlapped EDLs in a nanochannel generates a concentration polarization interface which can be used to efficiently focus analyte ions. In addition to this CP-based focusing mechanism, FASS-like stacking and focusing can also be achieved for charged samples of certain mobility in cases with non-overlapped EDLs. As such, it is theoretically possible to perform stationary field-amplified sample preconcentration in nanochannels without introducing multiple electrolyte solutions, but by simply inducing electric field gradients through the tailoring of wall surface potential uniformity via embedded electrodes. We show that the dominant mid-channel CP focusing effect only occurs in channels with sufficiently large step changes in zeta potential and in which the EDL thickness is comparable to or exceeds the channel height, and can even induce downstream electric field gradients for discretized analyte focusing and separation. Our results suggest that sample enhancement ratios exceeding  $10^5$  are potentially achievable, notably higher than those typically limited by sample dispersion in conventional FASS with high plug-to-background

conductivity ratios.<sup>8-11</sup> Moreover, the enhancement ratios predicted by our simulations are within an order of magnitude of the million-fold preconcentration levels that are possible using more refined nanoscale methods such as standard CP-based techniques and isotachophoresis.<sup>13,18</sup> Propagating CP effects can also enable simultaneous focusing and separation in the channel by generating extended field gradients. The efficacy and flexibility of this proposed technique leads us to conclude that there is potential for further improvement and optimization of various analyte preconcentration processes by embedding gate electrodes to manipulate local ion transport within nanofluidic channels.

### *F. Additional Simulation Details*

**Table 2.1:** Parameters used in the analytical and numerical calculations.

Parameter	Value(s)	Reference
KCl Electrolyte Solution Concentration $c_{\infty}$	1.5 $\mu$ M – 50 mM	--
Electrolyte Solution Dielectric Constant $\epsilon_f$	80.1	9
K <sup>+</sup> Diffusivity $D_{K^+}$	1.96 x 10 <sup>-9</sup> m <sup>2</sup> s <sup>-1</sup>	3
Cl <sup>-</sup> Diffusivity $D_{Cl^-}$	2.03 x 10 <sup>-9</sup> m <sup>2</sup> s <sup>-1</sup>	3
Sample Ion Diffusivity $D_s$	0.5 x 10 <sup>-9</sup> m <sup>2</sup> s <sup>-1</sup>	6
Simulated Channel Length $L$	10 $\mu$ m – 0.5 mm	--
Simulated Channel Height $H$	50 nm – 100 nm	--
Applied Electric Field Strength $V_{app} / L$	10 kV/m – 40 kV/m	--
Zeta Potential $\zeta$	-100 mV – 0 V	--
Wall Surface Charge $\sigma_w$	-1.5 mC m <sup>-2</sup> , -0.075 mC m <sup>-2</sup>	--
Zeta Potential Transition Length $\delta$	5 nm	--

### ***G. Acknowledgement***

We greatly acknowledge our funding sources, the Institute for Collaborative Biotechnologies through grant W911NF-09-001 from the U.S. Army Research Office, and grant DAAD19-03-D-0004 from the U.S. Army Research Office.

## References

1. T. C. Kuo, D. M. Cannon, Y. Chen, J. J. Tulock, M. A. Shannon, J. V. Sweedler, and P. W. Bohn, Gateable Nanofluidic Interconnects for Multilayered Microfluidic Separation Systems, *Anal. Chem.* **75**, 1861 (2003).
2. M. Napoli, J. C. T. Eijkel, and S. Pennathur, Nanofluidic technology for biomolecule applications: a critical review, *Lab Chip* **10**, 957 (2010).
3. Y. Ai, J. Liu, B. Zhang, and S. Qian, Field Effect Regulation of DNA Translocation through a Nanopore, *Anal. Chem.* **82**, 8217 (2010).
4. W. Sparreboom, A. van den Berg, and J. C. T. Eijkel, Principles and applications of nanofluidic transport, *Nature Nanotechnology* **4**, 713 (2009).
5. Y. Liu and L. Yobas, Slowing DNA Translocation in a Nanofluidic Field-Effect Transistor, *ACS Nano* **10**, 3985 (2016).
6. D. Stein, Z. Deurvorst, F. H. J. van der Heyden, W. J. A. Koopmans, A. Gabel, and C. Dekker, Electrokinetic Concentration of DNA Polymers in Nanofluidic Channels, *Nano Letters* **10**, 765 (2010).
7. J. Fu, R. B. Schoch, A. L. Stevens, S. R. Tannenbaum, and J. Han, A patterned anisotropic nanofluidic sieving structure for continuous-flow separation of DNA and proteins, *Nature Nanotechnology* **2**, 121 (2007).
8. D. S. Burgi and R. L. Chien, Optimization in sample stacking for high-performance capillary electrophoresis, *Anal. Chem.* **63**, 2042 (1991).
9. R. Bharadwaj and J. G. Santiago, Dynamics of field-amplified sample stacking, *J. Fluid. Mech.* **543**, 57 (2005).

10. J. M. Sutarich, B. D. Storey, and S. Pennathur, Field-amplified sample stacking and focusing in nanofluidic channels, *Phys. Fluids* **22**, 112003 (2010).
11. B. Jung, R. Bharadwaj, and J. G. Santiago, Thousandfold signal increase using field-amplified sample stacking for on-chip electrophoresis, *Electrophoresis* **24**, 3476 (2003).
12. Q. Pu, J. Yun, H. Temkin, and S. Liu, Ion-Enrichment and Ion-Depletion Effect of Nanochannel Structures, *Nano Letters* **4**, 1099 (2004)
13. Y. C. Wang, A. L. Stevens, and J. Han, Million-fold Preconcentration of Proteins and Peptides by Nanofluidic Filter, *Anal. Chem.* **77**, 4293 (2005).
14. A. Mani, T. A. Zangle, and J. G. Santiago, On the Propagation of Concentration Polarization from Microchannel-Nanochannel Interfaces Part I: Analytical Model and Characteristic Analysis, *Langmuir* **25**, 3898 (2009).
15. T. A. Zangle, A. Mani, and J. G. Santiago, Theory and experiments of concentration polarization and ion focusing at microchannel and nanochannel interfaces, *Chem. Soc. Rev.* **39**, 1014 (2010).
16. A. Plecis, C. Nanteuil, A. Haghiri-Gosnet, and Y. Chen, Electropreconcentration with Charge-Selective Nanochannels, *Anal. Chem.* **80**, 9542 (2008).
17. S. J. Kim, Y. Song, and J. Han, Nanofluidic concentration devices for biomolecules utilizing ion concentration polarization: theory, fabrication, and applications, *Chem. Soc. Rev.* **39**, 912 (2010).
18. B. Jung, R. Bharadwaj, and J. G. Santiago, On-Chip Millionfold Sample Stacking Using Transient Isotachophoresis, *Anal. Chem.* **78**, 2319 (2006).
19. W. L. Hsu, D. W. Inglis, M. A. Startsev, E. M. Goldys, M. R. Davidson, and D. J. Harvie, Isoelectric focusing in a silica nanofluidic channel: effects of electromigration and electroosmosis, *Anal. Chem.* **86**, 8711 (2014).

20. W. L. Hsu, D. J. Harvie, M. R. Davidson, H. Jeong, E. M. Goldys, and D. W. Inglis, Concentration gradient focusing and separation in a silica nanofluidic channel with a non-uniform electroosmotic flow, *Lab Chip* **14**, 3539 (2014).
21. R. B. M. Schasfoort, S. Schlautmann, J. Hendrikse and A. van den Berg, Field-effect flow control for microfabricated fluidic networks, *Science* **286**, 942 (1999).
22. A. E. Herr, J. I. Molho, J. G. Santiago, M. G. Mungal, and T. W. Kenny, Electroosmotic Capillary Flow with Nonuniform Zeta Potential, *Anal. Chem.* **72**, 1053 (2000).
23. L. M. Fu, J. Y. Lin, and R. J. Yang, Analysis of electroosmotic flow with step change in zeta potential, *J. Colloid Interface Sci.* **258**, 266 (2003)
24. G. Pardon and W. van der Wijngaart, Modeling and simulation of electrostatically gated nanochannels, *Adv. Colloid Interface Sci.* **199-200**, 78 (2013).
25. R. Karnik, R. Fan, M. Yue, D. Li, P. Yang, and A. Majumdar, Electrostatic Control of Ions and Molecules in Nanofluidic Transistors, *Nano Letters* **5**, 943 (2005).
26. H. Daiguji, Y. Oka, and K. Shirono, Nanofluidic Diode and Bipolar Transistor, *Nano Letters* **5**, 2274 (2005).
27. T. Maleki, S. Mohammadi, and B. Ziaie, A nanofluidic channel with embedded transverse electrodes, *Nanotechnology* **20**, 105302 (2009).
28. Y. J. Oh, A. L. Garcia, D. N. Petsev, G. P. Lopez, S. R. J Brueck, C. F. Ivory, and S. M. Han, Effect of wall-molecule interactions on electrokinetic transport of charged molecules in nanofluidic channels during FET flow control, *Lab Chip* **9**, 1601 (2009).
29. H. Daiguji, Ion transport in nanofluidic channels, *Chem. Soc. Rev.* **39**, 901 (2010).
30. Z. Jiang and D. Stein, Charge regulation in nanopore ionic field-effect transistors, *Phys. Rev. E* **83**, 031203 (2011).

31. X. Jin and N. R. Aluru, Gated transport in nanofluidic devices, *Microfluid Nanofluid* **11**, 297 (2011).
32. W. Guan, S. X. Li, and M. A. Reed, Voltage gated ion and molecule transport in engineered nanochannels: theory, fabrication, and applications, *Nanotechnology* **25**, 122001 (2014).
33. S. H. Lee, H. Lee, T. Jin, S. Park, B. J. Yoon, G. Y. Sung, K. B. Kim, and S. J. Kim, Sub-10 nm transparent all-around-gated ambipolar ionic field effect transistor, *Nanoscale* **7**, 936 (2015).
34. See Supplemental Material at <http://link.aps.org/supplemental/10.1103/PhysRevFluids.2.124203>.
35. D. Stein, M. Kruithof and C. Dekker, Surface-Charge-Governed Ion Transport in Nanofluidic Channels, *Phys. Rev. Lett.* **93**, 035901 (2004).
36. K. L. Jensen, J. T. Kristensen, A. M. Crumrine, M. B. Andersen, H. Bruus, and S. Pennathur, Hydronium-dominated ion transport in carbon-dioxide-saturated electrolytes at low salt concentration in nanochannels, *Phys Rev. E* **83**, 056307 (2011)
37. L. H. Yeh, Y. Ma, S. Xue, and S. Qian, Gate manipulation of ionic conductance in a nanochannel with overlapped electric double layers, *Sensors and Actuators B* **215**, 266 (2015).
38. C. Hughes, L. H. Yeh, and S. Qian, Field Effect Modulation of Surface Charge Property and Electroosmotic Flow in a Nanochannel: Stern Layer Effect, *J. Phys. Chem. C* **117**, 9322 (2013).
39. F. Baldessari and J. G. Santiago, Corrigendum to “Electrokinetics in nanochannels. Part I. Electric double layer overlap and channel-to-well equilibrium” [*J. Colloid Interface Sci.* **325** (2008) 526-538], *J. Colloid Interface Sci.* **331**, 549 (2009).

40. C. McCallum and S. Pennathur, Accounting for electric double layer and pressure gradient-induced dispersion effects in microfluidic current monitoring, *Microfluid Nanofluid* **20**, 13 (2016).
41. S. Behrens and D. G. Grier, The Charge of Glass and Silica Surfaces, *J. Chem. Phys.* **115**, 6716 (2001).
42. K. G. H. Janssen, J. C. T. Eijkel, N. R. Tas, L. J. de Vreede, T. Hankemeier and H. J. van der Linden, Electrocavitation in Nanochannels, 15th International Conference on Miniaturized Systems for Chemistry and Life Sciences October 2-6, 2011, Seattle, Washington, USA
43. J. M. de Rutte, K. G. H. Janssen, N. R. Tas, J. C. T. Eijkel, and S. Pennathur, Numerical investigation of micro- and nanochannel deformation due to discontinuous electroosmotic flow, *Microfluidics and Nanofluidics* **20**, 150 (2016)

### **III. Bipolar Electrochemistry in Confined Geometries**

#### ***A. Abstract***

We present the most comprehensive 2D numerical model to date for a nanoconfined bipolar electrochemical system. By accounting for the compact Stern layer and resolving the diffuse part of the electrical double layer (EDL) at the BPE surface and channel walls, our model captures the impact of surface polarization and ionic charge screening effects on the heterogeneous charge-transfer kinetics, as well as nonlinear electrokinetic transport phenomena such as induced-charge electroosmosis and concentration polarization. We employ the Poisson-Nernst-Planck and Stokes flow system of equations, unified with generalized Frumkin-Butler-Volmer reaction kinetics, to describe water electrolysis reactions and the resulting transport of ions and dissolved gases in the confined bipolar electrode (BPE) system. Our results demonstrate that under a sufficiently large applied electric field, the rapid reaction kinetics on our Pt BPE dynamically transition from charge-transfer limited to mass-transfer limited temporal regimes as regions depleted of redox species form and propagate outwards from the respective BPE poles. This phenomenon was visualized experimentally with pH-sensitive fluorescein dye and showed excellent phenomenological agreement with our numerical calculations, providing a foundation for further understanding and developing bipolar electrochemical processes in confined geometries. This chapter was reproduced in part with permission from the Journal of Physical Chemistry C, in press. Unpublished work copyright 2019 American Chemical Society (DOI: 10.1021/acs.jpcc.8b10473).

## ***B. Introduction***

Bipolar electrochemistry involves a conductive material that is immersed in an ionic solution and electronically isolated from external circuitry. When an electric field is applied within this solution, internal electron redistribution leads to charge polarization at two distinct poles of the equipotential conductor. If a sufficiently high interfacial potential difference develops between the polarized surface and the adjacent ionic solution containing redox-active molecules, charge transfer by oxidation-reduction reactions can simultaneously proceed at the two poles to pass current through the material.<sup>1,2</sup> This technique provides a flexible platform for fluidic on-chip integration of wireless electrochemical processes such as analyte focusing and separation,<sup>3</sup> biosensing and molecular-level detection,<sup>4-6</sup> multiplexed electrocatalyst<sup>7</sup> and metabolite<sup>8</sup> screening, surface patterning,<sup>9</sup> and self-propulsion of particles.<sup>10,11</sup> Enabled by modern microfabrication technologies, the integration of bipolar electrochemistry into micro- and nanofluidic platforms offers unprecedented analytical advantages such as small sample volume manipulation, increased surface interactions due to high geometric aspect ratios, and increased processing throughput via parallelization. The confinement of ionic and molecular species to nanometer-scale geometries can significantly alter physical transport phenomena, however, as conventional macroscopic assumptions of electroneutrality and limiting currents break down when surface effects and charge-screening electrical double layers (EDLs) become significant relative to the system size.<sup>12-16</sup>

The structure of the EDL directly affects the kinetics of electrochemical reactions. These effects are not explicitly treated in traditional macroscopic models<sup>17,18</sup> which, instead, empirically incorporate EDL effects by measuring the electrode potential relative to some equilibrium value measured in the “bulk” solution or calculated via the Nernst equation. The first to thoroughly investigate EDL effects on electrochemical kinetics was Frumkin,<sup>19</sup> who

concluded that the implications of such effects for Faradaic charge transfer reactions are primarily twofold: 1) the electrostatic interactions between polarized electrodes and charged redox-active species alter reactant concentrations at the reaction plane (located at the Stern/diffuse layer interface of the EDL<sup>12</sup>), and 2) diffuse charge screening and capacitive effects from the compact Stern layer alter the effective driving potential of a redox reaction by introducing an additional reaction plane potential contribution, known as the zeta potential, to the classical overpotential definition.<sup>18,19</sup> Modifications such as the Frumkin correction have been introduced to account for EDL effects on charge transfer rates,<sup>17,20</sup> but these approaches are limited to describing idealized EDLs with Boltzmann-distributed ions which remain in thermal equilibrium. In real electrochemical systems, however, EDLs can be perturbed from equilibrium if sufficient current is passed across the conductor/electrolyte interface.<sup>14,18,20</sup> Moreover, finite-sized EDLs in nanochannels and substantial reaction-induced changes in redox species concentrations at the electrode can lead to local deviations from “bulk” conditions of electroneutrality and uniform conductivity. In some cases, this results in the formation of nonequilibrium space charge regions which can extend considerable distances away from the electrode surface to generate ion concentration polarization zones.<sup>21-</sup>  
<sup>24</sup> Hence, previous macroscopic theories which require knowledge of some “bulk” reference condition are inadequate for the accurate analysis of electrochemical systems under confinement.

The modeling of EDL effects on bipolar electrochemical systems is nonexistent in the literature, and the vast majority of conventional electrochemistry studies which incorporate EDLs have been centered around 1D geometries. To our knowledge, Bonnefont *et al*<sup>12</sup> were the first to fully numerically incorporate the effects described by Frumkin in a two-electrode electrochemical model using a boundary condition which Biesheuvel *et al*<sup>24</sup> later called the

generalized Frumkin-Butler-Volmer (gFBV) equation. Subsequent studies have presented models to investigate the effects of the Stern and diffuse layers on heterogeneous charge-transfer kinetics under potentiostatic<sup>13-16</sup>, and galvanostatic<sup>12,24-26</sup> conditions. These previous reports demonstrated that EDL effects can produce significant deviations from theoretical predictions such as, for example, Faradaic currents which exceed the classical diffusion-limited and reaction-limited values.<sup>14,15,24</sup> Recently, 2D models of bipolar electrochemical systems have been introduced in the literature<sup>4,27-30</sup>, though these models tend to neglect or oversimplify induced-charge electroosmotic flow (ICEOF)<sup>4,27,28,30</sup>, ignore homogeneous reactions<sup>28-30</sup>, assume bulk electroneutrality,<sup>28,30</sup> employ charge-transfer limited (and thus, mass-transfer independent) Butler-Volmer kinetics,<sup>29</sup> and/or impose some experimentally measured net reaction current as a numerical boundary condition.<sup>27</sup> By contrast, we tie together for the first time the microscopic effects predicted by Frumkin with conventional continuum-based transport equations to describe in nanometer-scale detail the 2D spatiotemporal evolution of ionic charge and dissolved gases within a confined bipolar electrode (BPE) system.

In this work, we study the predicted charging dynamics, steady-state conditions, and discharging dynamics of a nanochannel-confined BPE system (Figure 3.1). Using fluorescence experiments to validate the model, we demonstrate that the combination of small fluid volumes in nanochannels and the facile electrochemical kinetics of Pt surfaces can lead to mass-transfer limited reaction regimes in which extended regions of redox species accumulation/depletion propagate throughout the entire channel. Moreover, the nonequilibrium EDLs formed at the BPE can lead to significant electrostatic interactions with charged molecules which can only be experimentally observed in nanoscale geometries. We also briefly discuss the implications of ICEOF, oxide growth, and buffer reactions on the

dynamics of our system before introducing a potential method for estimating homogeneous reaction rates through numerical modeling. Our model demonstrates excellent qualitative agreement with experimental observations and provides the most complete analysis to date of the complex mass transport and reaction kinetics encountered in the field of bipolar electrochemistry.

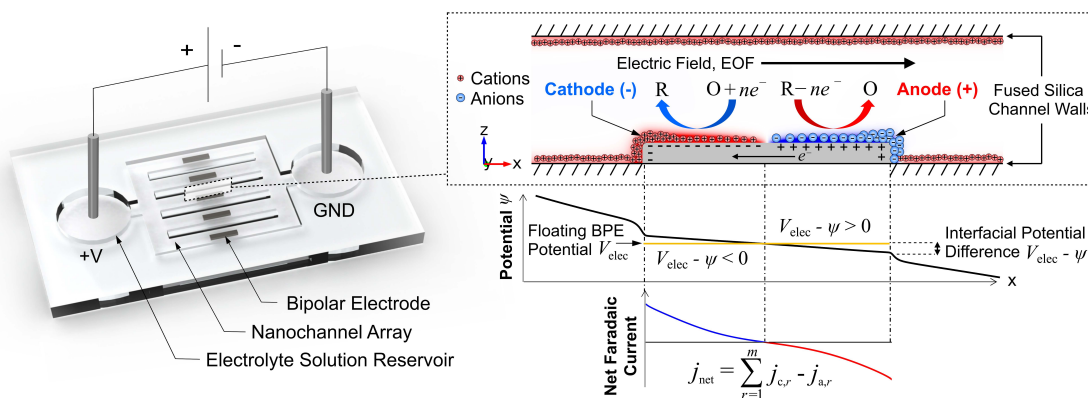


**Figure 3.1:** Schematic overview of a nanofluidic device containing a bipolar electrode array (left), along with a more detailed picture of the electrokinetics and current-voltage characteristics at the BPE surface (right). An externally applied potential difference between the driving electrodes in the reservoirs generates an electric field which wirelessly induces coupled redox reactions at the BPE poles.

### C. Theory and Simulation

#### 1. Numerical Model Overview

To understand the roles of the various competing transport mechanisms within our confined BPE system, we developed a 2D numerical model using the commercial finite-element package COMSOL Multiphysics v5.3a. Our model simulates water electrolysis reactions at a BPE surface and the resulting electrokinetic transport by advection, migration (where applicable), and diffusion throughout the system. The model considers ions within 0.1 mM and 1.0 mM sodium phosphate buffer solutions, redox-active species, and a dianionic fluorescein (FL) dye tracer, which we used experimentally to monitor electrokinetic events in

real time. To represent our geometry in 2D, we modeled a cross-section of the nanochannel spanning from the anodic reservoir to the cathodic reservoir, passing through the BPE at its center (Figures 3.1, 3.2). The simulated microscale electrolyte reservoirs at the ends of the nanochannel are, in reality, situated below much larger reservoirs which are assumed to be uniform in composition at some specified bulk value. Furthermore, the channel and BPE are assumed to be wide enough that the transport conditions are not appreciably affected by translation of the plane a small distance in the y-direction from this central location; thus, a 2D representation of the system is adequate for our analysis.

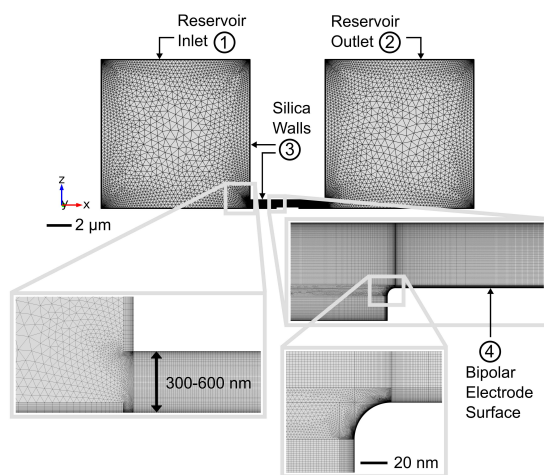


**Figure 3.2:** Computational domain, select boundaries, and finite element mesh discretization for the 2D numerical model.

Simulating the electrokinetic transport and Faradaic charge transfer involved in our nanoconfined BPE system required a highly customized finite-element mesh discretization due to the inherent numerical stiffness of the transport equations. That is, our model must resolve the large electrostatic and ionic gradients predicted near the channel wall and BPE surfaces while still allowing for a time-efficient numerical calculation under the computational restrictions of the hardware. To address these challenges we created a multiscale model

which is capable of resolving six spatial orders of magnitude, spanning from the very edge of continuum theory to several hundred micrometers in length (Figure 3.2). We improved time and computational efficiency by simulating a shorter 5  $\mu\text{m}$  long channel with a 1.67  $\mu\text{m}$ -long BPE, relative to the 1 cm long channel and 500  $\mu\text{m}$  long BPE used in our experiments. With this model, we aimed to study the response of the BPE to a step-change in potential, after which the disparate time scales of electrode polarization, heterogeneous charge transfer kinetics, and ionic charge transport lead to a dynamic progression of the system towards a steady state condition. To capture elusive, ultra-fast dynamic processes, we modeled the potential switching event as a smoothed step function which transitions over 5 ns. The experimental time scale of such transitions, however, will practically be limited by the capabilities of the external power supply used.

## 2. Theoretical Framework and Governing Equations

The relevant Faradaic reactions in our system are the hydrogen evolution and oxidation reactions (HER and HOR), as well as the oxygen evolution and reduction reactions (OER and ORR). The preferred pathways and mechanisms for these reactions vary depending on solution pH.<sup>18,31,32</sup> In acidic and alkaline solutions, respectively, the final balance equations for the reversible HER/HOR reaction are given by<sup>18</sup>



The final OER/ORR reaction equations in acidic and alkaline solutions, respectively, are given by<sup>31</sup>



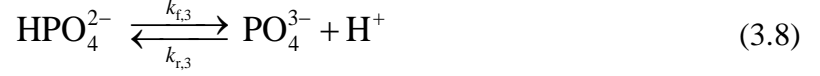


We modeled equations (3.1) - (3.4) as coupled, chemically reversible reactions; that is, the reactions occurring at one BPE pole can influence those occurring at the opposing pole at any given time by redox cycling. For example, dissolved hydrogen gas produced at the cathode can presumably be transported by advection and diffusion to the anode, where it can then be oxidized to produce protons in accordance with equation (3.1).

To describe the transport of the ten different dilute chemical species present in our system (namely,  $\text{H}^+$ ,  $\text{OH}^-$ ,  $\text{H}_2$ ,  $\text{O}_2$ ,  $\text{Na}^+$ ,  $\text{H}_3\text{PO}_4$ ,  $\text{H}_2\text{PO}_4^-$ ,  $\text{HPO}_4^{2-}$ ,  $\text{PO}_4^{3-}$ ,  $\text{FL}^{2-}$ ), we use the transient species conservation equation, assuming Nernst-Planck fluxes,<sup>33</sup>

$$\frac{\partial c_i}{\partial t} = -\nabla \cdot \left( \mathbf{u}c_i - D_i \nabla c_i - \frac{D_i}{RT} z_i F c_i \nabla \psi \right) + R_i, \quad (3.5)$$

where  $c_i$  is the concentration of species  $i$ ,  $\mathbf{u}$  is the fluid velocity vector,  $D_i$  is the diffusion coefficient of species  $i$ ,  $z_i$  is the valence of species  $i$ ,  $R$  is the ideal gas constant,  $T$  is the solution temperature (assumed to be fixed at 25°C),  $F$  is Faraday's constant,  $\psi$  is the electrostatic fluid potential, and  $R_i$  is the homogeneous reaction source term for species  $i$  (where applicable). This equation is the same as the species conservation equation introduced in Chapter II, with the exception that we have combined the transverse and applied EDL potentials into one variable and included homogeneous reactions. Note again that equation (3.5) assumes a Nernst-Einstein relation,  $\mu_i = D_i / (RT)$ , for the ionic mobilities.<sup>34</sup> We include the triprotic phosphoric acid association/dissociation reactions as source terms in equation (3.5) to account for the buffering effect of protons produced and consumed at the BPE surface for a wide range of possible pH values,



Additionally, we include the self-ionization of water,



where  $k_f$  and  $k_r$  respectively denote the forward and reverse rate constants for each reaction. See the Supporting Information for the numerical formulation of homogeneous reaction source terms and their associated rate constants.

We modeled the mean-field potential distribution  $\psi$  arising from solvent polarization in the presence of an applied potential and electrostatic interactions between charged surfaces and ionic counter-charge via Poisson's equation:

$$-\nabla \cdot (\varepsilon \nabla \psi) = \sum_{i=1}^m F z_i c_i \quad (3.10)$$

where  $\varepsilon$  is the permittivity of the solvent (i.e. water). As with equation (3.5), this equation is identical to that presented in Chapter II if the transverse and applied potentials are not separated. Equations (3.5) and (3.10) together form the Poisson-Nernst-Planck system of equations; these equations are subsequently coupled to conservation of mass and momentum to solve for electroosmotic flow (EOF) of the solvent fluid, which arises due to tangential Coulombic forces within the EDLs when an electric field is applied along the axis of the channel. For nanofluidic systems, the inherent dominance of viscous effects allows us to

describe the conservation of momentum for an incompressible, Newtonian fluid using the time-dependent Stokes equation and mass continuity,

$$\rho \frac{\partial \mathbf{u}}{\partial t} = \eta \nabla^2 \mathbf{u} - \nabla P - \sum_{i=1}^m F z_i c_i \nabla \psi; \quad \nabla \cdot \mathbf{u} = 0 \quad (3.11)$$

where  $\rho$  is the mass density of the fluid.

A concentration-dependent formulation of the charge transfer kinetics is necessary to capture dynamic shifts in reaction rates as reactants are rapidly consumed at our platinum BPE. As predicted by Frumkin, the surface concentrations of these redox-active species can be altered significantly by electrostatic interactions at the polarized metal-electrolyte interface. We therefore implement the generalized Frumkin-Butler-Volmer (gFBV) equations to capture these microscopic effects in describing the electrochemical kinetics of a redox couple with concentrations  $c_{\text{ox}}$  and  $c_{\text{red}}$  located just outside the Stern layer of an electrode. Electron transfer events theoretically take place at this location, from which liberated electrons tunnel across the solvation layer(s) and into the metal.<sup>14,15,24</sup> The interfacial charge transfer from these reactions produces a flux of electrons that can be described by a reaction rate with a potential dependent Arrhenius form for the kinetic rate constants,

$$j = K_c c_{\text{ox}} \exp\left(-\frac{\alpha_c n F \Delta V_s}{RT}\right) - K_a c_{\text{red}} \exp\left(\frac{\alpha_a n F \Delta V_s}{RT}\right), \quad (3.12)$$

where  $j$  is the local reaction current density,  $K_c$  is the cathodic rate constant,  $\alpha_c$  is the cathodic charge transfer coefficient,  $n$  is the number of electrons transferred per reaction,  $\Delta V_s$  is the interfacial potential difference between the BPE and the Stern/diffuse layer interface of the EDL,  $K_a$  is the anodic rate constant, and  $\alpha_a$  is the anodic charge transfer coefficient. In our model, the interfacial potential difference, and thus the surface charge and concentration of reacting species, vary at each point along the BPE surface. To account for

the pH-dependence of equations (3.1)-(3.4), we include all possible reactions simultaneously and introduce a scaling factor to formulate effective cathodic and anodic rate constants based on the local pH near the respective BPE poles (see the Supporting Information for more details).

We adopt the model of Stern<sup>14,35,36</sup> to relate the local surface charge of the BPE,  $\sigma_{\text{BPE}}$ , (in the absence of specific adsorption) to the interfacial potential difference,  $\Delta V_s = (V_{\text{elec}} - \psi)|_s$ ,

$$\sigma_{\text{BPE}} = \mathbf{n} \cdot \nabla (\varepsilon \psi) = C_s (V_{\text{elec}} - \psi)|_s, \quad (3.13)$$

where  $C_s$  is an effective capacitance of the Stern layer and  $V_{\text{elec}}$  is the potential of the floating BPE. The potential  $V_{\text{elec}}$  is determined through a nontrivial balance of all surface current terms; any imbalance between cathodic and anodic currents at the poles leads to net charge accumulation and a shift in the electrode potential over time. Thus, the difference between partial cathodic and anodic current densities from all possible redox reactions must equal the capacitive displacement current when integrated over the BPE surface,

$$\int_{\partial\Omega} j_{\text{net}} dS = \int_{\partial\Omega} C_s \frac{\partial (V_{\text{elec}} - \psi)|_s}{\partial t} dS, \quad (3.14)$$

where  $j_{\text{net}}$  is the net local Faradaic current density due to all reactions.

The Stern layer can be approximated as immobilized charge separated by a distance  $\lambda_s$  (commonly approximated as the radius of a solvated ion<sup>15</sup>), the capacitance of which is given by  $C_s = \varepsilon / \lambda_s$ . Large surface charge densities and their associated electric fields can reduce the degree of polarizability for strongly oriented solvent molecules in the EDLs, leading to a dielectric constant which deviates from the bulk zero-field value. This nonlinear polarization effect can be described by Booth's equation,<sup>37,38</sup> given by  $\varepsilon_r(E) = n_0^2 + 3(\varepsilon_r(0) - n_0^2)(\beta E)^{-1} [\coth(\beta E) - (\beta E)^{-1}]$ , where  $\varepsilon_r$  is the dielectric constant,

$E$  is the electric field strength,  $n_0$  is the refractive index, and  $\beta$  is a numerical constant. At steady state, equation (3.14) reduces to finding a value of  $V_{\text{elec}}$  such that there is a balance between the current entering the BPE at the cathode and the current leaving the BPE at the anode. Note that we neglect metal dissolution/deposition and the formation of surface layers at the BPE which would influence local charge transfer rates, such as kinetically passivating oxides which have been shown to form after high levels of sustained anodic oxidation.<sup>39</sup> The specific simulation parameters we used can be found in the Supporting Information, and the numerical boundary conditions are listed in Table 3.1.

**Table 3.1:** Numerical boundary conditions for the 2D model at the various surfaces indicated in Figure 3.2.

Boundary	Boundary Condition		
	Poisson's Equation	Species Conservation <sup>a</sup>	Stokes Equation & Continuity
1	$\psi = V_{\text{app}}(t)$	$c_i = c_{i,\infty}$	$p = 0$
2	$\psi = 0$	$c_i = c_{i,\infty}$	$p = 0$
3	$\mathbf{n} \cdot \nabla (\varepsilon \psi) = \sigma_w$ <sup>b</sup>	$-\mathbf{n} \cdot \mathbf{N}_i = 0$	$\mathbf{u} = 0$
4	$\mathbf{n} \cdot \nabla (\varepsilon \psi) = C_S (V_{\text{elec}} - \psi)$  $\int_{\partial\Omega} j_{\text{net}} dS = \int_{\partial\Omega} C_s \frac{\partial (V_{\text{elec}} - \psi)}{\partial t} dS$ <sup>c</sup>	$-\mathbf{n} \cdot \mathbf{N}_j = 0$  $-nF (\mathbf{n} \cdot \mathbf{N}_r) = \nu_r j_r$	$\mathbf{u} = 0$

<sup>a</sup> The subscript  $i$  represents all species, the subscript  $r$  indicates redox-active species only, and the subscript  $j$  corresponds to electrolyte species that are not redox-active.  $c_{i,\infty}$  corresponds to the bulk concentration of species  $i$  (see Table 3.5), and  $\nu_r$  is the stoichiometric coefficient of species  $r$ .

<sup>b</sup> We assume a fixed silica glass surface charge for simplicity, though realistically this value will depend on the local solution pH.<sup>36</sup>

<sup>c</sup> This equation is not, strictly speaking, a boundary condition, but is used to solve for the floating electrode potential  $V_{\text{elec}}$  and thus the local surface charge boundary condition at the BPE surface.

#### ***D. Experimental Methods***

We fabricated the BPE chips using standard planar photolithographic techniques. Briefly, we etched nanofluidic channels 300-600 nm tall, 500  $\mu\text{m}$  wide, and 1 cm long into fused silica glass wafers using reactive ion etching. Following this, we deposited 80 nm of Pt with a 20 nm Ti adhesion layer in the channels via thermal evaporation to form 500  $\mu\text{m}$  long, 125  $\mu\text{m}$  wide electrically-isolated electrodes. We then drilled fluidic access holes into separate fused silica wafers, which we bonded via room-temperature  $\text{N}_2$  and  $\text{O}_2$  plasma activation to the substrates containing the nanochannels and electrodes. To increase the working fluid volume

in the reservoirs and reduce adverse evaporation effects, we placed the devices in a custom micromachined chip holder for the duration of the experiments.

We performed all fluorescence experiments with an epifluorescence setup (Olympus IX73 inverted microscope, obtained from Olympus, Center Valley, PA, coupled to Andor Technology iXon Ultra EMCCD camera, purchased from Oxford Instruments, Concord, MA). Prior to analysis, we serially treated the nanofluidic chips via vacuum with aqueous 0.1 M NaOH solutions for 15 min, deionized water for 5 min (twice), and finally the solution of interest (a mixture of 100  $\mu$ M sodium fluorescein and 1.0 mM sodium phosphate buffer at pH 7.5) for 5 min. At this point, we introduced one Pt wire into each reservoir. To run the experiments, we applied 250 V between the Pt electrodes for 30 s using a Keithley 2410 voltage source. No visual or electrical signal obstruction from gas bubble formation was observed during these experiments (this was only observed in our device for applied potential differences exceeding 600 V). We acquired fluorescence images at a rate of 3.2995 Hz for 2.53 min using excitation and emission filters specific to fluorescein (i.e.,  $\lambda_{\text{ex}} = 494$  nm and  $\lambda_{\text{em}} = 521$  nm). We subtracted background signals and analyzed images with ImageJ v2 1.52e and custom Python v3.6.3 scripts.

## ***E. Results***

### **1. BPE Charging Dynamics**

Four distinct time scales characterize the ionic transport and electrochemical response of our nanoconfined BPE system when the voltage is turned on: 1) BPE polarization accompanied by the initial formation of EDLs at the Debye time scale, 2) charging of these EDLs at the Ohmic time scale, 3) heterogeneous charge transfer on the order of the Faradaic relaxation time, and 4) mass transport at the diffusion time scale.<sup>13,15,40,41</sup> Similarly, BPE

discharging proceeds with disparate time scales immediately after the voltage is turned off, a process which we leave for future discussion. In both cases, however, such time scales vary between our experimental device and numerical model due to differences between geometrical length dimensions, as well as the neglected presence of Pt oxides and FL adsorption on the BPE surface. Moreover, these time scales are difficult to quantify experimentally at early times due to practical restrictions on electronic hardware and frame-capture rates, but numerical methods offer sufficient time-resolution of these processes over many orders of magnitude; therefore, in this section we discuss only the charging dynamics of the nanoconfined BPE system as predicted by our model.

Before any potential difference is introduced across the fluid reservoirs, equilibrium conditions are maintained at the BPE surface and channel walls. That is, only the channel wall EDLs are fully formed and the BPE remains unpolarized. As an external potential of 1.6 V is applied to the driving electrodes, solvent polarization induces a nonzero field throughout the channel within a matter of picoseconds.<sup>42</sup> If the potential is ramped up on a slower time scale than this, which is the case for our simulations (5 ns) and is generally true for electronic equipment operating in direct current (DC) mode, solvent polarization will be seen to occur instantly. In response, electrons within the BPE quickly migrate towards the higher fluid potential at left BPE edge (Figure 3.1). This preferential electron redistribution causes the BPE to float to a uniform potential, producing a nonuniform interfacial electrode/electrolyte potential difference along the metal surface and segregating the BPE into a negatively charged cathodic pole at one end and a positively charged anodic pole at the other end.

The field-induced solvent polarization produces motion of ionic charges to electrostatically screen the nonuniform BPE surface charge and subsequently form EDLs on the order of the Debye time,  $\tau_D = \lambda_D^2 / D$ , where  $D$  is a characteristic diffusion coefficient and  $\lambda_D$  is the Debye

screening length<sup>15</sup> (Table 3.2). For moderate to large surface charge densities, the accumulation of counter-ions is delayed by mass transport effects which slow EDL charging to the Ohmic relaxation time, given by  $\tau_O = R_{\text{bulk}} C_{\text{EDL}}$ , where  $R_{\text{bulk}}$  is the characteristic bulk solution resistance and  $C_{\text{EDL}}$  is the characteristic EDL surface capacitance.<sup>40</sup> The rates of any subsequent electrochemical reactions are fundamentally linked to the evolving EDL structure by virtue of Frumkin's formalism, but the rate at which charge transfer can occur across the metal/electrolyte phase boundary is ultimately determined by heterogeneous reaction kinetics. Therefore, a similar RC time constant for Faradaic relaxation follows using the characteristic charge transfer resistance  $R_{\text{ct}}$  to yield  $\tau_{\text{ct}} = R_{\text{ct}} C_{\text{EDL}}$ . Faster reaction kinetics are expressed as lower charge transfer resistances, which can ultimately “short-circuit” EDL charging at extreme values and cause the current to bypass the fluid above the BPE due to rapid electrode depolarization via charge-transfer.<sup>40,43</sup> This is possible because the Faradaic reactions occur in parallel with capacitive EDL formation, as shown in classical electrochemical models<sup>17</sup> which depict an EDL capacitance in parallel with a series combination of the charge transfer resistance and Warburg (mass-transfer) impedance. Facile kinetics with low charge transfer resistances generally lead to significant consumption of redox-active species for even modest driving potentials, which can limit reactions to the rate at which charge-carrying reactants are transported to the BPE surface. In such cases, a mass-transport limited regime will appear at the longer diffusion time  $\tau_{\text{diff}} = L^2 / D$ , where  $L$  is a characteristic length scale.<sup>15,40,41</sup>

**Table 3.2:** Time scales and characteristic values for the modeled system.

Parameter	Equation	Characteristic Value
Geometric Length	$L = L_{\text{channel}} / 2$	2.5 $\mu\text{m}$
Debye Length	$\lambda_D = \sqrt{\varepsilon RT / F^2 \sum_i a_i z_i^2}$ <sup>a</sup>	10 nm
Debye Time	$\tau_D = \lambda_D^2 / D$ <sup>b</sup>	10 ns
Bulk Conductivity	$\sigma = F^2 \sum_{i=1}^m D_i z_i^2 c_{i,\infty} / RT$	0.15 mS/cm
Bulk Resistance	$R_{\text{bulk}} = L / \sigma$	1.7 $\Omega \text{ cm}^2$
EDL Capacitance	$C_{\text{EDL}} = \varepsilon (\lambda_D + \lambda_S)^{-1}$	70 mF/m <sup>2</sup>
Ohmic Relaxation Time	$\tau_O = R_{\text{bulk}} C_{\text{EDL}}$	10 $\mu\text{s}$
Charge Transfer Resistance	$R_{\text{ct}} = RT / j_0 F$ <sup>c</sup>	2.6 $\Omega \text{ cm}^2$
Charge Transfer Relaxation Time	$\tau_{\text{ct}} = R_{\text{ct}} C_{\text{EDL}}$	20 $\mu\text{s}$
Diffusion Time	$\tau_{\text{diff}} = L^2 / D$ <sup>b</sup>	650 $\mu\text{s}$

<sup>a</sup>  $a_i$  here is the activity coefficient for species  $i$ , as our electrolyte is not monovalent,<sup>44</sup> and  $e_0$  is elementary charge.

<sup>b</sup> We use the diffusion coefficient for hydrogen,  $D_{\text{H}^+} = 9.3 \times 10^{-9} \text{ m}^2/\text{s}$  to represent the fastest response times of the system.<sup>45</sup>

<sup>c</sup>  $j_0$  is the exchange current density of the fastest reaction, modeled here as  $j_0 = 100 \text{ A/m}^2$ .

The aforementioned mass-transport effects have been thoroughly examined in previous literature.<sup>17,18,46,47</sup> For example, Haber<sup>46</sup> noted the influence of changing reactant concentrations on the Nernst equation and coined the term “concentration overpotential” to describe the subsequent effect on the classical overpotential definition  $\eta = V_{\text{elec}} - V_{\text{bulk}} - E_{\text{eq}}$ , where  $\eta$  is the overpotential and  $E_{\text{eq}}$  is the equilibrium potential. Moreover, as a particular

electrochemical reaction is confined to smaller geometries, an increasing fraction of the driving potential manifests as concentration overpotential and hindered mass-transfer effects often become rate-limiting.<sup>18</sup> In our microscopic model, this translates to a reduction in surface concentrations at the Stern/diffuse layer interface, and therefore the net reaction rate from equation (3.12). Ohmic potential drops due to reaction-induced changes in the surrounding solution composition can also cause the effective driving potential at the BPE to deviate from the expected value.<sup>17</sup>

Figure 3.3(a) reveals that the BPE initially floats to exactly half of the applied 1.6 V at early times; the surface charge and interfacial potential distribution are therefore symmetrical on the order of the Debye time  $\tau_D \sim 10$  ns. Any subsequent asymmetry in charge transfer as reactions develop causes net charge accumulation along the surface due to unbalanced electron fluxes at the poles. This is evident in Figure 3.3(b), which shows that because the HER is modeled as the fastest reaction (see Table 3.8), the cathodic reaction rate exceeds the anodic reaction rate during the Ohmic and Faradaic relaxation periods, which in our simulations are of order  $\tau_o \sim 1 \times 10^{-5}$  s and  $\tau_{ct} \sim 2 \times 10^{-5}$  s, respectively. The cathodic pole remains negatively charged during these time scales, but the magnitude of the anode charge grows to exceed that of the cathode and a net positive charge therefore accumulates (Figure 3.3(c)) because there is more current entering the cathode than leaving the anode. This charge accumulation at the BPE surface also promotes asymmetry in the EDL charging at the poles, as evidenced by the nonzero surface integral of displacement current in Figure 3.3(c) (which, by equation (3.14), is equal to the difference between partial cathodic and anodic Faradaic currents integrated over the surface).

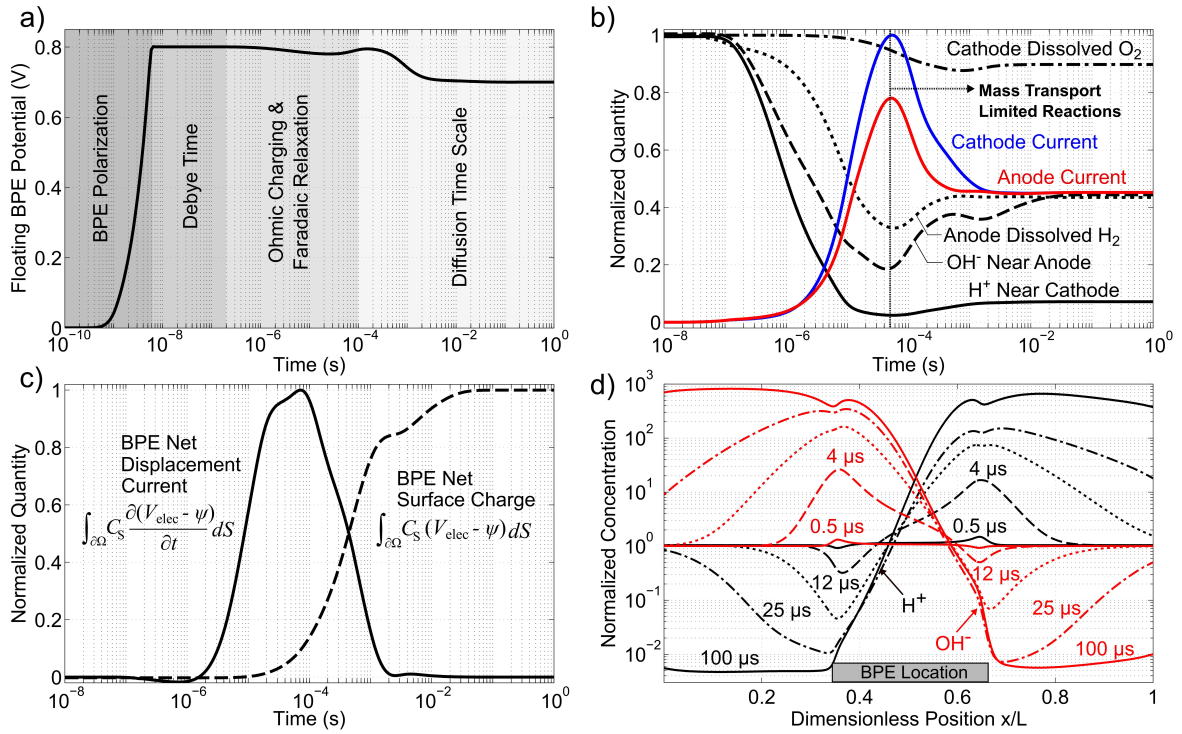


**Figure 3.3:** Charging dynamics for a 300 nm tall channel with a 1.0 mM buffer: (a) BPE floating potential at different time scales, (b) temporal evolution of redox-active reactant species and the corresponding local Faradaic current densities at or near each pole, (c) BPE surface charge and displacement current integrated over the surface, and (d) spatiotemporal evolution of  $H^+$  and  $OH^-$  concentration along the nanochannel centerline. The ionic concentrations in (b) were taken just outside the EDL adjacent to each pole, while the dissolved gas concentrations were evaluated at the surface of the BPE poles. Note that the net surface charge in (c) is the time integral of the net displacement current (which, in turn, is equal to the time integral of the net Faradaic BPE current).

The redox reactions become mass-transfer limited due to pole-localized depletion of reactants at some point between the Ohmic and the proton diffusion time scales (i.e. on the order of  $10^{-4}$  s). The spatiotemporal distribution of  $H^+$  and  $OH^-$  ions along the channel centerline demonstrates the evolution of these mass transport effects (Figure 3.3(d)). Specifically, depletion regions near the BPE poles form and propagate in the direction opposite to reactant transport (i.e. upstream propagation for  $H^+$ , downstream propagation for  $OH^-$ ) during the Faradaic and diffusion relaxation times as reactants are transported through these depleted regions to the BPE surface. Conversely, these species accumulate in the

direction of transport because the electrochemical production rate exceeds the rate of mass transport away from the surface. The distance these regions propagate after a given time can be roughly approximated by the diffusion length  $L \sim \sqrt{Dt}$  (e.g., after 120  $\mu\text{s}$ , the proton diffusion length is expected to be on the order of 1  $\mu\text{m}$ ). The real propagation distance cannot be accurately predicted solely through consideration of mass transport by diffusion, however, because the system additionally experiences ionic transport by migration and advection, as well as production/consumption by any applicable homogeneous reactions. Eventually, all combined mass transport effects at the surface balance the reaction fluxes from the charge transfer events, and the steady-state condition shown at  $t = 1$  s is attained (Figure 3.3(b)).

The concomitant production and consumption of  $\text{H}^+$  and  $\text{OH}^-$  at the respective poles leads to a dynamic pH gradient that extends a considerable distance away from the BPE, a phenomenon that has been reported in previous microfluidic studies.<sup>2,27</sup> Crooks and coworkers,<sup>3,7,10,21,27</sup> in particular, have shown that BPE-generated pH gradients can be leveraged to locally neutralize and deplete cations in Tris buffers, thereby decreasing the electrical conductivity of the solution. This nonuniform conductivity distribution generates field gradients which can induce stationary analyte focusing and separation zones in a manner analogous to ion concentration polarization.<sup>21,23,48</sup> These tunable pH and field gradients can also be employed for isoelectric focusing and separation techniques.<sup>2</sup>

Since ionic redox-active species are electrostatically attracted to the poles at which they react, there is a spatial separation between the depleted zones outside the EDLs and the locally enriched concentrations within the nonuniform EDLs (commonly referred to as the Frumkin effect).<sup>18,19</sup> The magnitude of the surface concentration is therefore highly dependent on the local surface charge magnitude and the extent of reactant depletion just outside the

EDL, both of which are fully captured by our microscopic model. As previously alluded to, it is partly due to the existence of these two distinct regions that incorporating finite EDLs can lead to currents above classical limiting values predicted by theory.<sup>14,24</sup>

## 2. Modeling Tracer Molecule Fluorescence

We qualitatively demonstrate the accuracy of our model by comparison with real-time experimental fluorescence measurements (Figure 3.4). Specifically, we aimed to elucidate the behavior of a fluorophore in the near vicinity of the BPE. The molecule we employed, fluorescein, is known to undergo pH-dependent changes in fluorescence emission;<sup>49</sup> thus, we employed FL to optically monitor the electrochemical formation of pH gradients. A range of tracer molecules with different pH-sensitivities can be employed to deduce information about the BPE charging and discharging dynamics, as well as the accompanying electrokinetic and electrochemical phenomena which return the system to equilibrium. For the purposes of this study, however, we limit our scope to thoroughly studying the steady-state distribution of fluorescein within our confined BPE system.

As a first calibration of our numerical model, we visualized the low pH “wake” that forms downstream of the anode through fluorescence quenching of the fluorophore (Figure 3.4(a)). In this experiment, the fluorescence intensity of the dye effectively drops to zero within a region starting near the edge of the BPE and extending all the way to the channel outlet (not pictured). This decreased intensity is consistent with zones of strong acidification,<sup>50</sup> as demonstrated by our experimental titration curve of fluorescence intensity vs. pH (Figure 3.4(b)).

Our model assumes that fluorescein remains a dianionic species, and we use a simple correlation factor to relate simulated “intensities” to local pH and fluorescein concentrations.

For this, we first assume that concentration and intensity are directly proportional. We then introduce an error function fitted to our empirical titration curve, which we normalize and multiply by the local concentration field to obtain effective intensities (Figure 3.4(c)). A comparison between experimental (Figure 3.4(a)) and simulated (Figure 3.4(c)) fluorescence intensity reveals excellent qualitative agreement. Specifically, the dianionic fluorescein is seen to have a locally lower intensity near the cathode edge, which our model confirms is due to electrostatic repulsion within the cathodic EDL. Conversely, electrostatic attraction is observed to locally increase the intensity at the anode; however, this local enhancement is obscured by quenching above the anode edge that is both observed experimentally and predicted numerically. These EDL effects are only observable when the BPE is confined within a nanochannel containing a sufficiently dilute electrolyte solution, such that the EDLs occupy a noticeable fraction of the channel cross-section. This knowledge of analyte behavior in the vicinity of the BPE can be leveraged for the purposes of detecting biorelevant molecules via pH-sensitive reporters and electrochemiluminescence (ECL) quenching.<sup>50</sup>

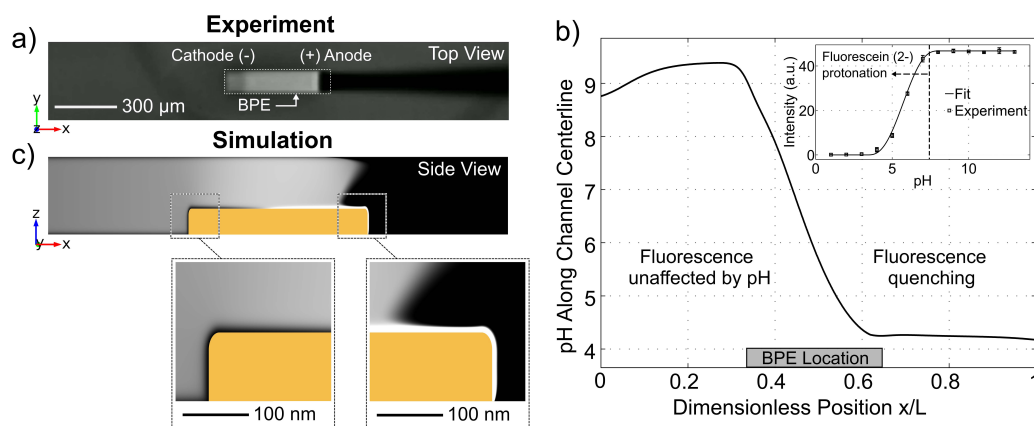


**Figure 3.4:** (a) Fluorescence experiments with pH-sensitive FL dye in a 1.0 mM buffer solution, (b) example of a simulated pH curve along the channel centerline showing regions of quenching predicted by the inset experimental titration curve, and (c) simulated 2D FL intensity profile.

### 3. BPE-Induced Ion Concentration Polarization

Concentration polarization can also be achieved using a confined bipolar electrode, without the necessity for overlapping EDLs. To understand how this process occurs, we revisit our ion transport velocity analysis from Chapter II (Figure 2.6). The phosphate buffer anions present in our system each have a relatively low mobility (Table 3.6), so they are prone to downstream transport (the opposite direction as the natural migration tendency) in regions of lower electric field and relatively high flow velocity. Recall that in our prior analysis, the area-averaged velocity in each region of the channel was required to be equal by mass conservation; that is not the case here, however, because the BPE reduces the cross-sectional area of the channel above the electrode. Instead, the integral of the velocity over the height must be equal in each region, allowing for higher average flow speeds in the region above the BPE. In fact, the average axial velocity above the BPE is 50% higher than in other regions for a 300 nm tall channel with a 100 nm thick BPE. This effect is further exacerbated by the presence of induced-charge electroosmotic flow which accelerates the flow locally in certain regions (see Chapter IV for more details). Moreover, for early times during BPE charging the ionic current above the BPE is short-circuited by EDL charging, leading to a significantly reduced electric field strength above most of the BPE (Figure 3.5(a)). Hence, the region above the BPE is one such area of relatively low electric field and high flow speed.

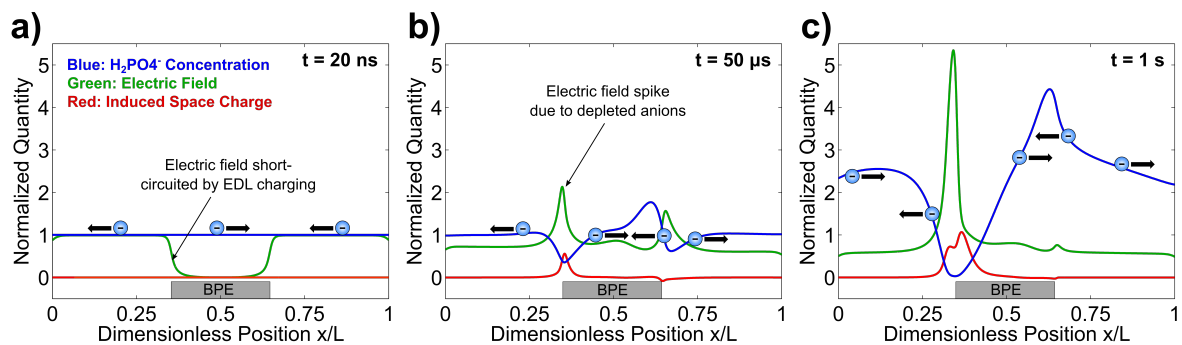


**Figure 3.5:** Formation of concentration polarization zones near the BPE edges: (a) at  $t = 20$  ns, the electric field above the BPE is reduced due to EDL charging; (b) at  $t = 50$   $\mu$ s, the initial formation of an electric field gradient due to anion focusing and depletion regions is evident; (c) at  $t = 1$  s, the steady state ion concentration profile along with the corresponding positive induced-charge layer and the spike in the electric field near the depletion zone are shown. All profiles are taken along the centerline of the channel at  $z = H/2$ .

The net effect of the reduced electric field and increased flow speed is that advection prevails over migration locally (i.e.  $0 < v_i^* < 1$ ) and anions above the BPE are transported downstream (left to right). By contrast, the electric field upstream and downstream of the BPE is sufficiently high to ensure upstream (right to left) transport of anions in these regions (i.e.  $v_i^* > 1$ ). Thus, focusing and depletion regions are formed near the cathode and anode, respectively, at the locations where the ion transport velocity changes sign; the ion depletion near the cathode reduces the local electrical conductivity of the solution by lowering the number of available charge carriers. Note that the ion transport velocity of cations does not change in this location, as both EOF and electromigration are directed downstream; thus, anions are selectively depleted and an induced-charge layer (ICL) of positive charge subsequently forms in the depletion zone and influences the potential distribution. Moreover, the local decrease in electrical conductivity due to ion depletion leads to an increase in the electric field magnitude.<sup>21,27</sup> As demonstrated in Chapter II, such electric field gradients can be leveraged for focusing and separation of analytes. Figure 3.5 illustrates how these CP

zones form for  $\text{H}_2\text{PO}_4^-$  anions, while Figure 3.6 demonstrates that simultaneous focusing and separation can be achieved upstream of the cathodic BPE pole for several monoanionic analytes of varying mobility.

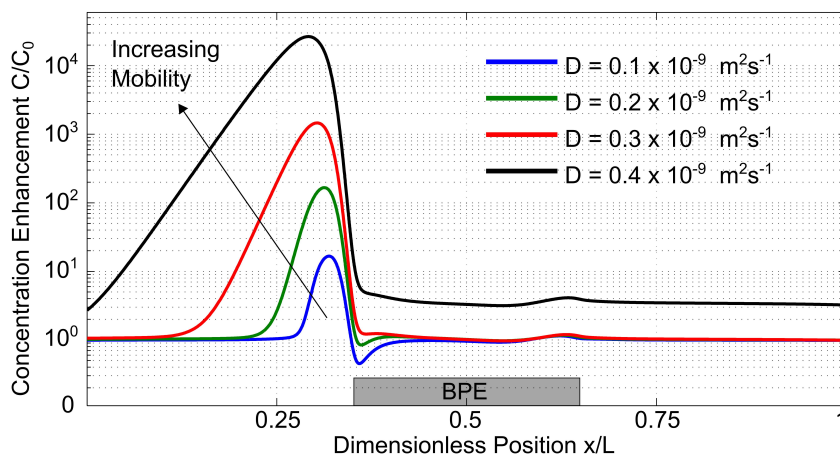


**Figure 3.6:** Simultaneous focusing and separation enabled by concentration polarization-induced electric field gradients. In a longer, more practical channel the field gradients would broaden and the enhancement profiles would be more easily distinguished from one another.<sup>27</sup>

#### 4. BPE Discharging Dynamics

The discharging dynamics of the confined BPE are fundamentally linked to the steady state conditions achieved during the application of a potential difference across the channel. Similar time scales to those discussed in Section 2 manifest during discharging but, more specifically, the electrochemical reactions and accompanying electrokinetic effects are dictated by the net charge accumulated on the electrode. As previously discussed, this is related to the relative rate of the cathodic and anodic reactions during the initial transient charging period, and should be distinguished from the charge due to electrostatic BPE polarization. This charge accumulation can be observed as a bias in the interfacial potential distribution towards one pole (Figure 3.7), and can be caused by asymmetry in the reaction

kinetics, charge transfer coefficients, and/or mass transfer conditions at the poles; this is loosely analogous to a Galvanic cell which acquires a net charge in order to reach the equilibrium potential required to balance the partial anodic and cathodic currents from a given reaction.<sup>17</sup>

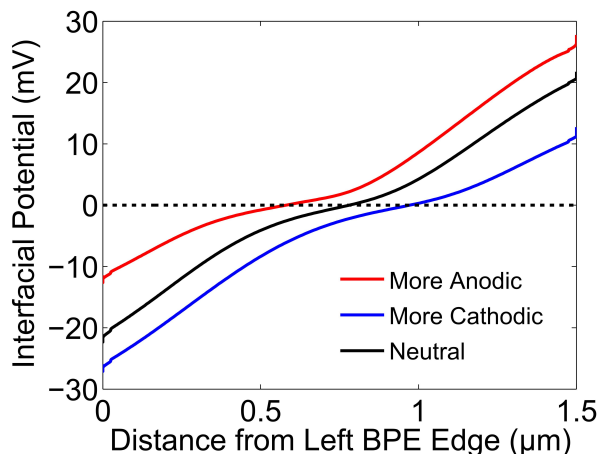


**Figure 3.7:** (a) Interfacial potential distributions along the BPE surface for the three different cases possible during charging: more anodic, more cathodic, and neutral. Note that the interfacial potential is proportional to local the surface charge.

The BPE steady state can be broadly classified into three categories: 1) a more anodic case in which a net positive charge has accumulated at the surface, 2) a more cathodic case in which a net negative charge has accumulated at the surface, and 3) a neutral case with no net charge accumulation; the electrokinetic transport as well as the chemical and electrochemical reactions which occur in solution after the applied potential is removed are qualitatively different for these three cases. To understand the origins of this behavior, we first revisit the polarization mechanism. Recall that BPE polarization arises due to a potential difference in solution between the ends of the BPE, which are ultimately surrounded by charged EDLs that maintain a potential difference between the diffuse layer and the bulk (i.e. the zeta potential). Also recall Gauss's Law, which dictates that in regions of nonzero space charge density, the

potential changes in response to the space charge; thus, if the applied potential is removed faster than the EDL space charge can respond, then the same effective zeta potential and EDL distribution as present in the steady state distributions still exist immediately after the removal of the applied potential. This is important because it follows that the potential difference between the BPE extremities also remains unchanged at the respective Stern layers. Therefore, the Faradaic reactions briefly continue to occur at the same rate even though the applied potential is now zero.

The reactions continue unabated well into the Debye time ( $\sim 10$  ns), in which only initial EDL relaxation occurs. It is not until the Ohmic time scale ( $\sim 10$   $\mu$ s) that we start to see appreciable drift-diffusion of ions in the EDL and a subsequent reduction in the surface charge distribution and Faradaic currents. This suggests that the electrode will remain polarized (i.e. bipolar) as long as the space charge in the EDLs still exists at the poles. As a result, the BPE cannot fully discharge during this period because there is still charge-transfer occurring at both poles; discharging requires that either the cathodic or anodic reactions proceeds at a relatively faster rate in order to preferentially deplete any accumulated charge. Therefore, even though the Ohmic and Faradaic time scales are similar in our simulations, Faradaic discharging is limited and delayed by EDL relaxation. Moreover, Faradaic discharge will also be affected by mass transport effects as gradients in electroactive species dissipate. Our calculations predict that the EDLs fully relax and the BPE loses its polarization around 10  $\mu$ s, as evidenced by the net charge present at the “weaker” pole (i.e. the anodic pole for the more cathodic case, and the cathodic pole for the more anodic case) going to zero around this time (Figure 3.8). That is, we integrate the surface charge for the anodic and cathodic poles separately over the BPE surface, and find that the entire surface charge distribution attains a single polarity around this time. Thus, any change in the charge

distribution prior to this time can be thought of primarily as the BPE losing the impetus for polarization due to EDL dissipation, while any change after this time can be attributed to conventional Galvanic discharge of accumulated charge.

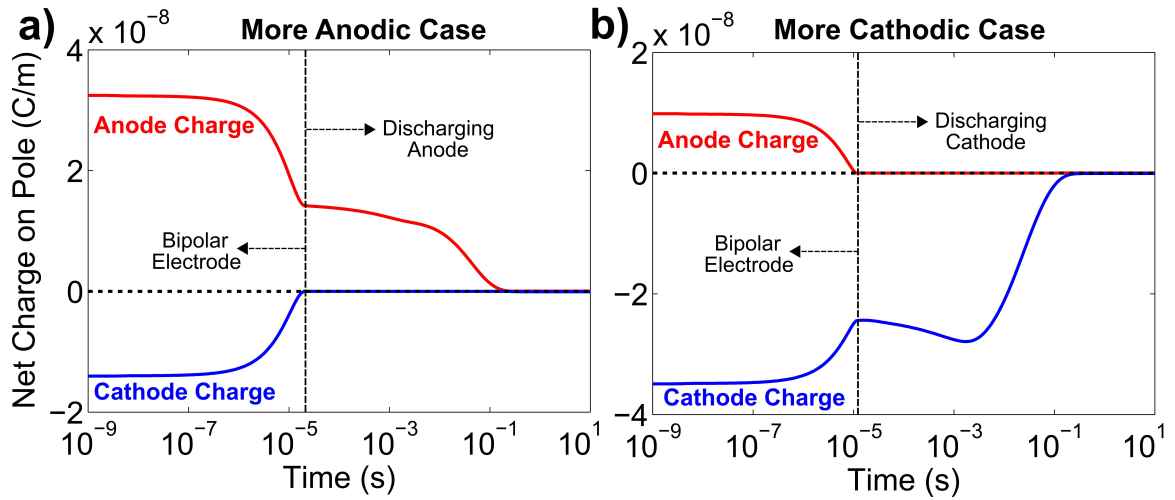


**Figure 3.8:** Net charge present (polarization + electrochemically accumulated charge) on (a) the anodic pole and (b) the cathodic pole during discharge. Results for both cases suggest that the BPE loses its polarization around  $10 \mu\text{s}$  and becomes either a discharging anode or cathode shortly thereafter.

The preferential anodic or cathodic discharge manifests as the BPE floating to either a positive or negative potential, respectively, during the Galvanic discharge period, as shown in Figure 3.9. Note that the fluid potential away from the BPE has reached zero by this point, thus reinforcing the notion that the BPE eventually acts as either a cathode or anode with a uniform driving potential of single polarity. The BPE potential floats to negative values at very early times for each case because the potential drop upstream of the cathode associated with CP-induced ion depletion biases  $V_{\text{elec}}$  to lower potentials before the EDLs can relax and the accumulated surface charge prevails. More specifically, the negative potential that the BPE initially reaches is roughly equal to the difference between the steady state BPE

potential and the expected potential at the middle of the channel for a case without any spatial conductivity variations (i.e.  $V_{\text{applied}}/2$ ). As such, this deviation can be considered a rough measure of the steady state deviation from a reaction-symmetric equilibrium condition.

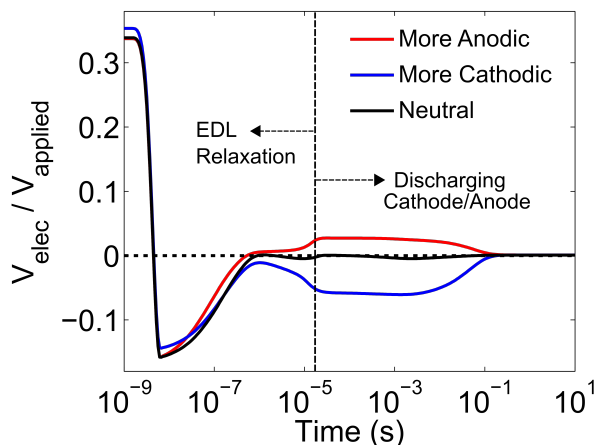


**Figure 3.9:** Floating BPE potential during discharging, which demonstrates how the BPE eventually floats to a positive value in the anodic case and a negative value in the cathodic case to shed the accumulated charge before reaching equilibrium.

EDL relaxation occurs by a process of drift-diffusion, in which strong electric fields are generated by the space charge imbalances in the EDLs above the BPE once the applied potential is removed. These imbalances polarize the solvent, thereby attracting ions of opposite sign to the region to neutralize the charge imbalance and restore electroneutrality; diffusion also aids in forcing these ions towards the surface due to the concentration gradients established by electrostatically depleted co-ion concentrations in the EDL. Thus, the cation-rich EDL above the cathode will experience a large influx of anions on the Ohmic time scale as the EDLs dissipate. This can be visualized through fluorescence measurements of FL, and is demonstrated experimentally and numerically in Figure 3.10. Specifically, we observe in our experiments that over the course of approximately 0.5 s, the FL intensity above the cathode transitions from relatively low intensity to relatively high intensity. We

note again that this time scale differs from that in our simulation due to disparities in experimental vs. modeled length scales, as well as practical limitations on how quickly the applied potential can experimentally be removed by the power supply.

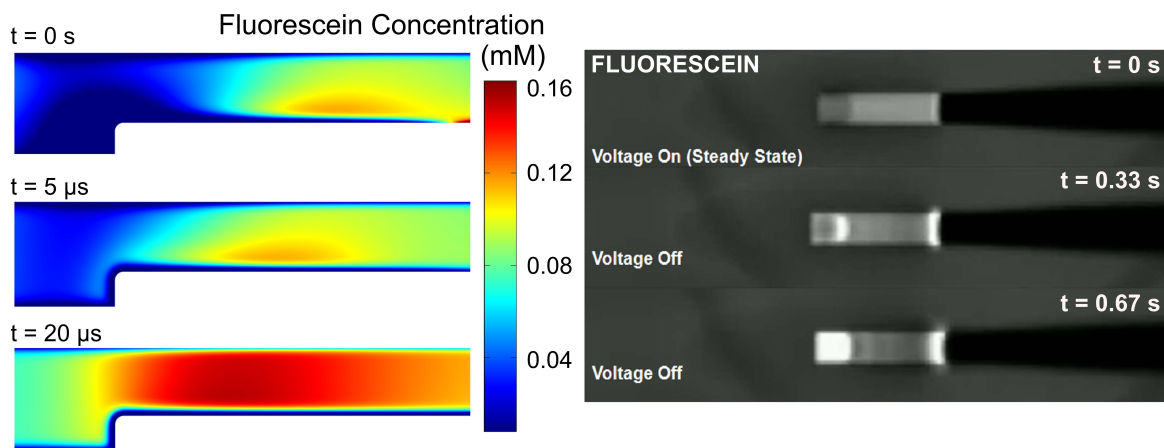


**Figure 3.10:** Fluorescein redistribution by drift-diffusion manifests as a rapid increase in concentration at the cathode due to the large influx of anions required to neutralize the space charge imbalance from the dissipating cathodic EDL. Note that no noticeable FL quenching is expected near the cathode during the EDL relaxation time, as this region contains a relatively high pH.

Faradaic reactions must necessarily accompany discharging, as interfacial charge transfer is the only mechanism by which a net accumulated charge can be shed from the electrode. Predictably, the more anodic case is characterized by oxidation reactions and the more cathodic case is characterized by reduction reactions which drive the discharge process. Thus, we can expect that the electrokinetics and chemical reactions associated with the redox-active ions produced by these discharging reactions will be qualitatively different for the two cases. That is, the oxidation reactions will produce  $O_2$  and  $H^+$  (resulting in a drop in the local pH) and the reduction reactions will produce  $H_2$  and  $OH^-$  (resulting in a local pH rise). Figure 3.11 demonstrates these pH shifts during the discharge reactions, indicating that the pH rapidly changes at both poles starting around  $10 \mu s$ , corresponding to the simulated time at which the BPE transitions to Galvanic discharge. As suggested by Figure 3.11, these

discharging reactions and subsequent pH changes should manifest at both poles, such that the entire spatial region near the BPE is eventually acidic for the more anodic case, alkaline for the more cathodic case, and near the bulk pH for the neutral case. However, we will show in the next section that this is not in accordance with experimental observations, as electrochemical modification of the surface while the applied potential is on noticeably affects the discharging dynamics.

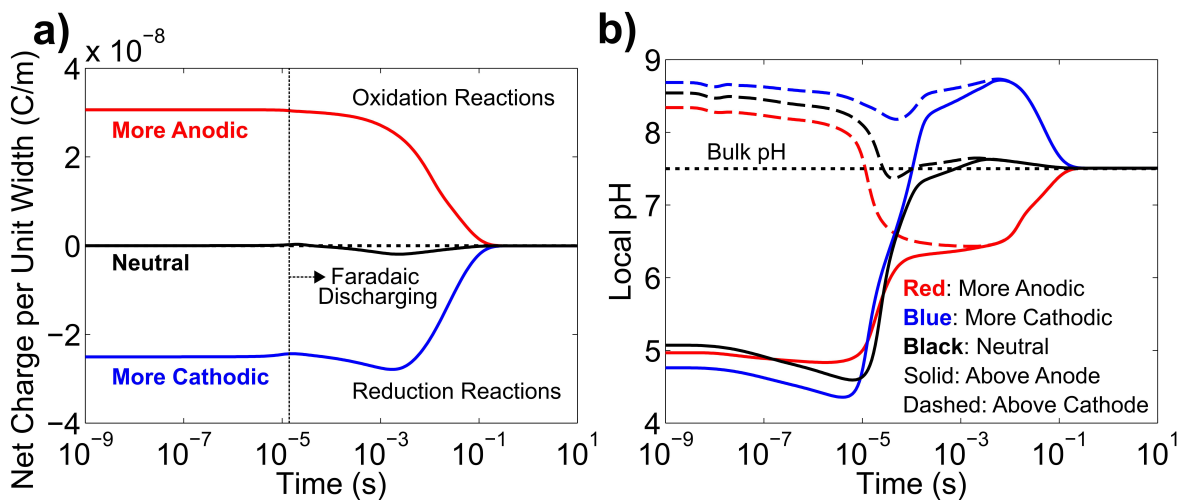


**Figure 3.11:** (a) Net accumulated BPE charge present during discharge and (b) local pH outside the EDL near both the cathode and anode for all three cases. These results indicate that there are significant oxidation (more anodic case) and reduction (more cathodic case) reactions that must take place for the BPE to fully discharge; these reactions are accompanied by the production of  $H^+$  or  $OH^-$  ions, respectively, and subsequently influence the local pH near the electrode.

Figure 3.12 below depicts the spatiotemporal evolution of electric field lines around the BPE during the charging and discharging phases. These results demonstrate several of the charging and discharging effects discussed heretofore, including currents short-circuited by EDL charging, a bias in the interfacial potential distribution, the loss of BPE polarization, and ultimately the formation of a secondary EDL to screen the accumulated charge during the Galvanic discharge period. Note that EDL relaxation is accompanied by a reversal in the electric field upstream and downstream of the BPE. This behavior is caused by a potential

difference between the ends of the BPE and the respective reservoirs, and is linked to the electrokinetics which serve to neutralize the space charge imbalance during EDL relaxation. That is, the potential in the left and right reservoirs is effectively zero after the rapid removal of the applied potential, but there still remains a positive electrostatic potential associated with the cathodic EDL space charge and a negative potential associated with the anodic EDL space charge above the BPE. Thus, a positive potential gradient (i.e. negative axial electric field) is established upstream of the cathode, a negative potential gradient (i.e. positive axial electric field) is established between the cathodic and anodic poles, and a positive potential gradient (i.e. negative axial electric field) is established downstream of the anode as the EDLs relax by drift-diffusion.

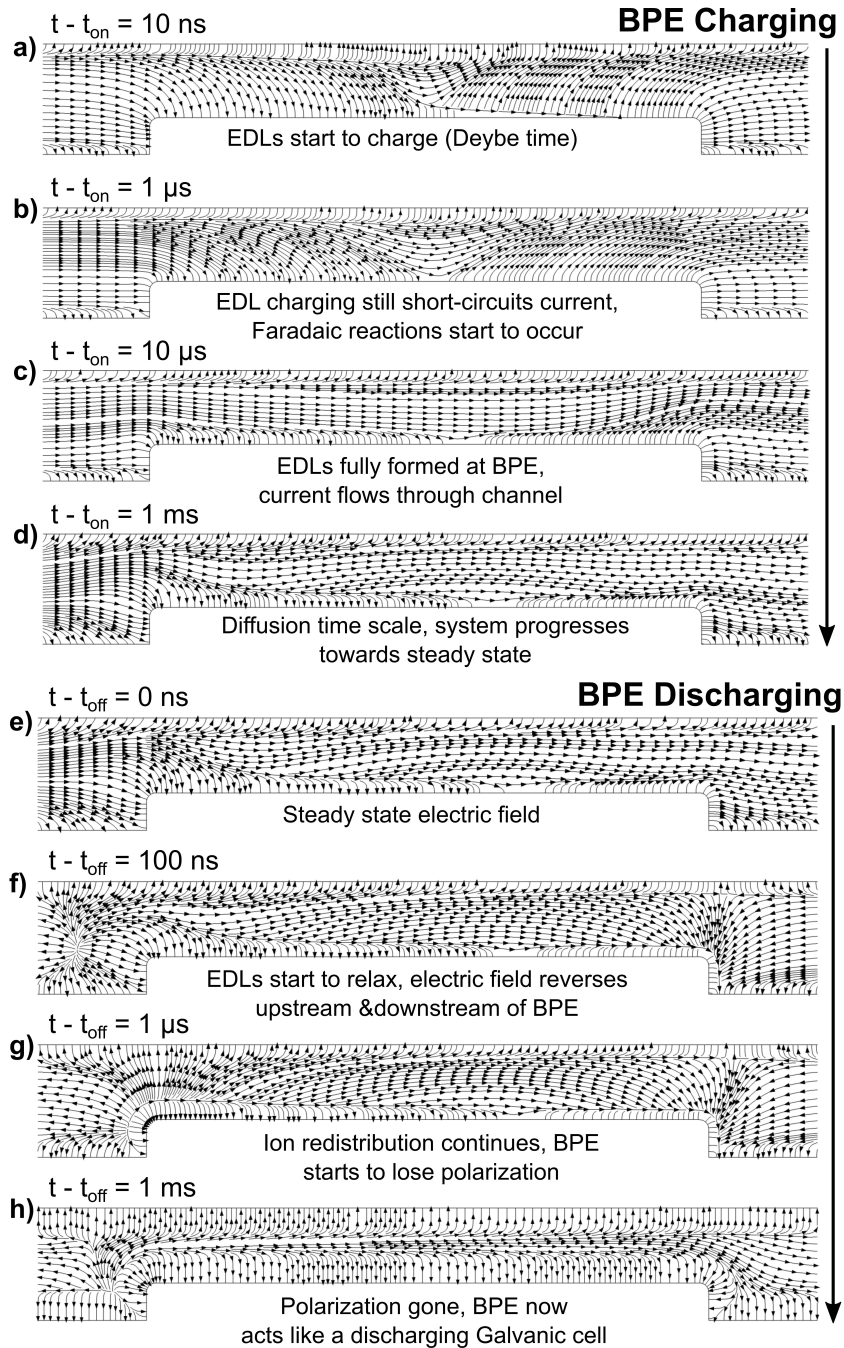


**Figure 3.12:** Spatiotemporal evolution of the electric field lines near the BPE during the charging and discharging processes.

## 5. Effect of Oxide Growth on BPE

The numerical results from the preceding sections have neglected the presence of surface oxides on the bipolar electrode. In practice, however, platinum electrodes are known to be

susceptible to oxidation after sustained reactions at anodes.<sup>39</sup> We can qualitatively account for the effects of the surface oxide film on the electrokinetic and electrochemical dynamics of our system by approximating some portion of the oxygen evolution current density as contributing to the formation and growth of platinum oxide on the surface. That is, we assume that the oxide growth rate is proportional to the local oxidation current from the OER,

$$\frac{\partial h_{\text{film}}}{\partial t} = \phi j_{\text{O}_2} \quad (3.15)$$

where  $h_{\text{film}}$  is the local film thickness,  $\phi$  is a proportionality constant that relates the charge transfer rate to the oxide growth rate. We assume an arbitrary value of  $1 \times 10^{-11} \text{ m}^3/\text{C}$  for the proportionality constant, as we only expect to obtain qualitative results from our model. The oxide film accordingly develops and grows thickest at the extremity of the anodic pole (Figure 3.13(a)), while the thickness is equal to zero for the entire anodic pole. This film acts as a resistive layer which serves to decrease the local interfacial potential difference between the BPE and the diffuse layer of the electrolyte solution. Thus, the interfacial potential difference now includes an additional Ohmic potential drop  $V_{\text{film}} = j_{\text{net}} R_{\text{film}}$ , where  $V_{\text{film}}$  is the potential drop across the film, and  $R_{\text{film}}$  is the surface film resistance, given by  $R_{\text{film}} = h_{\text{film}}/\sigma_{\text{film}}$  (for the purposes of this qualitative simulation we assume the conductivity of the film  $\sigma_{\text{film}}$  to be equal to  $1 \times 10^{-6} \text{ S/m}$ ). The local interfacial potential difference implemented in the surface charge and gFBV boundary conditions now changes from  $V_{\text{elec}} - \psi$  to  $V_{\text{elec}} - \psi - V_{\text{film}}$ . Note that the film thickness and potential drop are fixed to zero in locations where no net oxidation has occurred (i.e. the cathodic pole).

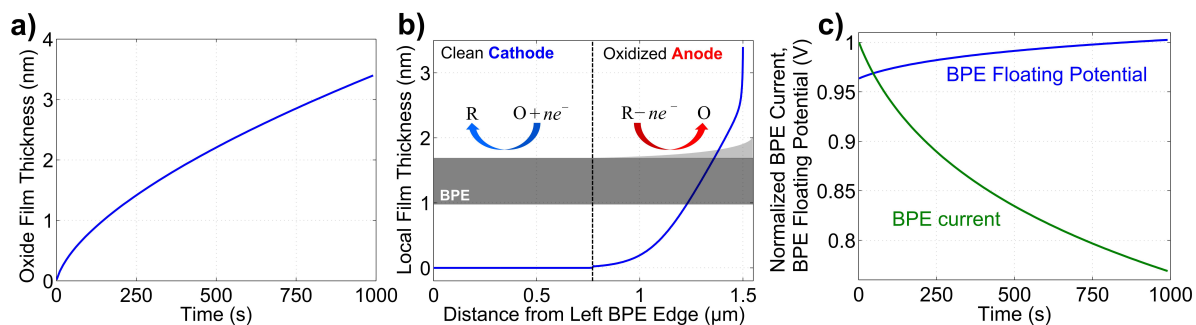


**Figure 3.13:** (a) Simulation of oxide film growth at the extremity of the anodic pole, (b) local oxide profile along the BPE surface after 1000 s of reactions, and (c) shift in the BPE floating potential towards the cathodic pole to compensate for the resistive oxide film growth; this shift serves to increase the anodic interfacial potential and decrease the cathodic interfacial potential.

The reactions at the cathodic and anodic poles of the electrode are coupled, much like those of a working and counter electrode in a conventional electrochemical system. Therefore, as oxide growth hinders the reactions at the anodic pole, the cathodic reactions must slow to compensate and maintain a balanced current to prevent infinite charge accumulation. This effect manifests as a shift in the BPE floating potential to higher values over time, so as to decrease the magnitude of the interfacial potential difference at the cathode and counteract the decrease in the effective driving potential at the anode from the increasing Ohmic potential drop. The faradaic current passing through the BPE therefore decreases over time due to the decrease in driving potential at both poles (Figure 3.13c).

As previously alluded to, the presence of a resistive film on the BPE surface also affects the discharging dynamics and the coupled electrokinetic events that accompany discharging. In particular, we observed events which suggest that, contrary to Figure 3.11, the pH does not drop or rise uniformly around the BPE during discharge. Instead, shortly after the cathodic fluorescein intensity rise associated with EDL relaxation, rapid and intense quenching linked to water oxidation products is observed locally only above the left pole (Figure 3.14). This localization can be attributed to the presence of the anodic oxide film,

which hinders discharging reactions at the right pole and causes the Galvanic discharge to occur more rapidly at the oxide-free left pole where the interfacial resistance is lower. We probed this behavior by utilizing a split BPE configuration,<sup>30,51</sup> which allowed for the two poles to be individually addressed and electrochemically pretreated separately. After pretreating the left pole via oxidation, the two poles were then electrically connected to each other and subsequently served as a BPE when an electric field was introduced in solution. Figure 3.14 shows that the pretreated BPE prevents localized discharging-linked quenching from occurring in the same manner as observed with an untreated BPE, confirming that the presence of the oxide film plays an important role in determining local discharging rates.

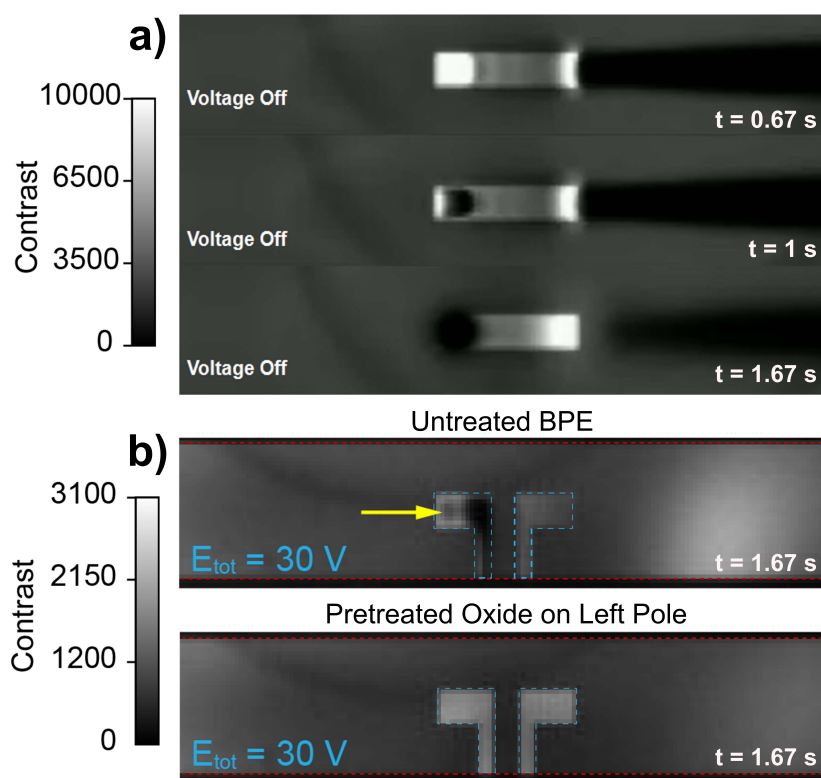


**Figure 3.14:** Depiction of localized fluorescence quenching associated with water oxidation products during anodic discharge: (a) the presence of the anodic oxide film increases the local interfacial resistance, causing the discharging to preferentially occur at the left pole; (b) pretreatment of the left pole suppresses the localized quenching

## 6. Deducing Information About Chemical Kinetics Through Simulation

There is a glaring lack of information in previous literature about the chemical kinetics of certain buffer protonation reactions, including the ubiquitous triprotic phosphate buffer system employed in this study. Simulation can potentially help to fill this void by providing unprecedented insight into the effect of homogeneous reactions on measurable electrochemical system conditions such as reaction currents, local pH, and electroosmotic pumping rates. This is true not only for the study of reactions directly coupled to electron transfer events,<sup>21</sup> but also for buffer reactions often ignored or oversimplified in many numerical studies of bipolar electrochemistry. The use of limiting currents to deduce information about chemical kinetics based on knowledge of Faradaic reaction rates has previously been proposed in the literature,<sup>18,52</sup> but it is difficult to quantify the effect of spatially nonuniform, dynamically variable properties such as electroosmotic flow and electric field gradients on true limiting currents in a confined BPE system which can deviate significantly from electroneutrality. Simulation provides an advantage here by allowing for a more tractable computational environment with the inclusion of as many (or as few) physical effects as desired. Furthermore, parametric studies can quickly and easily be implemented to quantify the sensitivity of results to a wide range of unknown or uncertain parameter values, enabling researchers to elucidate the nontrivial relationships between chemical, electrochemical, and electrokinetic phenomena.

In developing our model, we extensively searched the literature for previously reported protonation rates for phosphate buffer systems. However, we found only one study in which the proton dissociation rate of  $\text{H}_3\text{PO}_4$  was reported, with a value of  $k_{t,1} = 3.8 \times 10^8 \text{ s}^{-1}$  measured via ultrasonic absorption.<sup>53</sup> We used this value to determine the corresponding protonation

rate constant  $k_{r,1}$  via the equilibrium constant  $K = k_f / k_r$ , the values for which are readily available in the literature (see Table 3.7). Thus, we were left with two unknown protonation/deprotonation rate constants: one for  $\text{H}_2\text{PO}_4^-$  and another for  $\text{HPO}_4^{2-}$ . In this section, we assume that protonation reactions involving these species are slower than that of water,  $k_{r,w} = 1.4 \times 10^{11} \text{M}^{-1}\text{s}^{-1}$ , and subsequently examine how these unknown rate constants influence the predicted steady-state axial electric field, velocity, and pH distribution along the channel centerline. Note that all of the following observations were made assuming fixed equilibrium constants, and by varying only the protonation rates for monohydrogen and dihydrogen phosphate.

Predictably, the rate constants for each of the triprotic phosphate buffer reactions significantly affect the buffering capacity of the electrolyte. Figure 3.15(a) reveals that protonation rate constants slower than  $\sim 10^6 \text{M}^{-1}\text{s}^{-1}$  effectively cause the electrolyte to behave as an unbuffered solution. By contrast, progressively increasing the unknown rates yields a substantial buffering effect that is maximized when the unknown protonation rate constants are equal to  $k_{r,w}$ . Through analysis of the centerline pH profiles, we find that the broadening of pH gradients is fundamentally linked to the simulated reaction rates. For example, assuming protonation rate constants of  $\sim 10^9 \text{M}^{-1}\text{s}^{-1}$  leads to a low-pH gradient adjacent to the BPE anode that extends through the full length of the channel and disappears some distance into the microscale reservoir. Increasing the rate to  $\sim 10^{11} \text{M}^{-1}\text{s}^{-1}$  causes rapid neutralization of the pH over short distances, considerably reducing the extent of the predicted pH gradient. The effect of buffering on the pH gradient will naturally depend on system size, as several of the profiles in Figures 3.15(a) and 3.15(b) show a non-neutral pH region that extends into the reservoirs. This manner of analysis raises the possibility to parametrically adjust dissociation

rates to fit experimentally-determined pH gradients (e.g., via pH sensitive fluorophores) modulated by an applied voltage, enabling the determination of chemical kinetics without the need for difficult, instrument-intensive measurements such as ultrasonic absorption or nuclear magnetic resonance.<sup>53,54</sup>

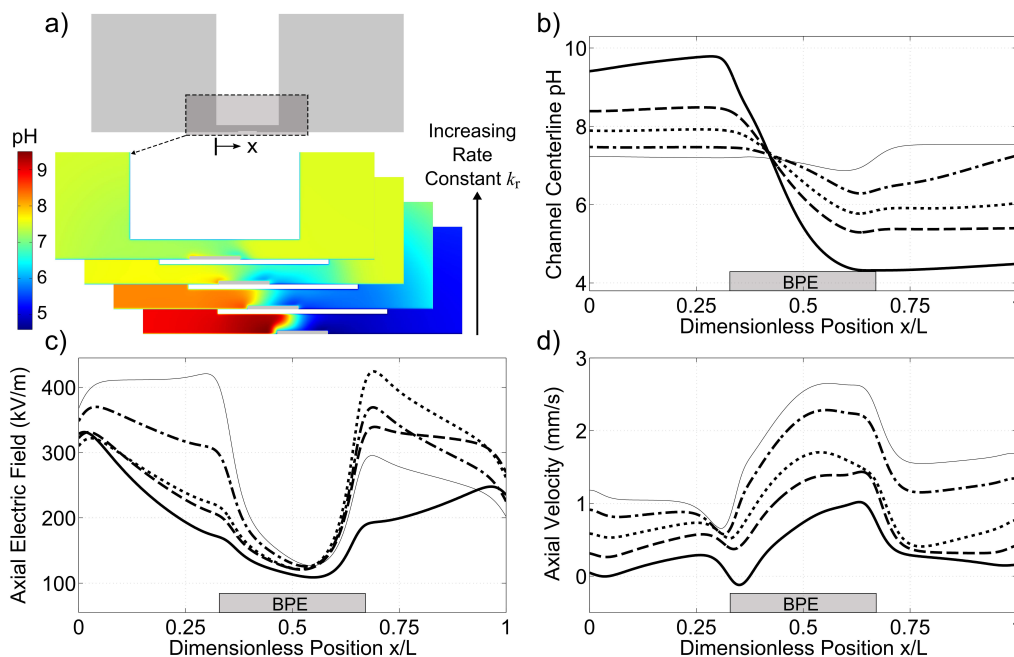


**Figure 3.15:** (a) Effect of phosphate buffer dissociation/association rate constants on predicted pH profiles in our shorter channel simulations for a 600 nm tall channel with a 0.1 mM phosphate buffer, (b) 1D pH profiles in the channel at  $z = H/2$ , (c) 1D axial electric field distribution in the channel at  $z = H/2$ , and (d) the local axial electroosmotic flow profile in the channel at  $z = H/2$ . The curves in (b)-(d) correspond to  $k_r = 1 \times 10^6 \text{ M}^{-1}\text{s}^{-1}$  (thick solid line),  $k_r = 7.5 \times 10^8 \text{ M}^{-1}\text{s}^{-1}$  (dashed line),  $k_r = 2.5 \times 10^9 \text{ M}^{-1}\text{s}^{-1}$  (dotted line),  $k_r = 1 \times 10^{10} \text{ M}^{-1}\text{s}^{-1}$  (dash-dot line), and  $k_r = k_{r,w} = 1.4 \times 10^{11} \text{ M}^{-1}\text{s}^{-1}$  (thin solid line).

The buffer reaction rates also directly affect the magnitude and distribution of the electric field along the axis of the channel, as the contribution to the electrical conductivity of each reacting species varies due to differences in valence and ionic mobility. At the low rate constant limit of  $10^6 \text{ M}^{-1}\text{s}^{-1}$ , the local field maxima occur near the channel inlet and outlet (Figure 3.15(c)). By increasing the magnitude of these rates, we observe a progressive

change in the electric field distribution, with the local maxima of the axial field shifting closer to the poles of the BPE. Accordingly, our simulations predict that varying the magnitude of proton dissociation rates can produce greater than a 100% change in the maximum magnitude of the electric field near the BPE poles. Because the simulated rates affect these local field gradients, they also directly influence the Coulombic forces and resulting electroosmotic velocity profile throughout the channel. In particular, the various centerline flow profiles in Figure 3.15(d) correspond to a factor of three increase in the local flow velocity as the reaction rate constants are gradually increased from  $10^6$  to  $10^{11} \text{ M}^{-1}\text{s}^{-1}$ .

### *F. Conclusion*

In this chapter, we demonstrated the use of a detailed 2D finite-element numerical model to simulate electrochemical reactions and electrokinetic transport of chemical species in a confined BPE system. Our model is the first to show in microscopic detail the complex transport and reaction mechanisms at the surface of a BPE as it becomes polarized and heterogeneous charge transfer proceeds simultaneously at both poles. We employ generalized Frumkin-Butler-Volmer kinetics to describe charge transfer across the theoretical Stern layer reaction plane, while also accounting for charge-screening effects in the diffuse layer by allowing for deviations from the traditional macroscopic assumption of bulk electroneutrality.

Fluorescence experiments were used to demonstrate the formation of an extended low pH region that develops and propagates downstream of the anodic pole due to rapid  $\text{H}^+$  production and  $\text{OH}^-$  consumption rates at our Pt BPE. Numerical calculations were shown to reproduce this effect once fluorescence intensity quenching by fluorescein protonation was empirically accounted for. Additionally, our model confirms that observed regions of locally depleted and enhanced intensity at the cathodic and anodic poles, respectively, are due to

electrostatic interactions with the polarized BPE. We found that these interactions and the dynamics of the BPE are altered by the growth of a resistive oxide film on the electrode, which can be qualitatively accounted for in the model. The effect of homogeneous buffer reaction kinetics on the predicted spatial pH distribution was briefly examined, and we found that simulation can potentially be a useful tool to estimate unknown parameters through an inverse optimization curve-fitting approach as an alternative to complex and time-consuming experimental methods. The model presented herein therefore provides an important first step towards further understanding the interplay between the intrinsically coupled polarization effects, Faradaic charge transfer, chemical reactions, and nonlinear transport phenomena encountered in confined bipolar electrochemistry.

### *G. Additional Simulation Details*

The reversible buffer and water reactions from equations (3.6)-(3.9) can be described by four reaction rate terms. For these forward and reverse reactions, we have the following reaction rates:

$$r_{\text{H}_3\text{PO}_4} = k_{f,1}c_{\text{H}_3\text{PO}_4} - k_{r,1}c_{\text{H}_2\text{PO}_4^-}c_{\text{H}^+}; \quad (3.16)$$

$$r_{\text{H}_2\text{PO}_4^-} = k_{f,2}c_{\text{H}_2\text{PO}_4^-} - k_{r,2}c_{\text{HPO}_4^{2-}}c_{\text{H}^+}; \quad (3.17)$$

$$r_{\text{HPO}_4^{2-}} = k_{f,3}c_{\text{HPO}_4^{2-}} - k_{r,3}c_{\text{PO}_4^{3-}}c_{\text{H}^+}; \quad (3.18)$$

$$r_{\text{H}_2\text{O}} = k_{f,w}c_{w,\infty} - k_{r,w}c_{\text{H}^+}c_{\text{OH}^-}; \quad (3.19)$$

where water assumed to be in excess at a concentration of  $c_{w,\infty} = 55.5 \text{ M}$ .<sup>55</sup> Table S1 below shows how these rates are combined to formulate reaction source terms  $R_i$  corresponding to equation (3.5).

**Table 3.3:** Homogeneous reaction source terms for the buffer reactions and autodissociation of water.

Species	Reaction Source Term $R_i$
$\text{H}_3\text{PO}_4$	$R_{\text{H}_3\text{PO}_4} = -r_{\text{H}_3\text{PO}_4}$
$\text{H}_2\text{PO}_4^-$	$R_{\text{H}_2\text{PO}_4^-} = r_{\text{H}_3\text{PO}_4} - r_{\text{H}_2\text{PO}_4^-}$
$\text{HPO}_4^{2-}$	$R_{\text{HPO}_4^{2-}} = r_{\text{H}_2\text{PO}_4^-} - r_{\text{HPO}_4^{2-}}$
$\text{PO}_4^{3-}$	$R_{\text{PO}_4^{3-}} = r_{\text{HPO}_4^{2-}}$
$\text{H}^+$	$R_{\text{H}^+} = r_{\text{H}_3\text{PO}_4} + r_{\text{H}_2\text{PO}_4^-} + r_{\text{HPO}_4^{2-}} + r_{\text{H}_2\text{O}}$
$\text{OH}^-$	$R_{\text{OH}^-} = r_{\text{H}_2\text{O}}$
$\text{Na}^+$	0
$\text{FL}^{2-}$	0
$\text{H}_2$	0
$\text{O}_2$	0

As previously alluded to, we implement a pH-dependent formulation of the Faradaic reactions to mechanistically account for shifts in the dominant reactions as the surrounding fluid composition changes over time.<sup>56</sup> That is, we assume that the reactions are “fully acidic” (i.e. only reactions  $2\text{H}^+ + 2e^- \rightleftharpoons \text{H}_2$  and  $4\text{H}^+ + \text{O}_2 + 4e^- \rightleftharpoons 2\text{H}_2\text{O}$  can occur locally) below  $\text{pH} = 4$  and “fully alkaline” (i.e. only reactions  $2\text{H}_2\text{O} + 2e^- \rightleftharpoons \text{H}_2 + 2\text{OH}^-$  and

$2\text{H}_2\text{O} + \text{O}_2 + 4e^- \rightleftharpoons 4\text{OH}^-$  occur locally) above  $\text{pH} = 10$ . Between these extremes, there is a combination of all four of the above reactions occurring. This is realized by scaling the effective cathodic and anodic rate constants from equation (3.12) by a pH-dependent error function that is evaluated by probing the local pH outside the cathodic and anodic EDLs, respectively. Thus, we have scaling functions  $f_{\text{acid}}$  and  $f_{\text{alk}}$  that are evaluated at two different locations,  $\text{pH}_c$  and  $\text{pH}_a$ , giving four possible scaling terms to multiply the respective rate constants by. For reduction half-reaction terms, the cathodic rate constant is multiplied by the appropriate scaling function evaluated using the cathodic pH, while the scaling function for each oxidation half-reaction term is evaluated using the anodic pH.

See Table 3.4 below for the formulation of each Faradaic reaction boundary term. Note that, for simplicity, we assume the cathodic rate constants for each acidic and alkaline reaction, respectively, are related to an exchange current density  $j_0$  and the bulk concentration of redox species via  $K_c = f_{\text{acid}}(\text{pH}_c) j_0 / c_{\text{ox},\infty}$  and  $K_c = f_{\text{alk}}(\text{pH}_c) j_0 / c_{\text{ox},\infty}$ . The anodic rate constants are similarly related to the exchange current density via  $K_a = f_{\text{acid}}(\text{pH}_a) j_0 / c_{\text{red},\infty}$  and  $K_a = f_{\text{alk}}(\text{pH}_a) j_0 / c_{\text{red},\infty}$ .

**Table 3.4:** Concentration-dependent and pH-dependent Frumkin-Butler-Volmer Faradaic reaction boundary terms.

Reaction	Equation	Reaction Current Density
HER (acidic)	$2\text{H}^+ + 2e^- \longrightarrow \text{H}_2$	$j_{\text{c,H}_2,\text{acid}} = j_{0,\text{H}_2,\text{acid}} f_{\text{acid}}(\text{pH}_c) \frac{c_{\text{H}^+}}{c_{\text{H}^+,\infty}} \exp\left[-\frac{\alpha_{\text{c,H}_2} n_{\text{H}_2} F (V_{\text{elec}} - \psi)}{RT}\right]$
ORR (acidic)	$4\text{H}^+ + \text{O}_2 + 4e^- \longrightarrow 2\text{H}_2\text{O}$	$j_{\text{c,O}_2,\text{acid}} = j_{0,\text{O}_2,\text{acid}} f_{\text{acid}}(\text{pH}_c) \frac{c_{\text{H}^+}}{c_{\text{H}^+,\infty}} \frac{c_{\text{O}_2}}{c_{\text{O}_2,\infty}} \exp\left[-\frac{\alpha_{\text{c,O}_2} n_{\text{O}_2} F (V_{\text{elec}} - \psi)}{RT}\right]$
HER (alkaline)	$2\text{H}_2\text{O} + 2e^- \longrightarrow \text{H}_2 + 2\text{OH}^-$	$j_{\text{c,H}_2,\text{alk}} = j_{0,\text{H}_2,\text{alk}} f_{\text{alk}}(\text{pH}_c) \exp\left[-\frac{\alpha_{\text{c,H}_2} n_{\text{H}_2} F (V_{\text{elec}} - \psi)}{RT}\right]$
ORR (alkaline)	$2\text{H}_2\text{O} + \text{O}_2 + 4e^- \longrightarrow 4\text{OH}^-$	$j_{\text{c,O}_2,\text{alk}} = j_{0,\text{O}_2,\text{alk}} f_{\text{alk}}(\text{pH}_c) \frac{c_{\text{O}_2}}{c_{\text{O}_2,\infty}} \exp\left[-\frac{\alpha_{\text{c,O}_2} n_{\text{O}_2} F (V_{\text{elec}} - \psi)}{RT}\right]$
HOR (acidic)	$\text{H}_2 \longrightarrow 2\text{H}^+ + 2e^-$	$j_{\text{a,H}_2,\text{acid}} = j_{0,\text{H}_2,\text{acid}} f_{\text{acid}}(\text{pH}_a) \frac{c_{\text{H}_2}}{c_{\text{H}_2,\infty}} \exp\left[\frac{\alpha_{\text{a,H}_2} n_{\text{H}_2} F (V_{\text{elec}} - \psi)}{RT}\right]$
OER (acidic)	$2\text{H}_2\text{O} \longrightarrow 4\text{H}^+ + \text{O}_2 + 4e^-$	$j_{\text{a,O}_2,\text{acid}} = j_{0,\text{O}_2,\text{acid}} f_{\text{acid}}(\text{pH}_a) \exp\left[\frac{\alpha_{\text{a,O}_2} n_{\text{O}_2} F (V_{\text{elec}} - \psi)}{RT}\right]$
HOR (alkaline)	$\text{H}_2 + 2\text{OH}^- \longrightarrow 2\text{H}_2\text{O} + 2e^-$	$j_{\text{a,H}_2,\text{alk}} = j_{0,\text{H}_2,\text{alk}} f_{\text{alk}}(\text{pH}_a) \frac{c_{\text{H}_2}}{c_{\text{H}_2,\infty}} \frac{c_{\text{OH}^-}}{c_{\text{OH}^+,\infty}} \exp\left[\frac{\alpha_{\text{a,H}_2} n_{\text{H}_2} F (V_{\text{elec}} - \psi)}{RT}\right]$
OER (alkaline)	$4\text{OH}^- \longrightarrow 2\text{H}_2\text{O} + \text{O}_2 + 4e^-$	$j_{\text{a,O}_2,\text{alk}} = j_{0,\text{O}_2,\text{alk}} f_{\text{alk}}(\text{pH}_a) \frac{c_{\text{OH}^-}}{c_{\text{OH}^+,\infty}} \exp\left[\frac{\alpha_{\text{a,O}_2} n_{\text{O}_2} F (V_{\text{elec}} - \psi)}{RT}\right]$

**Table 3.5:** Bulk concentration values as calculated by the sodium phosphate buffer nominal concentration, the bulk pH, and electroneutrality.

Species	Bulk Concentration (mM),	
	1.0 mM Phosphate Buffer	0.1 mM Phosphate Buffer
H <sub>3</sub> PO <sub>4</sub>	1.514 x 10 <sup>-6</sup>	1.514 x 10 <sup>-7</sup>
H <sub>2</sub> PO <sub>4</sub> <sup>-</sup>	0.339	0.0339
HPO <sub>4</sub> <sup>2-</sup>	0.661	0.0661
PO <sub>4</sub> <sup>3-</sup>	9.777 x 10 <sup>-6</sup>	9.777 x 10 <sup>-7</sup>
Na <sup>+</sup>	1.861	0.366
FL <sup>2-</sup>	0.1	0.1
Dissolved H <sub>2</sub>	1 x 10 <sup>-5</sup>	1 x 10 <sup>-5</sup>
Dissolved O <sub>2</sub>	1.3	1.3
H <sup>+</sup>	3.162 x 10 <sup>-5</sup>	3.162 x 10 <sup>-5</sup>
OH <sup>-</sup>	3.162 x 10 <sup>-4</sup>	3.162 x 10 <sup>-4</sup>

**Table 3.6:** Diffusion coefficients for each of the simulated species.

Species	Diffusion Coefficient (m <sup>2</sup> s <sup>-1</sup> )	Reference
H <sup>+</sup>	9.31 x 10 <sup>-9</sup>	57
OH <sup>-</sup>	5.6 x 10 <sup>-9</sup>	58
Dissolved H <sub>2</sub>	4.4 x 10 <sup>-9</sup>	59
Dissolved O <sub>2</sub>	2.3 x 10 <sup>-9</sup>	59
H <sub>3</sub> PO <sub>4</sub>	9.6 x 10 <sup>-10</sup>	58
H <sub>2</sub> PO <sub>4</sub> <sup>-</sup>	8.5 x 10 <sup>-10</sup>	60
HPO <sub>4</sub> <sup>2-</sup>	6.9 x 10 <sup>-10</sup>	60
PO <sub>4</sub> <sup>3-</sup>	6.1 x 10 <sup>-10</sup>	60
Na <sup>+</sup>	1.33 x 10 <sup>-9</sup>	58
FL <sup>2-</sup>	9.3 x 10 <sup>-10</sup>	61

**Table 3.7:** pKa values and associated rate constants.

Parameter	Value	Reference
pKa for H <sub>3</sub> PO <sub>4</sub> Dissociation	2.15	62
H <sub>3</sub> PO <sub>4</sub> Dissociation Rate Constant	3.8 x 10 <sup>8</sup> s <sup>-1</sup>	63
pKa for H <sub>2</sub> PO <sub>4</sub> Dissociation	7.21	62
H <sub>2</sub> PO <sub>4</sub> <sup>-</sup> Dissociation Rate Constant	81.2 s <sup>-1</sup>	----
pKa for HPO <sub>4</sub> Dissociation	12.33	62
HPO <sub>4</sub> <sup>2-</sup> Dissociation Rate Constant	6.3 x 10 <sup>-5</sup> s <sup>-1</sup>	----
pKa for H <sub>2</sub> O Dissociation	14	55
H <sub>2</sub> O Dissociation Rate Constant	2.522 x 10 <sup>-5</sup> s <sup>-1</sup>	55

**Table 3.8:** Faradaic reaction kinetics parameters.

Parameter	Value	Reference
HER/HOR Acidic Exchange Current Density	100 A/m <sup>2</sup> <sup>a</sup>	---
HER/HOR Alkaline Exchange Current Density	50 A/m <sup>2</sup> <sup>a</sup>	---
OER/ORR Acidic Exchange Current Density	20 A/m <sup>2</sup> <sup>a</sup>	---
OER/ORR Alkaline Exchange Current Density	10 A/m <sup>2</sup> <sup>a</sup>	---
Cathodic Charge Transfer Coefficient, H <sub>2</sub> and O <sub>2</sub>	0.5	32, 64-67
Anodic Charge Transfer Coefficient, H <sub>2</sub> and O <sub>2</sub>	0.5	32, 64-67
Number of Electrons Transferred/Reaction, H <sub>2</sub>	2	32
Number of Electrons Transferred/Reaction, O <sub>2</sub>	4	32

<sup>a</sup> These values were increased compared to literature values<sup>32,56,64</sup> to partly compensate for the shorter channel and BPE size compared to the experimental system, but the order of fastest to slowest kinetics remains consistent with the trend from previous literature.

**Table 3.9:** Geometry and other simulation parameters.

<b>Parameter</b>	<b>Value</b>	<b>Reference</b>
Surface Charge of Silica Walls	-3 mC/m <sup>2</sup>	---
Solution (Water) Dielectric Constant	78.3	68
Stern Layer Width	0.4 nm	69
Solution (Water) Refractive Index	1.33	38
Booth's Equation Parameter $\beta$	$1.41 \times 10^{-8}$ V/m	38
Applied Voltage	1.6 V	---
Channel Length	5 $\mu$ m	---
BPE Length	1.67 $\mu$ m	----
Reservoir Size (L x H)	10 $\mu$ m x 10 $\mu$ m	---
Channel Height	300-600 nm	---

### ***H. Acknowledgement***

This research was supported in-part by the Institute for Collaborative Biotechnologies through grants W911NF-09-001 and DAAD19-03-D-0004 from the U.S. Army Research Office. The content of the information does not necessarily reflect the position or the policy of the Government, and no official endorsement should be inferred.

## References

1. Duval, J.; Kleijn, J. M.; van Leeuwen, H. P. Bipolar electrode behavior of the aluminum surface in a lateral electric field. *J. Electroanal. Chem.* **2001**, *505*, 1-11.
2. Wei, W.; Xue, G.; Yeung, E. S. One-step concentration of analytes based on dynamic change in pH in capillary zone electrophoresis. *Anal. Chem.* **2002**, *74*, 934-940.
3. Laws, D. R.; Hlushkou, D.; Perdue, R. K.; Tallarek, U.; Crooks, R. M. Bipolar electrode focusing: simultaneous concentration enrichment and separation in a microfluidic channel containing a bipolar electrode. *Anal. Chem.* **2009**, *81*, 8923-8929.
4. Gao, R.; Ying, Y.; Hu, Y.; Li, Y.; Long, Y. Wireless bipolar nanopore electrode for single small molecule detection. *Anal. Chem.* **2017**, *89*, 7382-7387.
5. Gao, R.; Ying, Y.; Li, Y.; Hu, Y.; Yu, R.; Lin, Y.; Long, Y. A 30 nm nanopore electrode: facile fabrication and direct insights into the intrinsic feature of single nanoparticle collisions. *Angew. Chem.* **2018**, *130*, 1023-1027.
6. Ying, Y.; Hu, Y.; Gao, R.; Yu, R.; Gu, Z.; Lee, L. P.; Long, Y. Asymmetric nanopore electrode-based amplification for electron transfer imaging in live cells. *J. Am. Chem. Soc.* **2018**, *140*, 5385-5392.
7. Fosdick, S. E.; Crooks, R. M. Bipolar electrodes for rapid screening of electrocatalysts. *J. Am. Chem. Soc.* **2012**, *134*, 863-866.
8. Xu, W.; Fu, K.; Bohn, P. W. Electrochromic sensor for multiplex detection of metabolites enabled by closed bipolar electrode coupling. *ACS Sens.* **2017**, *2*, 1020-1026.

9. Ulrich, C.; Andersson, O.; Nyholm, L.; Björefors, F. Formation of molecular gradients on bipolar electrodes. *Angew. Chem.* **2008**, *120*, 3076-3078.
10. Fosdick, S. E.; Knust, K. N.; Scida, K.; Crooks, R. M. Bipolar electrochemistry. *Angew. Chem. Int. Ed.* **2013**, *52*, 10438-10456.
11. Paxton, W. F.; Kistler, K. C.; Olmeda, C. C.; Sen, A.; St. Angelo, S. K.; Cao, Y.; Mallouk, T. E.; Lammert, P. E.; Crespi, V. H. Catalytic nanomotors: autonomous movement of striped nanorods. *J. Am. Chem. Soc.* **2004**, *126*, 13424-13431.
12. Bonnefont, A.; Argoul, F.; Bazant, M. Z. Analysis of diffuse-layer effects on time-dependent interfacial kinetics. *J. Electroanal. Chem.* **2001**, *500*, 52-61.
13. Bazant, M. Z.; Thornton, K.; Ajdari, A. Diffuse-charge dynamics in electrochemical systems. *Phys. Rev. E.* **2004**, *70*, 021506.
14. Bazant, M. Z.; Chu, K. T.; Bayly, B. J. Current-voltage relations for electrochemical thin films. *SIAM J. Appl. Math.* **2005**, *65*, 1463-1484.
15. van Soestbergen, M. Frumkin-Butler-Volmer theory and mass transfer in electrochemical cells. *Russian Journal of Electrochemistry* **2012**, *48*, 570-579.
16. Rossi, M.; Wallmersperger, T.; Neukamm, S.; Padberg-Gehle, K. Modeling and simulation of electrochemical cells under applied voltage. *Electrochimica Acta* **2017**, *258*, 241-254.
17. Bard, A.; Faulkner, L. *Electrochemical Methods: Fundamentals and Applications*; John Wiley & Sons: New York, 2001.

18. Vetter, K. J. *Electrochemical Kinetics: Theoretical and Experimental Aspects*; Academic Press, Inc.: New York, 1967.
19. Frumkin, A. Hydrogen overpotential and the double layer structure. *Z. Phys. Chem. A* **1933**, *164*, 121-133.
20. Newman, J. S. *Electrochemical Systems*; Prentice-Hall, Inc.: New Jersey, 1973.
21. Anand, R. K.; Sheridan, E.; Knust, K. N.; Crooks, R. M. Bipolar electrode focusing: faradaic ion concentration polarization. *Anal. Chem.* **2011**, *83*, 2351-2358.
22. Pu, Q.; Yun, J.; Temkin, H.; Liu, S. Ion-enrichment and ion-depletion effects of nanochannel structures. *Nano Lett.* **2004**, *4*, 1099-1103.
23. Mani, A.; Zangle, T. A.; Santiago, J. G. On the propagation of concentration polarization from microchannel-nanochannel interfaces part I: analytical model and characteristic analysis. *Langmuir* **2009**, *25*, 3898-3908.
24. Biesheuvel, P. M.; van Soestbergen, M.; Bazant, M. Z. Imposed currents in galvanic cells. *Electrochimica Acta* **2009**, *54*, 4857-4871.
25. van Soestbergen, M. Diffuse layer effects on the current in galvanic cells containing supporting electrolyte. *Electrochimica Acta* **2010**, *55*, 1848-1854.
26. van Soestbergen, M.; Biesheuvel, P. M.; Bazant, M. Z. Diffuse-charge effects on the transient response of electrochemical cells. *Phys. Rev. E* **2010**, *81*, 021503.

27. Dhopeswarkar, R.; Hlushkou, D.; Nguyen, M.; Tallarek, U.; Crooks, R. M. Electrokinetics in microfluidic channels containing a floating electrode. *J. Am. Chem. Soc.* **2008**, *130*, 10480-10481.
28. Crouch, G. M.; Han, D.; Fullerton-Shirey, S. K.; Go, D. B.; Bohn, P. W. Addressable direct-write nanoscale filament formation and dissolution by nanoparticle-mediated bipolar electrochemistry. *ACS Nano* **2017**, *11*, 4976-4984.
29. Braun, T. M.; Schwartz, D. T. Bipolar electrochemical displacement: a new phenomenon with implications for self-limiting materials patterning. *ChemElectroChem* **2016**, *3*, 441-449.
30. Ordeig, O.; Godino, N.; del Campo, J.; Muñoz, F. X.; Nikolajeff, F.; Nyholm, L. On-chip electric field driven electrochemical detection using a poly(dimethylsiloxane) microchannel with gold microband electrodes. *Anal. Chem.* **2008**, *80*, 3622-3632.
31. Hine, F. *Electrode Processes and Electrochemical Engineering*; Plenum Press: New York, 1985.
32. Bockris, J. O'M. *Modern Aspects of Electrochemistry*, Vol 1; Butterworths: London, 1954.
33. Teorell, T. Transport processes and electrical phenomena in ionic membranes. *Prog. Biophys. Biophys. Chem.* **1953**, *3*, 305-369.
34. Jost, W. *Diffusion in Solids, Liquids, and Gases*; Academic Press: New York, 1952.
35. Stern, O. The theory of the electrolytic double layer. *Z. Elektrochem. Angew. Phys. Chem.* **1924**, *30*, 508-516.

36. Behrens, S. H.; Grier, D. G. The charge of glass and silica surfaces. *J. Chem. Phys.* **2001**, *115*, 6716-6721.
37. Booth, F. Dielectric constant of polar liquids at high field strengths. *J. Chem. Phys.* **1955**, *23*, 453-457.
38. Wang, H.; Pilon, L. Accurate simulations of electric double layer capacitance of ultramicroelectrodes. *J. Phys. Chem. C* **2011**, *115*, 16711-16719.
39. Bowden, F. P. The amount of hydrogen and oxygen present on the surface of a metallic electrode. *Proc. R. Soc. London, Ser. A* **1929**, *125*, 446-462.
40. Olesen, L. H.; Bruus, H.; Ajdari, A. ac electrokinetic micropumps: the effect of geometrical confinement, faradaic current injection, and nonlinear surface capacitance. *Phys. Rev. E* **2006**, *73*, 056313.
41. Bazant, M. Z.; Squires, T. M. Induced-charge electrokinetic phenomena. *Curr. Opin. Colloid Interface Sci.* **2010**, *15*, 203-213.
42. Duval, J. F. L.; Huijs, G. K.; Threels, W. F.; Lyklema, J.; van Leeuwen, H. P. Faradaic depolarization in the electrokinetics of the metal-electrolyte solution interface. *J. Colloid Interface Sci.* **2003**, *260*, 95-106.
43. Groot, C. C. M.; Bakker, H. J. A femtosecond mid-infrared study of the dynamics of water in aqueous sugar solutions. *Phys. Chem. Chem. Phys.* **2015**, *17*, 8449-8458.
44. Kohonen, M. M.; Karaman, M. E.; Pashley, R. M. Debye length in multivalent electrolyte solutions. *Langmuir* **2000**, *16*, 5749-5753.

45. Heberle, J.; Riesle, J.; Thiedemann, G.; Oesterhelt, D.; Dencher, N. A. Proton migration along the membrane surface and retarded surface to bulk transfer. *Nature* **1994**, *370*, 379-382.
46. Haber, F.; Russ, R. Über die elektrische reduction. *Z. Phys. Chem.* **1904**, *47*, 257-335.
47. Nernst, W. Theorie der reaktionsgeschwindigkeit in heterogenen systemen. *Z. Phys. Chem.* **1904**, *47*, 52-55.
48. Eden, A.; McCallum, C.; Storey, B. D.; Pennathur, S.; Meinhart, C. D. Analyte preconcentration in nanofluidic channels with nonuniform zeta potential. *Phys. Rev. Fluids* **2017**, *2*, 124203.
49. Togashi, D. M.; Szczupak, B.; Ryder, A. G.; Calvet, A.; O'Loughlin, M. Investigating tryptophan quenching of fluorescein fluorescence under protolytic equilibrium. *J. Phys. Chem. A* **2009**, *113*, 2757-2767.
50. Bouffier, L.; Doneux, T.; Goudeau, B.; Kuhn, A. Imaging redox activity at bipolar electrodes by indirect fluorescence modulation. *Anal. Chem.* **2014**, *86*, 3708-3711.
51. Chow, K.; Mavré, F.; Crooks, J. A.; Chang, B.; Crooks, R. M. A large-scale, wireless electrochemical bipolar electrode microarray. *J. Am. Chem. Soc.* **2009**, *131*, 8364-8365.
52. Delahay, P.; Berzins, T. Theory of electrolysis at constant current with partial or total control by diffusion – application to the study of complex ions. *J. Am. Chem. Soc.* **1953**, *75*, 2486-2493.
53. Green, L. W.; Kruus, P.; McGuire, M. J. Acid dissociation constants and rates as studied by ultrasonic absorption. *Can. J. Chem.* **1976**, *54*, 3152-3162

54. McConnell, H. M. Reaction rates by nuclear magnetic resonance. *J. Chem. Phys.* **1958**, *28*, 430-431.
55. Stillinger, F. H. *Theoretical Chemistry, Advances, and Perspectives*, Vol 3; Academic Press: New York, 1954, pp. 177-234.
56. Bagotzky, V. S.; Osetrova, N. V. Investigation of hydrogen ionization on platinum with the help of micro-electrodes. *Electroanalytical Chemistry and Interfacial Electrochemistry* **1973**, *43*, 233-249.
57. Heberle, J.; Riesle, J.; Thiedemann, G.; Oesterhelt, D.; Dencher, N. A. Proton migration along the membrane surface and retarded surface to bulk transfer. *Nature* **1994**, *370*, 379-382.
58. Persat, A.; Chambers, R. D.; Santiago, J. G. Basic principles of electrolyte chemistry for microfluidic electrokinetics. Part 1: Acid-base equilibria and pH buffers. *Lab Chip* **2009**, *9*, 2437-2453.
59. Ferrell, R.; Himmelblau, D. M.; Diffusion coefficients of nitrogen and oxygen in water. *J. Chem. Eng. Data* **1967**, *12*, 111-115.
60. Charlton, S. R.; Parkhurst, D. L. Modules based on the geochemical model PHREEQC for use in scripting and programming languages. *Computers & Geosciences* **2011**, *37*, 1653-1663.
61. Milanova, D.; Chambers, R.; Santiago, J. G. Electrophoretic mobility measurements of fluorescent dyes using on-chip capillary electrophoresis. *Electrophoresis* **2011**, *32*, 3286-3294.
62. Beynon, R. J.; Easterby, J. S.; *Buffer Solutions*; IRL Press at Oxford University Press: Oxford, New York, 1966.

63. Green, L. W.; Kruus, P.; McGuire, J. M. Acid dissociation constants and rates as studied by ultrasonic absorption. *Can. J. Chem.* **1976**, *54*, 3152-3162.
64. Trasatti, S. Work function, electronegativity, and electrochemical behaviour of metals III. Electrolytic hydrogen evolution in acid solutions. *J. Electroanal. Chem* **1972**, *39*, 163-184.
65. Ollo, K.; Guillaume, P. L. A.; Auguste, A. F. T.; Quand-Meme, G. C.; Honoré, K. K.; Lassiné, Q. Influence of various metallic oxides on the kinetic of the oxygen evolution reaction on platinum electrodes. *J. Electrochem. Sci. Eng.* **2015**, *5*, 79-91.
66. Notoya, R.; Matsuda, A.; Determination of the rate of the discharge step of hydrogen ion on a hydrogen-platinum electrode in aqueous solutions by the galvanostatic transient method. *J. Phys. Chem.* **1989**, *93*, 5521-5523.
67. Durst, J.; Siebel, A.; Simon, C.; Hasche, F.; Herranz, J.; Gasteiger, H. A. New insights into the electrochemical hydrogen oxidation and evolution reaction mechanism. *Energy Environ. Sci.* **2014**, *7*, 2255-2260.
68. Malmberg, C. G.; Maryott, A. A.; Dielectric constant of water from 0 to 100 C. *J. Res. Nat. Bureau Stand.* **1956**, *56*, 1-8.
69. Velikonja, A.; Gongadze, E.; Kralj-Iglic, V.; Iglic A. Charge dependent capacitance of stern layer and capacitance of electrode/electrolyte interface. *Int. J. Electrochem. Sci.* **2014**, *9*, 5885-5894.

## **IV. Induced-Charge Electroosmotic Flow at Bipolar Electrodes: A Potential Mechanism for Mixing and Peristaltic Micropump Actuation**

### *A. Abstract*

We present a novel technique for the electrokinetic actuation of a peristaltic micropump and briefly discuss the prospects of utilizing ICEOF at BPEs for mixing applications. The micropump discussed herein is a diaphragm-based positive-displacement micropump actuated by internally-generated pressure gradients resulting from ICEOF at a BPE in a microfluidic or nanofluidic channel. No electrochemical reactions at the BPE are required, though hybrid hydrodynamic-electrochemical actuation could potentially improve the effectiveness of the pump and provide more flexibility in operating conditions and materials. Through numerical modeling of the fluid-structure interactions, we examine the initiation of ICEOF at the BPE by aperiodic and periodic waveforms. We find that aperiodic actuation is somewhat effective but impractical, while periodic actuation suffers from significant backflow issues. To develop a more robust operating principle, we resolve this latter issue by introducing deformable polymer flaps into our simulation to provide directionally-biased hydrodynamic resistance and thus inhibit backflow. Our BPE peristaltic micropumping mechanism provides a promising approach for the predictable and precise manipulation of small fluid volumes that can be spatially and electrochemically isolated from contamination. This chapter was reproduced in part with permission from the Journal of Physical Chemistry C, in press. Unpublished work copyright 2019 American Chemical Society (DOI: 10.1021/acs.jpcc.8b10473).

## ***B. Introduction***

Manipulation of small fluid volumes is an essential process in lab-on-chip applications, and the ability to accomplish this task in a quick and facile manner enhances the operational efficiency of analytical devices utilized for mixing and pumping applications. From microelectronics cooling to biological assays and wearable drug delivery systems, micropumps in particular are fast becoming a ubiquitous and valuable tool for transport and thermal management.<sup>1</sup> Hence, the ability to understand and model the physical processes involved during actuation and the subsequent fluid transport is essential to the understanding and development of novel micropumping systems. Actuation techniques including electrostatic,<sup>2</sup> piezoelectric,<sup>3</sup> pneumatic,<sup>4</sup> thermo-pneumatic,<sup>5</sup> and electrochemical<sup>6-8</sup> have previously been demonstrated for diaphragm-based micropumps. In this chapter, we investigate the potential for BPE-induced electrokinetic actuation realized by internal pressure gradients arising due to nonlinear ICEOF.

Nonlinear induced-charge electrokinetic (ICEK) flow phenomena resulting from subjecting polarizable materials to applied electric fields have been studied extensively in the context of pumping,<sup>9-11</sup> mixing,<sup>12,13</sup> and particle manipulation<sup>14,15</sup> (see the review by Bazant and Squires<sup>16</sup> for a thorough discussion on previous ICEK research). The implementation of a phenomenological electroosmotic slip velocity boundary condition is a common feature encountered in prior ICEOF analyses, which often do not include electrochemical reactions and tend to ignore non-electroneutral EDL charge distributions by assuming negligibly thin EDLs.<sup>10,16</sup> Because we incorporate microscopic charge-transfer theory and resolve diffuse layer effects down to the no-slip shear plane, our model provides one of the most complete descriptions to date of ICEOF at a bipolar electrode surface.

### C. BPE Induced-Charge Electroosmotic Flow

As one might expect, upon BPE polarization the EDL above the negatively charged cathode is predominantly occupied by cations, while the EDL above the positive anode consists mainly of anions. Under an applied field, these ions migrate in opposite directions and subsequently generate nonuniform ICEOF above the BPE (see Figures 4.1 and 4.2). These opposing flow directions produce distinct hydrodynamic recirculation regions above the poles which induce adverse pressure gradients upstream and favorable pressure gradients downstream of the BPE (Figure 4.2) in order to maintain mass conservation. Note, however, that the net advective transport is still left to right due to electroosmotic pumping from the channel wall EDLs. Our simulations predicted induced pressure gradients on the order of  $10^9$ - $10^{10}$  Pa/m; due to the shortened channel length in our simulations, however, we calculated maximum fluid gauge pressures on the order of 10 kPa.

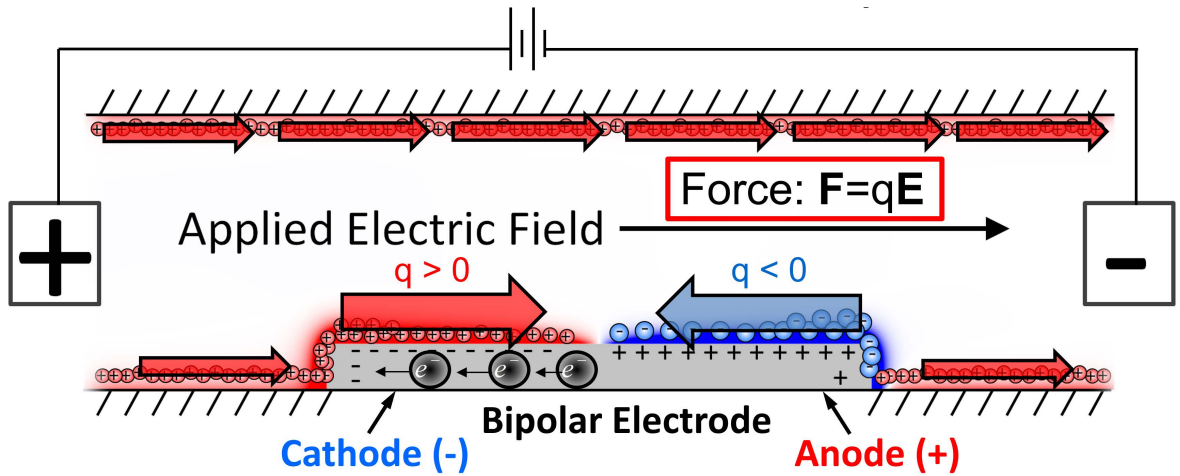


**Figure 4.1:** Coulombic forces acting on the channel wall and BPE EDLs. Regions of positive space charge near the channel walls and BPE cathode migrate downstream under a positive (left to right) electric field, while the region of negative space charge above the anode migrates upstream under the applied field. These opposing flow directions lead to hydrodynamic recirculation and induced pressure gradients within the channel.

The relaxation time scales of charge migration and viscous flow are intimately coupled during charging of the BPE due to the Coulombic forces acting within the equilibrium and nonequilibrium EDLs. Specifically, for very early times during BPE charging (i.e. before the Faradaic relaxation time) we observe that the ICEOF effect remains relatively small compared to the EOF from EDLs at the fused silica channel walls (as evidenced by the lack of flow recirculation from 0-2  $\mu$ s in Figures 4.2(b) and 4.2(c)). This is because the latter EDLs are already formed at equilibrium before the application of an electric field, whereas it takes time for diffuse charge to accumulate and subsequently migrate upstream/downstream in the nonequilibrium EDLs surrounding the BPE as it becomes polarized. It should also be noted that the composition of the channel wall EDLs can eventually be altered as a result of changes in zeta potential and ionic strength due to significant electrochemical consumption or production of ions; this is particularly true for protons.<sup>17</sup> Thus, the complete picture of spatiotemporal EOF and ICEOF evolution is a complicated one which is highly dependent on the ionic charge composition of the solution, the extent of BPE polarization, and the reaction kinetics.

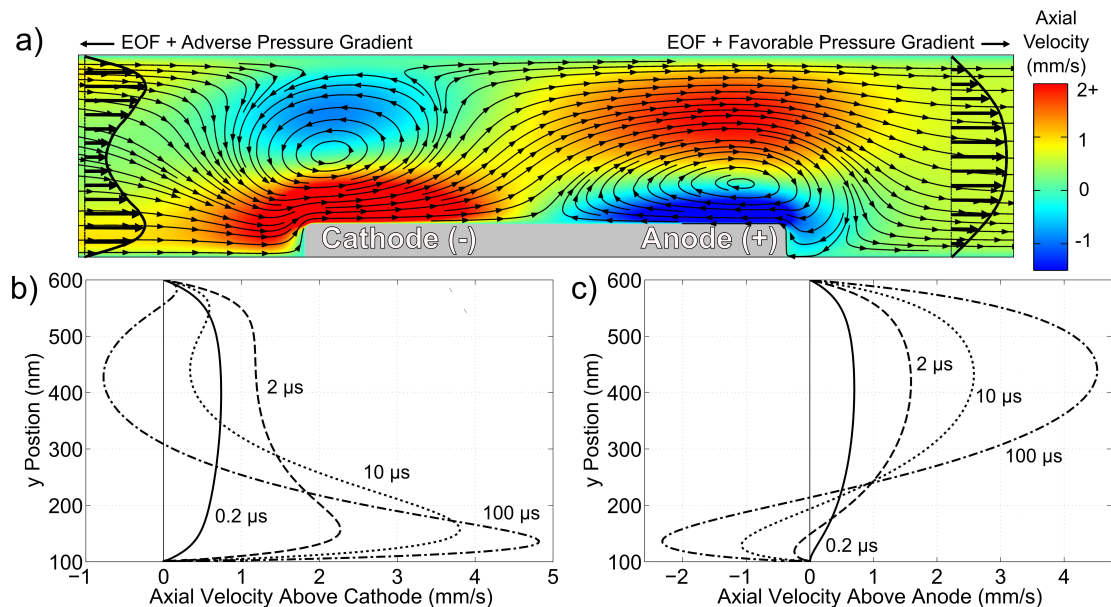


**Figure 4.2:** Induced-charge electroosmotic flow near the BPE for a 600 nm tall channel with a 1.0 mM buffer solution: (a) 2D profile depicting the axial velocity magnitude along with arrows and streamlines indicating the local flow direction, and evolution of the axial EOF profile above (b) the cathodic and (c) anodic poles at different times.

Previous studies have shown that pressure gradients arising from nonuniform EOF are capable of causing physical deformation of channel walls and delamination of bonded wafers.<sup>18</sup> Although we do not observe these detrimental effects in our current experiments due to the relatively thick (i.e., 0.5 mm) fused silica walls used, we will demonstrate in the next section that such pressure forces can be used to our advantage by slightly modifying the device configuration.

#### ***D. BPE-Induced Peristaltic Pumping Mechanism***

We can extend our detailed bipolar ICEOF model to represent a channel with a deformable wall, leading to the prospect of combining conventional electrochemical actuation with hydrodynamic positive-displacement pumping realized by ICEOF-induced internal pressure gradients. Electrochemical actuation has been studied previously,<sup>6-8</sup> though our proposed

design allows for additional control and customization by coupling the nonlinear hydrodynamics with wireless bipolar electrochemistry. Specifically, if the top silica glass channel wall of our device was instead replaced by a thin membrane made from a flexible material such as polydimethylsiloxane (PDMS), the high local pressure near the BPE cathode could be leveraged to physically deflect the membrane as an effective actuation mechanism.

This physical phenomenon can be modeled through the use of fluid-structure interaction equations, which couple the solid mechanics and fluid mechanics with a stress matching condition at the fluid-solid interface. Therefore, for generality we use the Navier-Stokes equation and mass conservation,

$$\rho \left( \frac{\partial \mathbf{u}_{\text{fluid}}}{\partial t} + \mathbf{u}_{\text{fluid}} \cdot \nabla \mathbf{u}_{\text{fluid}} \right) = \eta \nabla^2 \mathbf{u}_{\text{fluid}} - \nabla P - \rho_E \nabla \psi; \quad \nabla \cdot \mathbf{u}_{\text{fluid}} = 0, \quad (4.1)$$

where  $\mathbf{u}_{\text{fluid}}$  is the fluid velocity vector. For the structural mechanics, we invoke momentum conservation for the solid,

$$\rho \frac{\partial^2 \mathbf{u}_{\text{solid}}}{\partial t^2} = \nabla \cdot \boldsymbol{\sigma}_{\text{solid}}, \quad (4.2)$$

where  $\mathbf{u}_{\text{solid}}$  is the solid displacement vector and  $\boldsymbol{\sigma}_{\text{solid}}$  is the local stress tensor in the solid. There are two conditions that must be met at the fluid-solid interface boundary: 1) the interface is maintained by the fluid and solid both moving with the same velocity at the boundary (i.e. no-slip) and 2) the stress exerted on the fluid by the solid is equal to the stress exerted on the solid by the fluid (i.e. Newton's 3<sup>rd</sup> law). Mathematically, these conditions are respectively represented by,

$$\mathbf{u}_{\text{fluid}} = \frac{\partial \mathbf{u}_{\text{solid}}}{\partial t}, \quad (4.3)$$

$$\boldsymbol{\sigma}_{\text{solid}} \cdot \mathbf{n} = \boldsymbol{\Gamma} \cdot \mathbf{n}, \quad (4.4)$$

where  $\boldsymbol{\Gamma}$  is the fluid stress tensor, given by  $\boldsymbol{\Gamma} = -P\mathbf{I} + \eta[\nabla\mathbf{u} + (\nabla\mathbf{u})^T]$ , where  $\mathbf{I}$  is the identity tensor. These equations are coupled to the Poisson-Nernst-Planck system of equations from Chapter III in order to solve for the electrokinetic actuation of the membrane and subsequent positive-displacement pumping in the top channel.

Figure 4.3(a) shows a hypothetical configuration in which an actuation channel containing a BPE is utilized to pump stationary fluid in an adjacent channel by peristaltic motion of the flexible PDMS membrane. When an electric potential is introduced across the bottom channel, the high and low pressures due to ICEOF near the cathode and anode, respectively, cause the membrane to deform accordingly. This deformation subsequently influences the pressure distribution in the above sample fluid channel, causing localized high pressure above the cathode and flow out of the top channel due to the cross-sectional pinching effect (Figure 4.3(a)). Above the anode, the downwards deflection of the membrane conversely reduces the local pressure and draws sample fluid in to be stored in the expanded cross-section. When the potential is turned off, the membrane relaxes and some of the stored fluid is transported towards the cathode to be pumped out of the channel upon subsequent BPE activation.

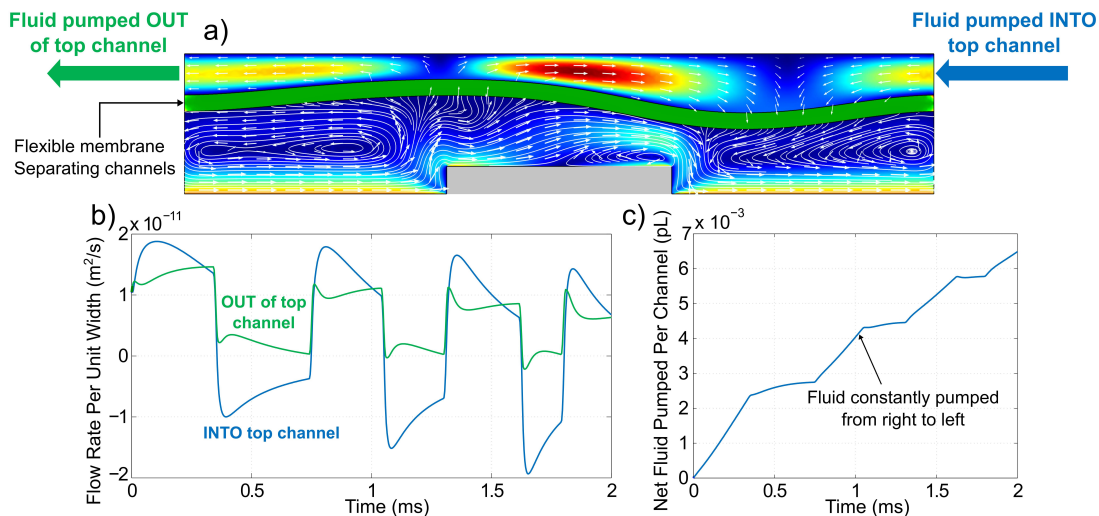


**Figure 4.3:** (a) Peristaltic pumping configuration with a flexible membrane separating a BPE actuation channel from a sample fluid channel, (b) flow rates the top target channel inlet and outlet show storage and pumping of fluid made possible by aperiodic hydrodynamic membrane deflection, and (c) net fluid volume pumped through the top channel over several potential-switching cycles.

The nontrivial coupling between the electrokinetics, hydrodynamics, and solid mechanics in this particular configuration requires precise timing of potential switching for maximum operating efficiency if aperiodic actuation is employed. Figures 4.3(b) and 4.3(c) depict an optimized pumping cycle for the simulated geometry which ensures that fluid is continuously pumped out of the top channel throughout multiple actuation steps at an initial rate of approximately 7.5 pL/s per channel. In this model, the BPE was actuated by aperiodic 0.2 V square wave pulses (see Figure 4.3(b) for flow rates during the on/off periods) of single polarity. The attenuating actuation period in this simulation, which would pose difficulties for practical device operation, is required here to prevent backflow as the membrane relaxes. In practice, microfabricated polymer flaps can be integrated to provide anisotropic hydrodynamic resistance and act as passive check valves,<sup>1</sup> enabling continuous rectified pumping with minimal backflow using a much simpler sinusoidal actuation signal.

Figure 4.4 illustrates an example of the pumping process for a device with integrated passive valves. The first step is the same as that depicted in Figure 4.3(a), in which upwards deflection of the membrane near the cathode locally increases the top fluid pressure and the downwards deflection near the anode locally decreases the pressure. The anisotropic resistance of the angled flaps permits flow from right to left but inhibits flow in the reverse direction, thus the valves open because there is a positive pressure gradient (that is, higher pressure to the right and lower pressure to the left) at both the top right and top left boundaries.

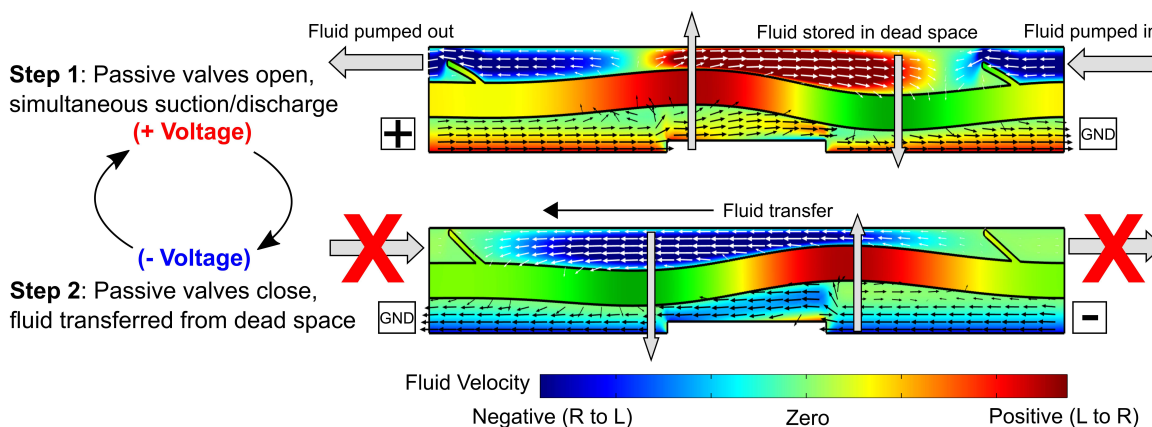


**Figure 4.4:** Depiction of the reciprocating peristaltic pumping mechanism for a periodically-actuated device with integrated polymer flap valves for 50  $\mu\text{m}$  long, 1  $\mu\text{m}$  tall channels separated by 1  $\mu\text{m}$  thick PDMS (axial coordinate not to scale). The anisotropic hydrodynamic resistance of the angled flaps permits flow from right to left but inhibits flow in the reverse direction, causing the valves to close and stored fluid to be transported from right to left.

As the polarity of the actuation waveform reverses, the flow direction in the bottom channel switches and the membrane subsequently starts to move upwards near the right edge of the BPE and downwards near the left edge of the BPE. This motion causes the top fluid pressure to decrease above the left edge and increase above the right edge due to the cross-sectional expansion and reduction, respectively. In the absence of any passive valves, this periodic actuation would result in all of the fluid that was pumped out of the top left outlet

during the first step being pulled back in and pumped out of the top right inlet, such that the flow simply moves back and forth over time and no net pumping is achieved. By contrast, the valves largely prevent backflow and assist in the efficient transfer of fluid stored in the dead space towards the left BPE edge; this fluid is now stored in dead space above the left BPE edge and will be pumped out of the top left upon polarity reversal of the AC signal. Figure 4.5 demonstrates how the passive valves rectify the pumping output.

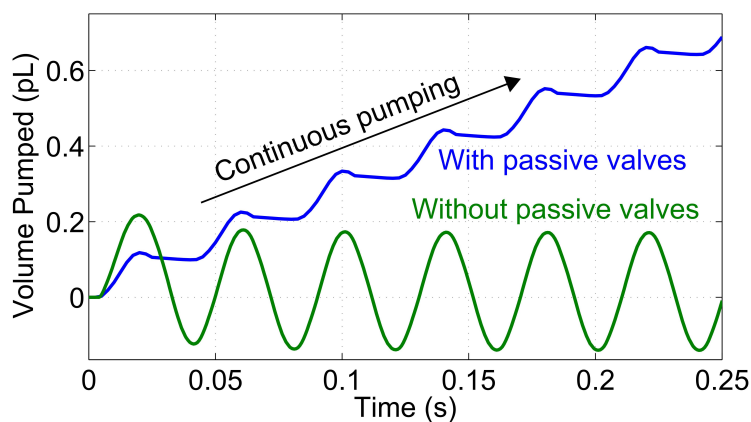


**Figure 4.5:** Simulated periodic pumping profiles for a device with (blue curve) and without (green curve) passive valves. Without any mechanism for preventing backflow, periodic actuation leads to no net fluid being pumped. Conversely, an electrokinetic BPE pumping device with passive valves can yield continuous and near-unidirectional pumping.

Note that our fully-coupled fluid-structure interaction model includes only the ICEOF and neglects Faradaic reactions for simplicity; at high reaction rates, however, the production of dissolved gases at high concentrations and subsequent bubble nucleation in the confined geometry will further exacerbate the nonuniform pressure distribution<sup>19,20</sup> and could allow for more effective physical actuation. Moreover, by varying the dimensions of an array of BPEs situated along the channel axis, one can more selectively deform a structure by actuating specific BPEs through control of the applied potential magnitude and thus the degree of individual BPE polarization. A more sophisticated microband array of discontinuous “split

BPEs<sup>21,22</sup> could also hypothetically be implemented to provide improved control over the specific timing and location of actuation throughout an extended system. This hybrid manner of hydrodynamic and wireless bipolar electrochemical actuation could provide a valuable means for pumping small volumes of an electrochemically isolated fluid without the necessity for mechanical integration, vacuum control, or direct electrical interfacing with the fluid sample of interest.

### *E. Electrokinetic Mixing Using Bipolar Electrodes*

As we have shown, strong hydrodynamic recirculation regions manifest due to ICEOF above the BPE when a relatively large electric field is introduced in the channel. In Chapter I we discussed how such flow patterns are a common feature in mixing devices,<sup>13</sup> which suggests that BPEs can also be employed in fluidic channels or capillaries to disturb local flow structures and promote mixing of disparate substances. Using our numerical model, we can easily probe the validity of this approach. To accomplish this, we simulate the transport of two uncharged species using an existing steady state velocity field solution solved for in Chapter III as the convection coefficient in the species conservation equation. We introduce two unmixed species into the channel entrance as an inlet boundary condition; that is, one species occupies only the top half of the channel inlet and the other species occupies only the bottom half of the inlet. An outflow condition at the channel outlet enforces a zero normal concentration gradient for both uncharged species and allows the concentration values to float to values which satisfy the conservation equations. The numerical product of the concentrations of the two species provides a measure of how much common space the two species occupy, and thus serves well as a mixing metric which allows for visualization of well-mixed zones.

While being transported downstream in a straight channel, the two species can mix only by transverse diffusion and Taylor dispersion<sup>23</sup> (which is more prominent for EOF in nanochannels than for microchannels with plug-like flow and longer diffusion time scales). By contrast, a channel with BPEs offers the ability to generate recirculating flow patterns that aid in mixing, as discussed in Chapter I. Figure 4.6 shows the relative influence of the BPE on the mixing metric for transport conditions at  $Pe = 6000$ . The results indicate that the BPE serves reasonably well simply as a static mixer; an array of BPEs can be patterned throughout the channel (on both the top and bottom walls) to significantly enhance fluid mixing. Arguably a more effective technique, however, would be similar to the periodic voltage switching technique mentioned for the electrothermal micromixer in Chapter I. That is, intermittent reversal of the applied potential polarity would disturb the flow structures around the BPE and potentially induce chaotic mixing patterns in the flow, particularly for larger scale devices than that simulated here (a 600 nm tall channel).

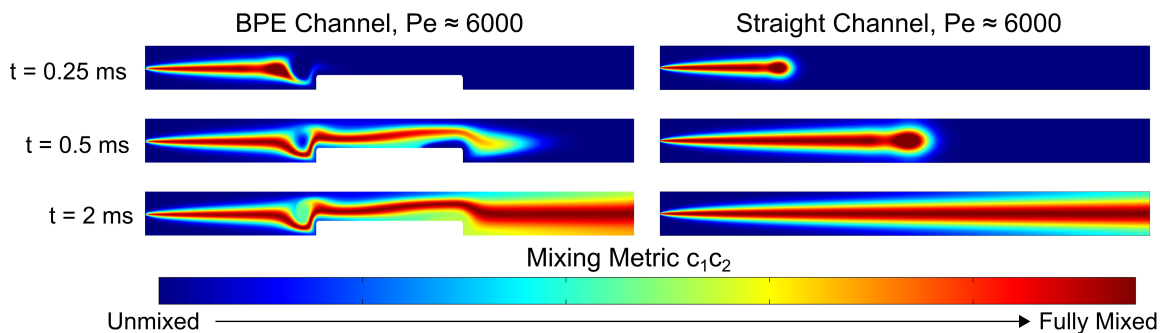


**Figure 4.6:** Spatiotemporal mixing distribution for a fluidic device with and without a BPE. Plots show the mixing of two species which initially enter unmixed at the left boundary and are advected downstream, visualized as the product of the two species' concentrations. For the straight channel, mixing occurs only by Taylor dispersion and direct transverse diffusion, whereas the recirculating flow near the BPE aids in mixing.

### ***F. Conclusion***

In this work, we examined the role of BPE induced-charge electroosmotic flow on the hydrodynamic conditions achieved in a nanochannel under an applied potential difference. By numerically resolving the flow down to the shear plane, we captured the coupled effects of surface polarization and electrokinetic EDL charging on the fluid dynamics and transient response of the system. We showed that resulting pressure gradients from the predicted hydrodynamic recirculation are theoretically capable of actuating a peristaltic micropumping mechanism by physical deflection of a flexible membrane, and we demonstrated this concept numerically with a highly coupled fluid-structure interaction model. Moreover, we showed that with the use of structurally integrated polymer flaps as passive valves, continuous and rectified peristaltic pumping can be achieved in the device with simple AC waveform actuation. Finally, we demonstrated that the hydrodynamic recirculation associated with ICEOF at the BPE can potentially offer a flexible platform for rapid on-chip mixing, with the capabilities for widely parallelizable static or dynamic mixing.

### ***G. Acknowledgement***

This research was supported in-part by the Institute for Collaborative Biotechnologies through grants W911NF-09-001 and DAAD19-03-D-0004 from the U.S. Army Research Office. The content of the information does not necessarily reflect the position or the policy of the Government, and no official endorsement should be inferred.

## References

1. Laser, D. J.; Santiago, J. G. A review of micropumps. *J. Micromech. Microeng.* **2004**, *14*, R35-R64.
2. Zengerle, R.; Ulrich, J.; Kluge, S.; Richter, M.; Richter, A. A bidirectional silicon micropump. *Sensors Actuators A* **1995**, *50*, 81-86.
3. Li, S.; Chen, S. Analytical analysis of a circular PZT actuator for valveless micropumps. *Sensors Actuators A* **2003**, *104*, 151-161.
4. Rapp, R.; Schomburg, W. K.; Maas, D.; Schulz, J.; Stark, W. LIGA micropump for gases and liquids. *Sensors Actuators A* **1994**, *40*, 57-61.
5. van de Pol, F. C. M.; van Lintel, H. T. G.; Elwenspoek, M.; Fluitman, J. H. J. A thermopneumatic micropump based on micro-engineering techniques. *Sensors Actuators A* **1990**, *21*, 198-202.
6. Neagu, C.; Jansen, H.; Gardeniers, H.; Elwenspoek, M. The electrolysis of water: an actuation principle for MEMS with a big opportunity. *Mechatronics* **2000**, *10*, 571-581.
7. Xie, J.; Miao, Y.; Shih, J.; He, Q.; Liu, J.; Tai, Y.; Lee, T. D. An electrochemical pumping system for on-chip gradient generation. *Anal. Chem.* **2004**, *76*, 3756-3763.
8. Li, P.; Sheybani, R.; Gutierrez, C. A.; Kuo, J. T. W.; Meng, E. A parylene bellows electrochemical actuator. *J. Microelectromech. Syst.* **2010**, *19*, 215-228.
9. Beebe, D. J.; Mensing, G. A.; Walker, G. M. Physics and applications of microfluidics in biology. *Annu. Rev. Biomed. Eng.* **2002**, *4*, 261-286.
10. Squires, T. M.; Bazant, M. Z. Induced-charge electro-osmosis. *J. Fluid. Mech.* **2004**, *509*, 217-252.

11. Ajdari, A. Pumping of liquids using asymmetric electrode arrays. *Phys. Rev. E* **2000**, *61*, R45-R48.
12. Whitesides, G. M.; Stroock, A. D. Flexible methods for microfluidics. *Phys. Today* **2001**, *54*, 42-48.
13. Wu, Z.; Li, D. Micromixing using induced-charge electrokinetic flow. *Electrochimica Acta* **2008**, *53*, 5827-5835.
14. Anderson, J. L. Effect of nonuniform zeta potential on particle movement in electric fields. *J. Colloid Interface Sci.* **1985**, *105*, 45-54.
15. Yariv, E. Induced-charge electrophoresis of nonspherical particles. *Phys. Fluids* **2005**, *17*, 051702.
16. Bazant, M. Z.; Squires, T. M. Induced-charge electrokinetic phenomena. *Curr. Opin. Colloid Interface Sci.* **2010**, *15*, 203-213.
17. Behrens, S. H.; Grier, D. G. The charge of glass and silica surfaces. *J. Chem. Phys.* **2001**, *115*, 6716-6721.
18. de Rutte, J. M.; Janssen, K. G. H.; Tas, N. R.; Eijkel, J. C. T.; Pennathur, S. Numerical investigation of micro- and nanochannel deformation due to discontinuous electroosmotic flow. *Microfluid. Nanofluid.* **2016**, *20*, 150.
19. Gao, R.; Ying, Y.; Hu, Y.; Li, Y.; Long, Y. Wireless bipolar nanopore electrode for single small molecule detection. *Anal. Chem.* **2017**, *89*, 7382-7387.

20. Contento, N. M.; Branagan S. P.; Bohn, P. W. Electrolysis in nanochannels for in situ reagent generation in confined geometries. *Lab Chip* **2011**, *11*, 3634-3641.
21. Ordeig, O.; Godino, N.; del Campo, J.; Muñoz, F. X.; Nikolajeff, F.; Nyholm, L. On-chip electric field driven electrochemical detection using a poly(dimethylsiloxane) microchannel with gold microband electrodes. *Anal. Chem.* **2008**, *80*, 3622-3632.
22. Chow, K.; Mavré, F.; Crooks, J. A.; Chang, B.; Crooks, R. M. A large-scale, wireless electrochemical bipolar electrode microarray. *J. Am. Chem. Soc.* **2009**, *131*, 8364-8365.
23. Tallarek, U.; Rapp, E.; Scheenen, T.; Bayer, E.; Van As, H. Electroosmotic and pressure-driven flow in open and packed capillaries: velocity distributions and fluid dispersion. *Anal. Chem.* **2000**, *72*, 2292-2301.